The Dissertation Committee for Bisen Lin
certifies that this is the approved version of the following dissertation:

On the Motion of Flexible Strings and Filaments in Inertial and Viscous Regimes

Committee:

K. Ravi-Chandar, Supervisor

Mark E. Mear

Gregory J. Rodin

Rui Huang

Michael Marder

On the Motion of Flexible Strings and Filaments in Inertial and Viscous Regimes

by

Bisen Lin, B.S.; M.S.

DISSERTATION

Presented to the Faculty of the Graduate School of
The University of Texas at Austin
in Partial Fulfillment
of the Requirements
for the Degree of

DOCTOR OF PHILOSOPHY

THE UNIVERSITY OF TEXAS AT AUSTIN
December 2007

Dedicated to:

my wife *Xiaomei (Catherine) Han*,

my parents *Zancheng Lin* and *Shixia Zheng*.

Acknowledgments

I would like to express my appreciation and sincere gratitude to my advisor, Professor Krishnaswamy Ravi-Chandar, for all of his excellent teaching, guidance and support throughout my Ph.D. studies. His broad knowledge and deep physical understanding of the subject helped me throughout this research. I also thank my committee members, Professors Mark E. Mear, Gregory J. Rodin, Rui Huang and Michael Marder, for spending their valuable time on reading and making valuable comments on this dissertation.

My appreciations also go to professors in EM program for their excellent teaching and supports, which leaded to important parts of preparations for my research. I also thank Professor Oscar Gonzalez from Math Department for his excellent teaching and discussion with me on part of the numerical treatment, and Professor Ronald Stearman for using his LDS electro-magnetic shaker. My gratitude also goes to Mr. Travis Crooks, David Gray, Rick Maldonado, and Frank Wise for their excellent technical laboratory support.

I would also like to thank all my colleagues and friends for their help and friendship. Last but certainly not least, special thanks go to my family for their constant support throughout my school life. I sincerely express my great appreciation to my loving wife, Xiaomei (Catherine) Han, for her invaluable support and encouragement.

BISEN LIN

On the Motion of Flexible Strings and Filaments in Inertial and Viscous Regimes

Publication No. __________________

Bisen Lin, Ph.D.
The University of Texas at Austin, 2007

Supervisor: K. Ravi-Chandar

Study of the dynamics of strings and filaments has broad applications, for instance, macroscopic coil motion in petroleum engineering and microscopic one-armed swimmers in biological science. In this work, we study the motions of flexible strings and thin filaments in two different regimes, inertial and viscous, theoretically and experimentally.

Quantitative experiments on the whirling string show that steady motion exists only when the string whirls at its natural frequencies and that whirling motions for other frequencies exhibit rich dynamics. Furthermore, three kinds of response have been observed experimentally for the planar excitation: planar steady oscillation; two-dimensional (2D) to three-dimensional (3D) transient response; 3D steady whirling motion. These phenomena repeat as the driving frequency is increased. The forced response of a string subjected to planar excitation is analyzed through a perturbation technique and multiple time scale method.

The steady-state whirling motion of linear elastic filaments under self-weight with rotary excitation at one end and free at the other has been examined; specifically, the effect of bending stiffness has been investigated both theoretically and experimentally. The theoretical predictions have been compared with the experimental results for thin filaments with different bending stiffness to demonstrate the effect of bending stiffness directly. The dynamic response of thin filaments under planar excitation has also been studied experimentally.

The two-dimensional dynamics of an Euler elastica in low-Reynolds number regime has been studied. Tension effects have been shown to be either comparable to or dominant over the bending contributions for the microscopic one-armed swimmers. Hence one may change the tension in situ through the externally or internally generated forces, thus changing the effective bending stiffness, and as a consequence controlling the swimming velocity and the propulsion efficiency.

Finally, the low-Reynolds-number dynamics of a micro-string has been studied, in order to understand the physics underpinning eukaryotic sperm flagellar swimming. Both linear analysis of small-amplitude swimming and fully numerical simulations show that time-reversal symmetry is broken, which leads to the propulsion. Numerical studies have been performed for different boundary conditions and different forcing levels. Comparison with previous bending model illustrated that, for the same equivalent bending stiffness, the micro-string has higher propulsion efficiency with similar swimming velocity. Excellent agreement between the simulation predictions and the experimentally observed flagellar waveforms has been obtained. With this theoretical model, observations of swimming characteristics of the sperm of different species are reconciled into a single scaling relationship, characterized by the so-called "string sperm number". Our results

imply that tension plays a crucial role in flagellar elasticity and provides impetus for studying a different model underlying the physics of flagellar swimming. For example, it is possible to postulate alternate hypotheses for active force generation by the dynein motors; it also enables the formulation of a different role to the micro-filaments in general, one based on tension rather than one based on bending.

Table of Contents

List of Tables

List of Figures

Chapter 1

Introduction

In this dissertation, the dynamic response of flexible strings and filaments is examined with a view towards biological applications. Previous research on the motion of flexible strings and thin filaments in inertial gravitational regime is reviewed first in Section 1.1. Then, recent studies on the microscopic one-armed swimmer at low-Reynolds number are summarized in Section 1.2; this is followed in Section 1.3 by detailed outline of this dissertation.

1.1 Motion of Flexible Strings and Thin Filaments in the Inertial Regime

Studies of the vibrations of strings have a long history; Bernoulli, Euler, Kirchhoff, Rayleigh and many others have explored various aspects of this problem. Routh [79] provides a summary of the analysis of strings and cables in great detail and provides a historical context. There is a vast recent literature on the transverse vibration of strings [22,47,66–68,70,75,76]. Most of these investigations focus on the problem of a taut string held between two points under a constant tension and set in motion to generate transverse deflections of the string. Even as early as 1858 non-planar whirling under planar excitation was noted by Rayleigh. When forced by transverse harmonic motion far below the natural frequency of the linearized equations of motion, a string exhibits transverse oscillations that are confined to the plane of excitation. However, as the natural frequency is approached, and the amplitude of the transverse motion exceeds a critical level, the transverse motion of the string becomes unstable to perturbations; the resulting motion is a whirling motion where the string deflects not only in the plane of excitation, but also perpendicular to it. With further increases in the frequency, the amplitude of the whirling motion grows first and then diminishes abruptly; well beyond the natural frequency, the string resumes planar motion with smaller amplitudes. This behavior has been examined analytically by numerous investigators. Narasimha [68] pointed out that even under small amplitude motion, the equations governing the motion are inherently nonlinear. He showed that neglecting the axial stretch and changes in tension along the length of the wire is not justifiable. While this was implicit in the earlier analysis (see Routh [79]), Narasimha [68] made the representation of the length and tension changes explicit and showed further that planar motion was unstable at a high enough amplitude. Tufillaro [88] developed a simple single mode model for the string and examined the planar and nonplanar motions; periodic, quasi-periodic and chaotic motions were observed in this model. O'Reilly and Holmes [75] and Nayfeh, et al., [70] examined the dynamics of this whirling motion by the method of multiscales. These models are able to capture the essence of the problem: that planar motions are unstable near the natural frequencies of the linearized problem. In all these investigations, the primary motion was the string deflection in the plane of the driving force; the whirling or out-of-plane motion was the result of instabilities in the system.

Whirling motion of perfectly flexible strings also exhibits rich dynamics. Steady-state solutions of the linearized problem in terms of Bessel functions were described by Fourier. Routh [79] describes many special cases of the hanging string or chain problem. Kolodner [55] provided a complete mathematical model for this nonlinear problem associated with the whirling of an inextensible, flexible string. While Kolodner predicted the qualitative behavior of steady-state solutions, he did not obtain a complete solution to the problem. Bessel's functions of the first kind of order zero were already known to represent the whirling shape of the string corresponding to the linearized problem [79]. Caughey [23] performed a perturbation analysis of the small amplitude oscillations near the natural frequencies of the linearized problem and found stable and unstable regimes of the solutions. Caughey [24] also presented an analysis of whirling of a string fixed at one end and constrained to lie on the axis of whirling at the other end; note that this constraint requires a non-zero tension at this end. Under these conditions, he obtained closed form solutions for the modes of free whirling of the string. Investigating the stability of the solutions, he demonstrated that the perturbed motions were Lyapunov stable: points of the string that are initially within a certain distance from the steady-state mode shapes continue to remain within this distance. The nonlinear eigenvalue problem associated with steady-state whirling of the string results in a two-point boundary value problem; solution of the two-point boundary value problem can be obtained by suitable numerical methods, such as the shooting method, the finite difference method, and so on. Coomer *et al.*, [27] have recently revisited this problem and obtained such numerical solutions with MAPLE.

In contrast to the taut string problem, very little experimental work has been reported in the literature concerning whirling of a hanging string. Western [90] used his wife's necklace chain as an example of an inextensible and flexible string; he was able to show that the natural modes of the rotating vertical chain corresponding to small amplitudes resembled the zero order Bessel function of the first kind, this is, in fact, a simple and beautiful experimental demonstration of Bessel's function. Careful examination of his photographs indicates that beyond the second mode, the natural modes may not have been achieved in the experiment. Howell and Triantafyllou [49] have addressed the related problem of a hanging chain under in-plane harmonic excitation; through asymptotic analysis and numerical simulations they found that at large excitation amplitudes, stable as well as unstable steady-state solutions exist in both two and three-dimensions. Coomer *et al.*, [27] used flash photography to identify the number of nodes at any given frequency of rotation and indicated that the number of nodes varied even under the same rotational frequency suggesting that the string possesses multiple solutions at each rotating frequency. In this sense, the experimental research on strings under rotary or planar harmonic excitation at one end and free at the other has been qualitative in nature.

The dynamics of filaments has also been studied for quite a long time and with renewed interest recently due to its potential applications in biological problems. The classical theory of the finite motion of the slender rods was developed by Kirchhoff about 150 years ago, presented in detail by Love [62], and recently reviewed by Dill [31]. While there is a large number of investigations dealing with the motion of perfectly flexible strings as summarized above, relatively little work has been done on the motion of filaments with nonnegligible bending stiffness. Goriely and Tabor [38–41] studied the nonlinear dynamics of filaments based on the Kirchhoff's rod equations in a series of papers: they studied the stability of various stationary solutions, such as planar ring and straight rod, subject to twisting perturbations. They also proved the existence of dynamical instabilities and provided the selection mechanism for the shape of unstable filaments. Then, they performed a nonlinear analysis of the motion of a straight rod and showed that the motion can be described by a pair of nonlinear Klein-Gordon equations which couple the local deformation amplitude to the twist density. The existence of pulse-like and front-like traveling wave solutions has also been found in their analysis. Finally, they studied the instabilities of helical rods and showed that helices without terminal forces are always dynamically stable.

1.2 Microscopic One-Armed Swimmers at Low-Reynolds Number

Many micro-organisms in nature propel themselves by spinning or beating their appendices - cilia or flagella [11]. For instance, bacteria rotate their basal motor to spin their relatively rigid helical flagella for their swimming [6]. In contrast, eukaryotic sperms beat their relatively soft flagella for swimming when adenosine triphosphate (ATP) is sufficiently presented in the solvent and thus activates the dynein motors [61]. Recently, a microscopic artificial one-armed swimmer has been demonstrated experimentally [33], which mimics some aspects of the motion of microorganisms but with externally driven magnetic forcing. Modeling the propulsion of such micro-swimmers has attracted a lot of interest from the biophysics community in past decades [4, 20, 45, 63, 77, 84, 85, 91]. For these micro-swimmers, with length $L \sim 10 \mu m$, swimming velocity $V_0 \sim 10^2 \mu m/s$, mass density of fluid $\rho \sim 10^3 kg/m^3$ and fluid viscosity $\mu \sim 10^{-3} N \cdot s/m^2$, the Reynolds number is estimated as $Re = \rho V_0 L/\mu \sim 10^{-3} << 1$. Hence, motion of such micro-swimmers is well characterized by low-Reynolds-number hydrodynamics [77,85]. This is fundamentally different from the macroscopic animal kingdom as inertial effects are negligible and viscous drag dominates their motion. The propulsive force in such micro-swimmers is purely the result of the anisotropy of the hydrodynamic drag in the local normal (η_n) and tangential (η_t) directions, i.e. $\eta_n > \eta_t$ [45].

Eukaryotic sperm flagella have a complex 9+2 axonemal structure [61,72]. The nine circumferentially distributed doublet microtubules are connected to each other by the nexin links and to the central pair of singlet microtubules by radial spoke proteins. Dynein motors are distributed periodically along the length of the microtubules; these generate propulsive forces with sufficient concentration of adenosine triphosphate (ATP) in the solution. The formation of cross-bridges between the dynein and the microtubules is thought to generate relative sliding between microtubules that results in the generation of a bending wave along the flagellum [11,14,15,59]. Thus, the flagellum can then be modelled as an internally driven filamentary structure. Such models have been suggested for the operation of the dynein motors [20,21]. The coupling of the internal force generation to the movement requires a model of the elastic deformable element that provides both the physical structure to the flagellum and the interaction with the fluid. Previous studies of these aspects have concentrated on modelling the flagellum by considering the bending deformations of the microtubule structure of the flagellum.

Early investigators in this area focused on the hydrodynamics of the problem [45,46]. More recently, attention has been directed towards the structural and mechanical aspects of the problem. In his classic lecture [77], *Life at Low Reynolds Number*, Purcell proposed a simple swimming mechanism at low-Reynolds number called the “three-link swimmer”, which is the fundamental swimming mechanism in an inertialess environment; this simplified model can be used to gain an understanding of the underlying mechanics of the motion of sperm flagellum without getting involved in the details of the mechanisms of force generation and the structural intricacies of the flagellum, but more sophisticated models are required when quantitative estimates are to be made of the propulsion. Recent studies have optimized this three-link swimmer geometrically [4] and kinematically [84]. Through many studies of dynamics of the elastic micro-filaments at low-Reynolds number, it has been shown that self-organized beating can lead to the self-propulsion of the filament [20, 21, 63, 91, 92]. Specifically, Wiggins and Goldstein [91, 92] considered small-amplitude oscillatory motion of a filament with small bending stiffness in a viscous fluid; the resulting hyperdiffusion problem was examined to show that propulsive force could be generated by such bending oscillations. Camalet *et al.* [20, 21] used essentially the same model for the elastic deformation of the flagellum, but incorporated into the dynamic equations a sliding model for the internally generated forces; they showed that propagating wave solutions that can propel the filament appear via a Hopf bifurcation. Axial force was incorporated in their model, but neglected after the geometric linearization [20]. Lowe [63] generalized these ideas by performing numerical simulations of the nonlinear equations of the dynamics of filaments; filament elasticity was modelled by incorporating both tension and bending effects, and active forces were simply prescribed as propagating quadrupoles. He demonstrated that indeed self-propulsion is possible within this model; more importantly, he concluded that a quantitative matching of experimentally observed flagellar shapes was only possible if the bending forces on the filament were far greater than the viscous forces. Specifically, this requires the bending stiffness of the flagella to be about three to four orders of magnitude larger than the experimental data commonly reported by numerous investigators [50,60,73,74]. Lowe suggested either that the living sperm flagellum is stiffer or that some active mechanism is present [63].

1.3 Overview of Present Work

In this dissertation, the motion of flexible strings with zero bending stiffness and thin filaments with nonnegligible bending stiffness in two different regimes - inertial and low-Reynolds-number - has been investigated. The thesis is organized as follow:

In chapter 2, theoretical analysis of the free and forced responses of a flexible string under self-weight and subjected to both harmonic rotary excitation and planar harmonic excitation at one end and left free at the other in inertial field with gravity are presented first. Specifically, a perturbation approach is applied to analyze the forced response of a string subjected to planar harmonic excitation. Second, quantitative experimental investigations on the rubber strings is conducted utilizing a stereo-vision imaging system. Steady motions as well as nonsteady motions are observed in the experiments. Finally, comparison between the experimental results with the theoretical analysis is studied.

In chapter 3, the motion of linear elastic filaments under self-weight with either rotary excitation or planar harmonic excitation at one end and free at the other is examined based on the Kirchhoff's slender rod theory; specifically, the effect of bending stiffness is investigated both theoretically and experimentally. Similarities between the problem of a perfectly flexible string and filament with nonnegligible bending stiffness are exploited in identifying the possible modes of oscillation. The theoretical predictions are compared with the experimental results for filaments with different bending stiffness to demonstrate the effect of bending directly.

In chapter 4, we study the two-dimensional dynamics of an Euler elastica in low-Reynolds number regime and show that the effect of tension is comparable to or dominates over the bending contributions for the microfilaments with small bending stiffness in the range of 10^{-24} to $10^{-21} N \cdot m^2$. Then, we propose a new control mechanism, which uses tension as a parameter, to alter the effective bending stiffness, and as a consequence control the swimming velocity and the propulsion efficiency.

In chapter 5, the low-Reynolds number dynamics of a micro-string is investigated, in order to understand the fundamental physics underpinning the self-propulsion and the generation of swimming patterns of the microscopic natural swimmers: eukaryotic sperm flagella. Both linear analysis of small-amplitude swimming and numerical simulation of the fully nonlinear governing equations show that the time-reversal symmetry is broken, which leads to propulsion. Numerical studies are performed for different boundary conditions and different forcing levels. The swimming velocity and propulsion efficiency have been calculated for different "string sperm number" S_t. The comparison between the simulation results and the experimentally observed waveforms of the sperm flagellar motion show excellent agreement. Comparison with previous bending models illustrated that, for the same equivalent bending stiffness and loading condition, the micro-string has higher propulsion efficiency with similar swimming velocity.

In chapter 6, we summarize the main results and describe some proposals for future work.

Chapter 2

Planar and Whirling Motions of Flexible Strings

In this chapter, we examine the dynamics of a string hanging under self-weight and free of constraint at one end under either rotary excitation or planar, harmonic excitation at the other end[1]. A review of the formulation and solution of the equations of motion for the whirling string is provided in Section 2.1 to set the stage for our presentation. In Section 2.2, we review the governing equations and perform the asymptotic analysis for the forced response of the in-plane excitation problem. The experimental tasks of identifying an appropriate string that satisfies the assumptions of the theory, the assembly of the apparatus to provide appropriate control over the imposed twirling motion and planar harmonic excitation, and the determination of the spatial variation of the string during the experiment are described in detail in Section 2.3. In Section 2.4, we describe the experimental results and then provide a comparison to the linear and nonlinear theories of whirling. A number of interesting deviations from the steady-state solution assumed in the theoretical formulation are also described in this section. The experimental results and comparison to the theoretical analysis for the case of the in-plane harmonic excitation are examined in Section 2.5.

---

[1] Some of the contents of this chapter have been published in *J. Appl. Mech. - T ASME*, **73**, 842-851 (2006).

2.1 Analysis of a Whirling String

Consider a string of length L, free at one end and attached at the other end to the shaft of a rotating motor. For a string with negligible bending stiffness, the only elastic force is internal tension which is along the local tangent direction. This is the setting in which Kolodner [55] formulated the nonlinear problem of a whirling string; we will review this formulation in this section.

2.1.1 Equations of Motion

Let $\mathbf{r}(s,t)$ be the position vector of any point of the string; s is the Lagrangian coordinate measured from the free end of the string and t represents time.

$$\mathbf{r}(s,t) = X_i\hat{\mathbf{e}}_i = x_i\hat{\mathbf{b}}_i \tag{2.1}$$

where $\hat{\mathbf{e}}_i$[2] is the Newtonian reference frame, and $\hat{\mathbf{b}}_i$ is the current frame associated with the rotating axis and X_i and x_i are the components of $\mathbf{r}$ in the two frames, respectively. A sketch of the deformed shape of the string and the coordinate systems is shown in Figure 2.1. The only forces acting on any segment of the string as it executes a rotational motion imposed on it about the axis $\hat{\mathbf{n}}_3$ are the body force on the string and the internal tension in the string. The body force per unit length is taken to be $\mathbf{f}(s,t)$. The tension in the string must always be along the tangent to the string and is represented as $\mathbf{T}(s,t)$. Therefore the tension can be written as

$$\mathbf{T}(s,t) = T(s,t)\hat{\mathbf{t}}(s,t) = \frac{T(s,t)}{|\mathbf{r}'(s,t)|}\mathbf{r}'(s,t) \tag{2.2}$$

---

[2] We use standard index notation with Latin indices taking the range 1, 2, 3 and Greek indices taking the range 1, 2. The repeated index indicates summation over the range of the index.

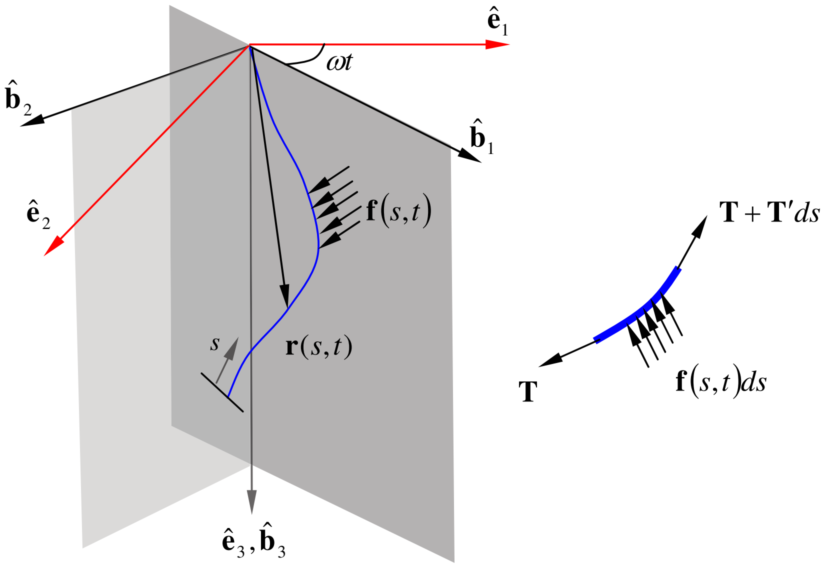

Figure 2.1: Motion configuration of the string.

where $\hat{\mathbf{t}}(s,t)$ is the unit vector tangent to the string, $T(s,t)$ is the magnitude of the tension, and prime denotes the derivative with respect to s. Compared to the transverse deflection, the longitudinal extension of the string is negligible such that the inextensibility equation $|\mathbf{r}'(s,t)| = 1$ holds; while this inextensibility is not essential, it makes the problems simpler. Antman and Reeken [2] have examined the problem of whirling while drawing simultaneously. In the experiments described in the present work, the extension of the string was shown to be negligible through direct measurements.

Consider the free-body-diagram of an infinitesimal segment ds of the string, as shown in the Figure 2.1. The general equations of motion for this infinitesimal segment can be expressed as

$$\mathbf{T}'(s,t) + \mathbf{f}(s,t) = \rho\ddot{\mathbf{r}}(s,t) \tag{2.3}$$

where ρ is the mass density per unit length of the string. The string is assumed to be set in motion in air, but the speed of motion is considered to be low enough to neglect air resistance; therefore, the only component of body force on the string is its own weight given by

$$\mathbf{f} = \rho g \hat{\mathbf{e}}_3 = \rho g \hat{\mathbf{b}}_3 \tag{2.4}$$

where g is the acceleration due to gravity. Eq.(2.3) can now be rewritten in component form in the $\hat{\mathbf{e}}$-frame

$$\begin{cases} \rho \ddot{X}_1 = (TX_1')' \\ \rho \ddot{X}_2 = (TX_2')' \\ \rho \ddot{X}_3 = (TX_3')' + \rho g \end{cases} . \tag{2.5}$$

The inextensibility constraint is also written in terms of components as

$$X_1'^2 + X_2'^2 + X_3'^2 = 1. \tag{2.6}$$

Eqs. (2.5) and (2.6) are the governing differential equations for the three dimensional motion of the string.

2.1.2 Nonlinear Eigenvalue Problem

Kolodner [55] and Caughey [23] investigated steady-state solutions to the whirling problem posed above assuming that the following steady-state motion exists

$$\begin{cases} X_1(s,t) = X(s)\cos\omega t \\ X_2(s,t) = X(s)\sin\omega t \\ X_3(s,t) = Z(s) \\ T(s,t) = T(s) \end{cases} . \tag{2.7}$$

It is readily seen that Eq. (2.7) represents motion of the string in a plane, with the plane rotating about the $\hat{\mathbf{e}}_3$ axis at the frequency ω. $X(s)$ is the amplitude in this vertical plane. Introducing Eq. (2.7) into the governing differential equations of motion in Eqs. (2.5) and (2.6), we obtain

$$\begin{cases} (TX')' + \rho\omega^2 X = 0 \\ (TZ')' + \rho g = 0 \\ X'^2 + Z'^2 = 1 \end{cases} . \tag{2.8}$$

The necessary boundary conditions are the following: the tension is zero at the free end ($s = 0$): $T(0) = 0$, and the string is fixed at $s = L$: $X(L) = Z(L) = 0$. Through a change of variable $u(s) = \frac{TX'}{\rho g}$, the above equations can be simplified as follows

$$u''(s) + \frac{\omega^2}{g}\frac{u(s)}{\sqrt{u^2(s) + s^2}} = 0 \tag{2.9}$$

The boundary conditions can now be written in terms of the transformed variable u as follows

$$u(0) = u'(L) = 0. \tag{2.10}$$

Equations (2.9) and (2.10) can be nondimensionalized with $\hat{s} = s/L$ and $\hat{u} = u/L$, to yield

$$\frac{d^2\hat{u}}{d\hat{s}^2} + \hat{\omega}^2 \frac{\hat{u}}{\sqrt{\hat{u}^2 + \hat{s}^2}} = 0 \tag{2.11}$$

where $\hat{\omega} = \omega\sqrt{\frac{L}{g}}$, and

$$\hat{u}(0) = 0, \frac{d\hat{u}(1)}{d\hat{s}} = 0. \tag{2.12}$$

Equation (2.11) together with Eq. (2.12) constitutes a nonlinear eigenvalue problem. It can also be treated as a nonlinear two-point boundary value problem for prescribed $\hat{\omega}$ and solved numerically by using finite difference or shooting methods. Once we have the solution $\hat{u}(\hat{s})$, other components of the solution for such a steady-state whirling can be obtained. In particular,

$$T(s) = \rho g\sqrt{u^2(s) + s^2}, \tag{2.13}$$

$$X(s) = -\frac{g}{\omega^2}u' = -\int_s^L \frac{u(\xi)}{\sqrt{u^2(\xi)+\xi^2}}d\xi \tag{2.14}$$

and

$$Z(s) = \int_s^L \frac{\xi}{\sqrt{u^2(\xi)+\xi^2}}d\xi. \tag{2.15}$$

We will first examine the linearized problem and then discuss the nonlinear problem.

2.1.3 Small Amplitude Whirling

For $\hat{u} << 1$, the above nonlinear eigenvalue problem (eq. (2.11)) can be reduced to a linear eigenvalue problem

$$\hat{s}\frac{d^2\hat{u}}{d\hat{s}^2} + \hat{\omega}^2\hat{u} = 0. \tag{2.16}$$

Equation (2.16) is a Bessel equation. Its solution can be written as

$$\hat{u}(\hat{s}) = \sqrt{\hat{s}}AJ_1(2\hat{\omega}\sqrt{\hat{s}}) + \sqrt{\hat{s}}BY_1(2\hat{\omega}\sqrt{\hat{s}}) \tag{2.17}$$

where J_1 and Y_1 are the Bessel functions of the first kind and second kind of order one. From the first of the boundary conditions in Eq. (2.12), we see that the second term must be discarded since $Y_1(2\hat{\omega}\sqrt{\hat{s}}) \longrightarrow \infty$ as $\hat{s} \longrightarrow 0^+$. Also, A has nontrivial values only at discrete whirling frequencies (eigenfrequencies of the system) given by the zeros of J_1. The general solution can then be written as the superposition of the eigenmodes corresponding to the eigenfrequencies:

$$\hat{u}(\hat{s}) = \sum_{n=1}^{\infty} \sqrt{\hat{s}}A_n J_1(2\hat{\omega}_n\sqrt{\hat{s}}) \tag{2.18}$$

where A_n are the amplitudes to be determined and $J_0(2\hat{\omega}_n) = 0$ provides the roots $\hat{\omega}_n$. Finally, the solution for the linearized problem for the fundamental mode $n = 1$ can be written in terms of the string coordinates as:

$$\begin{cases} Z(s) \approx L - s \\ X(s) = -\frac{g}{\omega^2}u' \approx -\frac{LA}{\hat{\omega}_1} J_0(2\hat{\omega}_1\sqrt{\frac{s}{L}}) \end{cases} . \tag{2.19}$$

The main upshot of this analysis is that *the string can whirl at steady-state only at fixed frequencies* ω_n. Casual observation of string whirling, however, suggests that the string can indeed whirl at any frequency; this observation prompted Kolodner first, and others later, to look for steady-state solutions from the complete equation of motion in Eqs. (2.11) and (2.12).

2.1.4 Large Amplitude Whirling

When $\hat{u}$ is not small, the nonlinear eigenvalue problem in Eqs. (2.11) and (2.12) must be solved. Kolodner [55] showed that whenever $\omega_n < \omega < \omega_{n+1}$, steady-state whirling can occur at any of the n eigenmodes. Caughey [24] examined this problem thoroughly, but with the end $s = 0$ constrained to remain along the initial vertical line; this requires a non-zero tension to appear at this end. Caughey [24] showed that steady whirling cannot occur for $\omega < \omega_1$, that unique periodic solutions exist for arbitrary rotational speed and that the solutions are stable. He also obtained closed-form solutions to the nonlinear problem in terms of Jacobi elliptic functions. Very recently, Coomer *et al.*, [27] showed that the two-point boundary value problem in Eqs. (2.11) and (2.12) could be solved using the *shooting method* implemented in Maple. We determined the solution to the whirling problem in MATLAB. In order to obtain these solutions to the nonlinear problem, we start the numerical solution procedure with different initial guesses for the shape of the string; in particular the mode shape of the linearized eigenvalue problem can be used as an initial guess. For a prescribed initial tip amplitude, the program searches for the eigenvalue at which the solution is obtained. In Fig. 2.2, the amplitude at the tip of the string, A (or $X(0)$)

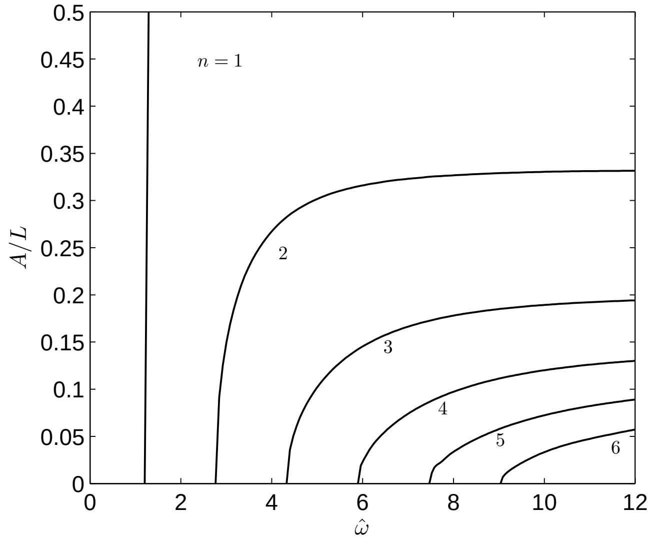

Figure 2.2: Variation of the tip amplitude with frequency of whirling for the different modes. The first mode has a horizontal asymptote at $A/L \approx 1$ and hence is not shown completely.

corresponding to each frequency ω is shown. As an illustration, the corresponding mode shapes for whirling frequency $\omega = 60 rad/s$ are shown in Fig. 2.3. Clearly, for any frequency $\omega_n < \omega < \omega_{n+1}$, there are n mode shapes and corresponding amplitudes. The variation of the tension in the string along its length normalized by the weight of the string $\rho g L$ is shown in Fig. 2.4. The tension takes on its maximum value, significantly larger than the static value for the lower modes, at the nodes and is equal to the static value at points with a vertical tangent. The main result of this exercise is that for the nonlinear problem, *at each frequency of whirling, there are a number of discrete modes at which steady-state whirling can occur*. The amplitude of whirling is determined by the mode.

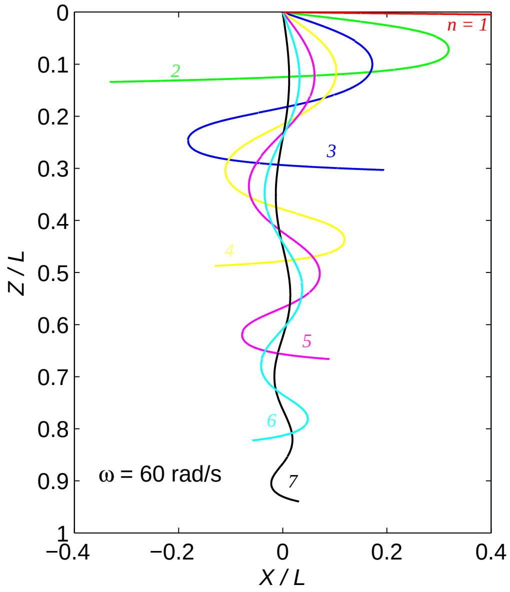

Figure 2.3: Mode shapes determined from the nonlinear analysis. Whirling frequency $\omega = 60 rad/s$. The first mode appears nearly horizontal and hence is not completely shown in this figure.

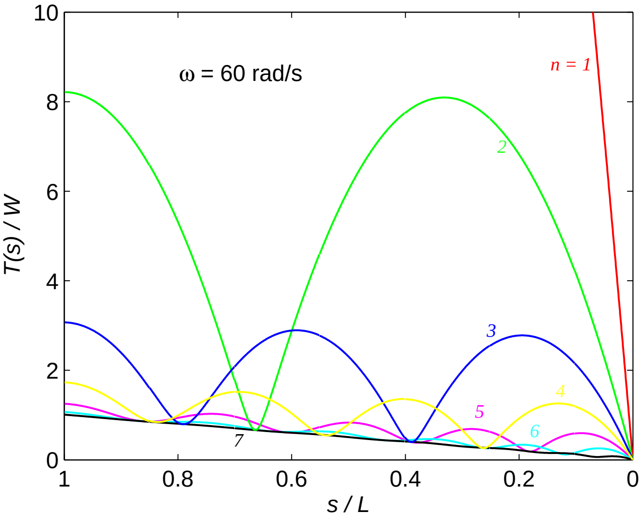

Figure 2.4: Variation of tension (normalized by the weight) along the length of the string for different modes as shown in Fig. 2.3.

2.1.5 Forced Whirling

Caughey [23] considered approximate non-linear solutions for the forced whirling of the string; he further examined the stability of such motions. We summarize his results for use in interpretation of our experimental results. Consider that the rotational motion is imposed at the upper end of the string by fixing it at a distance (δ) from the axis of rotation. Then, the solution to the forced nonlinear problem near any natural frequency $\hat{\omega}_n$ can be written as

$$X(s) = \delta + A_n J_0\big(2\hat{\omega}_n\sqrt{\frac{s}{L}}\big). \tag{2.20}$$

Typically, a summation of the normal modes would be used to represent the shape under forced oscillations, but since the resulting nonlinear equations are quite difficult to solve, Caughey [23] suggested considering only the n^{th} mode when the driving frequency is in the neighborhood of $\hat{\omega}_n$; this places a restriction on the magnitude A_n, but this is not of major consequence here. Eliminating Z between the second and third of Eq. (2.8), the tension in the string may then be written as

$$T(s) = \frac{\rho g s}{\sqrt{1-[X'(s)]^2}} = \frac{\rho g s}{\sqrt{1-A_n^2[J_0'(2\hat{\omega}_n\sqrt{s/L})]^2}}. \tag{2.21}$$

In order to determine the amplitude A_n, we first substitute Eq. (2.21) into Eq. (2.8), then multiply by $J_0(2\hat{\omega}_n\sqrt{s/L})$ and integrate with respect to s over $[0, L]$. The first term of the resulting equation is integrated by parts, and after substitution of limits and a change of variable $\xi = \sqrt{s/L}$, we get

$$\frac{A_n}{L}\left(\int_0^1 \xi J_0^2\left(2\hat{\omega}_n\xi\right)\,d\xi - \frac{\hat{\omega}_n^2}{\hat{\omega}^2}\int_0^1 \frac{\xi J_1^2\left(2\hat{\omega}_n\xi\right)}{\sqrt{1-A_n^2\hat{\omega}_n^2/L^2\left(J_1\left(2\hat{\omega}_n\xi\right)/\xi\right)^2}}\,d\xi\right) \tag{2.22}$$
$$+\frac{\delta}{L}\int_0^1 \xi J_0\left(2\hat{\omega}_n\xi\right)\,d\xi = 0,$$

which is a nonlinear equation for A_n; the first and third terms can be integrated

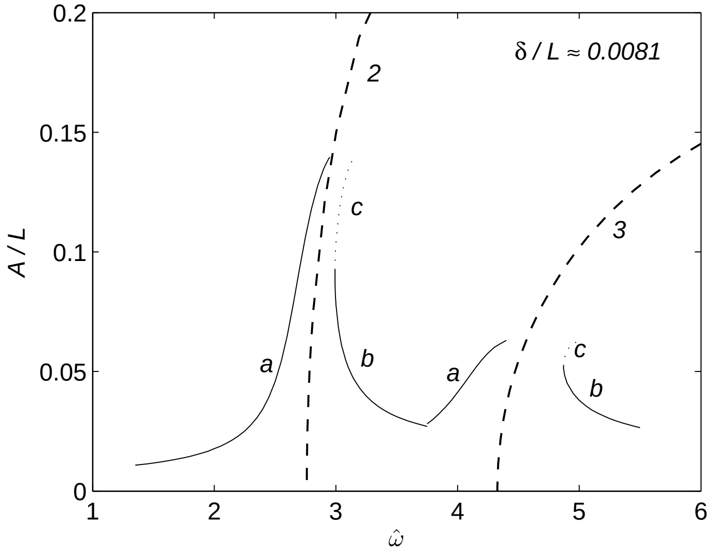

Figure 2.5: Variation in the amplitude with the frequency for forced motion of the string near the 2^{nd} and 3^{rd} natural frequencies. Dash lines are the solutions of the free motion.

explicitly and then Eq. (2.22) can be solved numerically for A_n at each given ω. This solution is shown in Fig. 2.5 for frequencies in the neighborhood of the 2^{nd} and 3^{rd} natural frequencies. This solution is not unlike the simple nonlinear response of the Duffing equation and hence one would expect similarities such as unstable branches and hysteretic behavior. Investigation [23] on the stability of these solution branches showed that a and b are stable while c is unstable. Upon increasing the frequency, the amplitude will follow branch a and at some level of amplitude - dictated by inherent damping - jump to branch b while upon decreasing the frequency, the amplitude will follow the branch b until some frequency and then jump to branch a. Of course, this applies only for small amplitude whirling due to the approximate nature of the solution used in Eq. (2.20).

2.2 Analysis of the Motion of a String Under Planar Excitation

2.2.1 Equations of Motion

Due to the intrinsic similarity, the equations of motion of the string under planar excitation at one end and free at the other are same as that for the whirling string in Eq. (2.3). It is important to note that even though we consider an imposed 2D harmonic motion lying in the (X_1, X_3) plane, we do not take $X_2 = 0$; since there are no constraints on the motion of the string in the X_2 direction, it is free to take a general 3D motion shape. In the following, we will first consider two possible steady-state motions for the free response - 2D oscillation and 3D whirling response - and then examine the forced response.

2.2.2 Steady-State Free Response

As observed in the experiments, there are two possible steady-state responses for the string, namely, 2D oscillations and 3D whirling motion

$$\begin{cases} X_1(s,t) = X(s)\cos\omega t \\ X_2(s,t) = 0 \\ X_3(s,t) \approx Z(s) \end{cases} \tag{2.23}$$

and

$$\begin{cases} X_1(s,t) = X(s)\cos\omega t \\ X_2(s,t) = X(s)\sin\omega t \\ X_3(s,t) = Z(s) \end{cases} . \tag{2.24}$$

Thus, for both cases, equation (2.3) can be simplified as:

$$\begin{cases} (TX')' + \rho\omega^2 X = 0 \\ (TZ')' + \rho g = 0 \\ X'^2 + Z'^2 = 1 \end{cases} . \tag{2.25}$$

For the 2D oscillatory response, the assumption $X_3(s,t) \approx Z(s)$ is an approximation since the inextensibility constraint is satisfied only approximately through this type of assumption. Equation (2.25) represents the envelope of the mode shapes; these equations are identical to the equations that describe steady-state 3D whirling motion of the string as discussed in Section 2.1.2. For the 3D whirling motion, Eq. (2.25) describe the motion in the (X, Z) plane, which rotates about the $X_3(or Z)$ axis at frequency ω. For the free motion, the boundary conditions can be written as:

$$\begin{cases} X(L,t) = 0 \\ Z(L,t) = 0 \\ T(0,t) = 0 \end{cases} . \tag{2.26}$$

An approach similar to the one developed by Kolodner [55] and reviewed in Section 2.1.2 will be used in order to simplify Eq. (2.25). Through a change of variable $u(s) = TX'/\rho g$ and then normalization with $\hat{s} = s/L$ and $\hat{u} = u/L$, then equation (2.25) can be reduced to

$$\frac{d^2\hat{u}}{d\hat{s}^2} + \hat{\omega}^2 \frac{\hat{u}}{\sqrt{\hat{u}^2 + \hat{s}^2}} = 0 \tag{2.27}$$

where $\hat{\omega} = \omega\sqrt{L/g}$; the boundary conditions can also be written in terms of the normalized variables as

$$\begin{cases} \hat{u}(0) = 0 \\ \frac{d\hat{u}}{d\hat{s}}(1) = 0 \end{cases} . \tag{2.28}$$

Equation (2.27) together with (2.28) constitutes a nonlinear eigenvalue problem. It can also be treated as a nonlinear two-point boundary value problem for prescribed $\hat{\omega}$ and solved numerically by using finite difference or shooting method [27]. Depending on whether the solutions are interpreted through Eqs. (2.23) or (2.24), we have solutions for planar or 3D motion. Once we have the solution for $\hat{u}(s)$, other components of the solution, i.e. mode shape (X, Z) and internal tension T, for such a steady-state motion can be obtained easily, as discussed in Eqs. (2.13), (2.14), and (2.15).

The linearized problem for $\hat{u} \ll \hat{s}$ has been addressed by many authors [27, 79, 90] and was reviewed in Section 2.1.3. The main upshot of the linear analysis is that *the string can be excited into a steady-state motion only at its eigenfrequencies:* $\omega_n = \hat{\omega}_n \sqrt{g/L}$, where $\hat{\omega}_n$ are the roots of $J_0(2\hat{\omega}_n) = 0$. Here, the subscript n indicates the mode number. For $\hat{u}$ not small compared to $\hat{s}$, the full nonlinear eigenvalue problem in Eqs. (2.27) and (2.28) must be solved numerically. In order to obtain these solutions, we start the numerical simulation procedure with different initial guesses for the mode shape; in particular the mode shape of the linearized eigenvalue problem can be used as an initial guess. For a prescribed amplitude of the free end, the program searches for the normalized frequency $\hat{\omega}$ at which the solution is obtained. The solutions obtained are similar to the whirling solution and will be discussed along with the forced response in Fig. 2.6.

2.2.3 Forced Response of a String: Perturbation Analysis

For the string subjected to a forced planar excitation, the boundary conditions are

$$\begin{cases} X_1(L,t) = \epsilon^3 X_0 \cos(\omega t) \\ X_2(L,t) = X_3(L,t) = 0 \\ T(0,t) = 0 \end{cases} \tag{2.29}$$

where ω is the driving frequency, X_0 is the excitation amplitude and is a small number compared to the length L of the string, and ϵ is the artificially introduced perturbation parameter[3]. Nayfeh [69] investigated the forced response of a taut

---

[3] Since the perturbation method is so powerful for solving the nonlinear differential equations, we introduce the perturbation parameter ϵ, so that we can find the asymptotic solutions to the equations associated with the forced response of the problem. Finally, we set $\epsilon = 1$ to recover the original problem [5].

string under planar excitation by using the standard perturbation expansion to linearize the problem and then the method of multiple-time scales to extract the long time response; he found that as the excitation frequency approaches the natural frequency of the string, the planar motion becomes unstable, and the solution turns out to be 3D motion. Triantafyllou and Howell [49, 86] studied the resulting motion for a hanging chain under planar excitation at the upper end in the gravitational field and found the similar characteristic as the taut string. However, they did the analysis for the velocity fields in the local coordinate system and it is hard to compare the experimental results to their analysis directly. Hence, we use the same approach to analyze the position of the string in the global coordinate system for easy quantitative comparison to our experimental results.

First, let us consider the asymptotic solutions for the free motion. For consistency, we choose the following perturbation expansion

$$\begin{cases} X_1(s,t) = \epsilon x_1(s,t) + \epsilon^3 x_3(s,t) + O\left(\epsilon^5\right) \\ X_2(s,t) = \epsilon y_1(s,t) + \epsilon^3 y_3(s,t) + O\left(\epsilon^5\right) \\ X_3(s,t) = L - s + \epsilon^2 z_2(s,t) + O\left(\epsilon^4\right) \\ T(s,t) = \rho g s + \epsilon^2 T_2(s,t) + O\left(\epsilon^4\right) \end{cases} . \tag{2.30}$$

Clearly, the zeroth order solution corresponds to the string hanging vertically down under its own weight, without any motion. Substituting Eq. (2.30) into the governing equations of motion (Eq. (2.5)) and collecting terms with same order in ϵ, we obtain the first and second order perturbation equations

$$\begin{cases} g\left(s x_1'\right)' = \ddot{x}_1 \\ g\left(s y_1'\right)' = \ddot{y}_1 \end{cases} \tag{2.31}$$

and

$$\begin{cases} T_2' = \rho\left[g\left(s z_2'\right)' - \ddot{z}_2\right] \\ z_2' = \frac{1}{2}\left[\left(x_1'\right)^2 + \left(y_1'\right)^2\right] \end{cases} . \tag{2.32}$$

The solutions of Eq. (2.31) that obey the fixed end boundary conditions are

$$\begin{cases} x_1(s,t) = X(t) J_0\left(\zeta\right) \\ y_1(s,t) = Y(t) J_0\left(\zeta\right) \end{cases} \tag{2.33}$$

where $J_0\left(\zeta\right)$ is the Bessel function of first kind of order zero, $\zeta = 2\hat{\omega}_n\sqrt{s/L}$, and $\hat{\omega}_n = \omega_n\sqrt{L/g}$. The boundary conditions in Eq. (2.26) leads to $J_0\left(2\hat{\omega}_n\right) = 0$, which gives us the natural frequency ω_n of free motion of a hanging string. This is consistent with the linear analysis of the free motion of a hanging string in Section 2.2.2.

Next, introducing Eq. (2.33) into (2.32), we find the solutions for $z_2(s,t)$ and $T_2(s,t)$

$$\begin{cases} z_2(s,t) = & \frac{\hat{\omega}_n^2}{2L}\left(X^2+Y^2\right)\left[J_1^2\left(\zeta_L\right) - J_0^2\left(\zeta\right) - J_1^2\left(\zeta\right)\right] \\ \\ T_2(s,t) = & \frac{\rho g \hat{\omega}_n^2}{2L}\left(X^2+Y^2\right) J_1^2\left(\zeta\right) - \frac{\rho\zeta}{4}\left(\dot{X}^2 + X\ddot{X} + \dot{Y}^2 + Y\ddot{Y}\right) \\ & \left[\xi J_1^2\left(\zeta_L\right) - 2\zeta\left[J_0^2\left(\zeta\right) + J_1^2\left(\zeta\right)\right] + 2J_0\left(\zeta\right)J_1\left(\zeta\right)\right] \end{cases} \tag{2.34}$$

where $\zeta_L = 2\hat{\omega}_n$. Then, for the forced response, we use the following approximations

$$\begin{cases} X_1(s,t) \approx \epsilon x_1(s,t) + \epsilon^3 X_0 \cos\left(\omega t\right) \\ X_2(s,t) \approx \epsilon y_1(s,t) \\ X_3(s,t) \approx L - s + \epsilon^2 z_2(s,t) \\ T(s,t) \approx \rho g s + \epsilon^2 T_2(s,t) \end{cases} . \tag{2.35}$$

Introducing Eqs. (2.33), (2.34) and (2.35) into Eq. (2.5) and keeping terms up to third order (ϵ^3), then through the standard Galerkin's procedure to eliminate the spatial dependence, we obtain two ordinary differential equations for $X(t)$ and $Y(t)$; these equations are then correct to third order in ϵ. Before proceeding further, the equations are normalized by setting $\hat{t} = \omega_n t$, $\hat{X} = X/L$, $\hat{Y} = Y/L$, $\hat{\omega} = \omega\sqrt{L/g}$, $\hat{X}_0 = X_0/L$ and then dropping the hats in all terms except $\hat{\omega}$ and

$\hat{\omega}_n$. The resulting normalized equations are

$$\begin{cases} \ddot{X} + X = & \epsilon^2[\beta_1\left(X^3 + XY^2\right) + \beta_2\left(X\dot{X}^2 + X^2\ddot{X} + X\dot{Y}^2 + XY\ddot{Y}\right) \\ & +2\left(\frac{\hat{\omega}}{\hat{\omega}_n}\right)^2 f\cos\left(\frac{\hat{\omega}}{\hat{\omega}_n}t\right)] \\ & \\ \ddot{Y} + Y = & \epsilon^2\left[\beta_1\left(X^2Y + Y^3\right) + \beta_2\left(Y\dot{X}^2 + XY\ddot{X} + Y\dot{Y}^2 + Y^2\ddot{Y}\right)\right] \end{cases}, \quad (2.36)$$

in which the coefficients are

$$\begin{aligned} \beta_1 &= 2\hat{\omega}_n^4\frac{\alpha_1}{\alpha_0} \\ \beta_2 &= 4\hat{\omega}_n^4\frac{\alpha_2}{\alpha_0} \\ f &= \frac{X_0}{2}\frac{\alpha_3}{\alpha_0} \end{aligned} \quad (2.37)$$

and

$$\alpha_0 = \int_0^{\zeta_L}\zeta J_0^2\left(\zeta\right)\,d\zeta = \frac{1}{2}\zeta_L^2 J_1^2\left(\zeta_L\right)$$

$$\alpha_1 = \int_0^{\zeta_L}\zeta^{-2}J_0\left(\zeta\right)J_1^2\left(\zeta\right)\left[4J_1\left(\zeta\right) - 3\zeta J_0\left(\zeta\right)\right]\,d\zeta$$

$$\alpha_2 = \int_0^{\zeta_L}\left[\zeta^{-1}J_1\left(\zeta\right)h_2\left(\zeta\right)\right]'J_0\left(\zeta\right)\,d\zeta$$

$$\alpha_3 = \int_0^{\zeta_L}\zeta J_0\left(\zeta\right)\,d\zeta = \zeta_L J_1\left(\zeta_L\right) \quad (2.38)$$

where

$$h_2\left(\zeta\right) = \frac{1}{2}\int_0^{\zeta}\xi\left[J_1^2\left(\zeta_L\right) - J_0^2\left(\xi\right) - J_1^2\left(\xi\right)\right]\,d\xi. \quad (2.39)$$

In order to analyze the possible steady-state solutions for Eq. (2.36), we use the standard method of multiple time scales [5, 69] by introducing two time scales, namely, $\tau_0 = t$ and $\tau_1 = \epsilon^2 t$; τ_1 is expected to capture the long time behavior appropriately. Therefore, $X(t)$ and $Y(t)$ are written as

$$\begin{cases} X(t) = X\left(\tau_0, \tau_1\right) = A_0\left(\tau_0, \tau_1\right) + \epsilon^2 A_1\left(\tau_0, \tau_1\right) \\ Y(t) = Y\left(\tau_0, \tau_1\right) = B_0\left(\tau_0, \tau_1\right) + \epsilon^2 B_1\left(\tau_0, \tau_1\right) \end{cases} . \tag{2.40}$$

Substituting into Eq. (2.36) and collecting terms of same order in ϵ, the zeroth and second order equations are given below

$$\begin{cases} \partial_0^2 A_0 + A_0 = 0 \\ \partial_0^2 B_0 + B_0 = 0 \end{cases} \tag{2.41}$$

and

$$\begin{cases} \partial_0^2 A_1 + A_1 = & -2\partial_0\partial_1 A_0 + \beta_1\left(A_0^3 + A_0 B_0^2\right) \\ & +\beta_2\left[A_0\left(\partial_0 A_0\right)^2 + A_0^2\left(\partial_0^2 A_0\right) + A_0\left(\partial_0 B_0\right)^2 + A_0 B_0\left(\partial_0^2 B_0\right)\right] \\ & +2\left(\frac{\hat{\omega}}{\hat{\omega}_n}\right)^2 f\cos\left(\frac{\hat{\omega}}{\hat{\omega}_n} t\right) \\ \\ \partial_0^2 B_1 + B_1 = & -2\partial_0\partial_1 B_0 + \beta_1\left(A_0^2 B_0 + B_0^3\right) \\ & +\beta_2\left[B_0\left(\partial_0 A_0\right)^2 + A_0 B_0\left(\partial_0^2 A_0\right) + B_0\left(\partial_0 B_0\right)^2 + B_0^2\left(\partial_0^2 B_0\right)\right] \end{cases} \tag{2.42}$$

where ∂_0 and ∂_1 represent the partial derivative with respect to τ_0 and τ_1, respectively. The solutions to the zeroth order equations (2.41) are

$$\begin{cases} A_0\left(\tau_0, \tau_1\right) = A\left(\tau_1\right) e^{i\tau_0} + \bar{A}\left(\tau_1\right) e^{-i\tau_0} \\ B_0\left(\tau_0, \tau_1\right) = B\left(\tau_1\right) e^{i\tau_0} + \bar{B}\left(\tau_1\right) e^{-i\tau_0} \end{cases} \tag{2.43}$$

where $A\left(\tau_1\right)$ and $B\left(\tau_1\right)$ are complex, and the bar represents their complex conjugates. For convenience, the complex quantities $A\left(\tau_1\right)$ and $B\left(\tau_1\right)$ are represented in polar form

$$\begin{cases} A\left(\tau_1\right) = a\left(\tau_1\right) e^{i\theta\left(\tau_1\right)} \\ B\left(\tau_1\right) = b\left(\tau_1\right) e^{i\phi\left(\tau_1\right)} \end{cases} \tag{2.44}$$

where a, b, θ and ϕ are real. Then introducing the zeroth order solutions into the right hand side of the second order equations (2.42) and further requiring that the coefficients of the secular terms vanish, we get the following evolution equations for a, b, θ and ϕ

$$\begin{cases} \frac{da}{d\tau_1} = \frac{1}{2}\left[\left(\beta_1 - 2\beta_2\right) ab^2 \sin 2(\phi - \theta) + (1+\sigma)^2 f \sin(\sigma\tau_1 - \theta)\right] \\ \\ \frac{d\theta}{d\tau_1} = \frac{1}{2}\left[\left(3\beta_1 - 2\beta_2\right) a^2 + \left(\beta_1 - 2\beta_2\right) b^2 \cos 2(\phi - \theta) + 2\beta_1 b^2 + (1+\sigma)^2 \frac{f}{a} \cos(\sigma\tau_1 - \theta)\right] \\ \\ \frac{db}{d\tau_1} = \frac{1}{2}\left[\left(\beta_1 - 2\beta_2\right) a^2 b \sin 2(\phi - \theta)\right] \\ \\ b\frac{d\phi}{d\tau_1} = -\frac{1}{2} b\left[\left(3\beta_1 - 2\beta_2\right) b^2 + \left(\beta_1 - 2\beta_2\right) a^2 \cos 2(\phi - \theta) + 2\beta_1 a^2\right] \end{cases} . \tag{2.45}$$

In the above equations, $\sigma = \hat{\omega}/\hat{\omega}_n - 1$ is usually referred to as *detuning* and is a small deviation from the n^{th} eigenfrequency ω_n; note that we have set $\epsilon = 1$ at this stage. For further simplicity, let $\gamma = 2(\phi - \theta)$, $\nu = \sigma\tau_1 - \theta$. Then, equation (2.45) becomes

$$\begin{cases} \frac{da}{d\tau_1} = \frac{1}{2}\left(\beta_1 - 2\beta_2\right) ab^2 \sin\gamma + \frac{1}{2}(1+\sigma)^2 f \sin\nu \\ \\ \frac{d\nu}{d\tau_1} = \sigma + \frac{1}{2}\left(3\beta_1 - 2\beta_2\right) a^2 + \frac{1}{2}\left(\beta_1 - 2\beta_2\right) b^2 \cos\gamma + \beta_1 b^2 + (1+\sigma)^2 \frac{f}{2a} \cos\nu \\ \\ \frac{db}{d\tau_1} = -\frac{1}{2}\left(\beta_1 - 2\beta_2\right) a^2 b \sin\gamma \\ \\ b\left[\frac{d\gamma}{d\tau_1} = \left(\beta_1 - 2\beta_2\right)\left(1 - \cos\gamma\right)\left(a^2 - b^2\right) + \left(1+\sigma\right)^2 \frac{f}{a} \cos\nu\right] \end{cases} . \tag{2.46}$$

There are two possible steady-state solutions for Eq. (2.46), i.e. planar and 3D motions. In both cases, all the quantities are time-independent. First, for 2D steady-state motion, we have $b = 0$, then, equation (2.46) can be reduced to

$$\left(-1\right)^k f\sigma^2 + 2\left(a + \left(-1\right)^k f\right)\sigma + \left(-1\right)^k f + \left(3\beta_1 - 2\beta_2\right) a^3 = 0, \tag{2.47}$$

where k is an integer. Equation (2.47) can be solved for σ for a prescribed a. For the 3D steady-state motion, equation (2.46) can be simplified as

$$\begin{cases} \sigma^2 + 2\left(1 + \frac{1}{\Delta}\right)\sigma + \left(1 + \frac{4\beta_1 a^2}{\Delta}\right) = 0 \\ \\ b^2 = a^2 + \frac{(-1)^k (1+\sigma)^2 f}{2(\beta_1 - 2\beta_2) a} \end{cases} \tag{2.48}$$

where

$$\Delta = \left[(-1)^k \left(3\beta_1 - 2\beta_2\right) f\right] / \left[2\left(\beta_1 - 2\beta_2\right) a\right]. \tag{2.49}$$

Equation (2.48) can be solved for σ and b for given a.

For the planar and 3D steady-state motions to be stable, the eigenvalues of the Jacobian matrix of Eq. (2.46) must all be negative or pure imaginary, i.e. the small perturbation from the equilibrium state must be bounded. For the 2D steady-state motions to be stable, this results in the following inequalities

$$\begin{cases} (-1)^k \left(3\beta_1 - 2\beta_2\right) a_0 - (1+\sigma)^2 \frac{f}{2a_0^2} \le 0 \\ \\ \left(\beta_1 - 2\beta_2\right)^2 a_0^4 - \left[(-1)^k (1+\sigma)^2 \frac{f}{a_0} + \left(\beta_1 - 2\beta_2\right) a_0^2\right]^2 \le 0 \end{cases} . \tag{2.50}$$

Similarly, for 3D motion, we have

$$\begin{cases} 4a_0^2 \left[2\left(\beta_1 - 2\beta_2\right)^2 a_0^3 - \beta_2 (1+\sigma)^2 f \cos\nu_0\right]^2 + \left(\beta_1 - 2\beta_2\right)(1+\sigma)^2 f a_0^2 \\ \left[(-1)^k 16\beta_1 \left(\beta_1 - 2\beta_2\right) a_0^3 + \left(5\beta_1 + 2\beta_2\right)(1+\sigma)^2 f - (-1)^k \frac{(3\beta_1 - 2\beta_2)(1+\sigma)^4 f^2}{2(\beta_1 - 2\beta_2)} a_0^{-3}\right] \ge 0 \\ \\ 2\left(\beta_1 - 2\beta_2\right)^2 a_0^3 - (-1)^k \beta_2 (1+\sigma)^2 f \ge 0 \\ \\ (-1)^k 16\beta_1 \left(\beta_1 - 2\beta_2\right) a_0^3 + \left(5\beta_1 + 2\beta_2\right)(1+\sigma)^2 f - (-1)^k \frac{(3\beta_1 - 2\beta_2)(1+\sigma)^4 f^2}{2(\beta_1 - 2\beta_2)} a_0^{-3} \le 0 \end{cases} \tag{2.51}$$

where the subscript zero represents quantities corresponding to the steady-state solutions.

The solutions of the 2D and 3D steady-state motions corresponding to Eqs. (2.47) and (2.48) are shown in Figures 2.6a and 2.6b, respectively, for modes

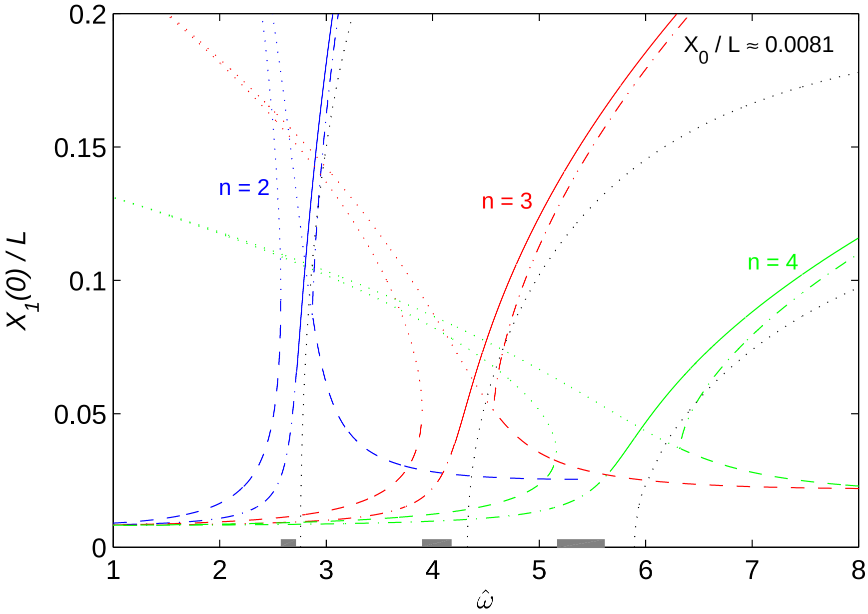

(a) in-plane

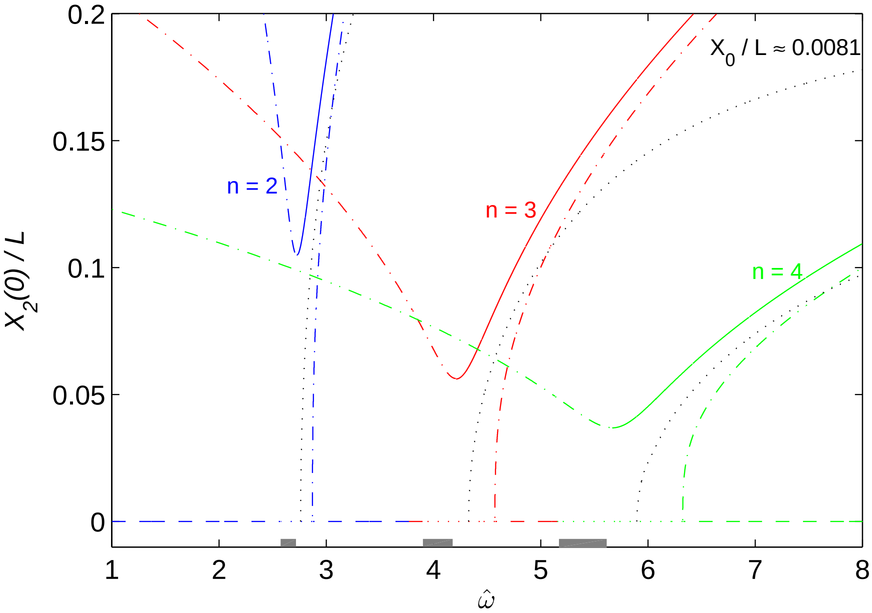

(b) out-of-plane

Figure 2.6: Frequency response of the string under planar excitation. The color lines are predictions of the perturbation analysis (solid line: stable 3D; dash-dot lines: unstable 3D; dashed lines: stable 2D; dotted lines: unstable 2D). The solutions of free response are also superposed in this figure as black dotted lines. ($L = 0.40m$).

$n = 2, 3, 4$. The results of the stability analysis are also indicated in these figures. The different lines (blue, red, and green in the electronic version) correspond to modes $n = 2, 3, 4$, respectively. While multiple branches are seen, for clarity, we identify the dashed lines as stable 2D and solid lines as stable 3D motion. For $n = 2$, as the driving frequency increases, the response first follows the branch of stable steady-state planar motion with a small amplitude (identified by the dashed line). When $\hat{\omega} \approx 2.58$, the planar motion becomes unstable and the 2D branch beyond this is indicated by the dotted line; 3D motion is also still unstable and is indicated by the dash-dot line; this was noted by Triantafyllou and Howell [86] as well. As the frequency reaches $\hat{\omega} \approx 2.72$, stable 3D solution (solid line) becomes available such that the response will follow this stable 3D branch until $\hat{\omega} \approx 2.87$; beyond this stable planar solutions (dashed line) with lower energy appear again. This shows that even though the excitation is restricted to be planar, the forced response can be either planar or 3D due to the dynamical instability, which depends on the excitation frequency. As the driving frequency approaches the resonant frequency range, the planar response becomes unstable and the resulting motion becomes 3D. After the frequency passes through the resonant frequency range, the motion changes back to 2D motion again. These phenomena repeat for other modes $n = 3, 4$ etc and are indicated also in Fig. 2.6. The range over which neither 2D nor 3D motion is stable is indicated by the gray bar placed along the abscissa in Fig. 2.6 near each mode; it is apparent that this range increases with increasing mode number.

So far, we have established the theoretical analysis for the motion of a flexible string subjected to either planar or rotary excitation at one end and free at the other under self-weight. In the following sections, we will perform the corresponding experiments and compare the experimental results with the theoretical analysis.

2.3 Experimental Setup

There are three main ingredients in bringing to realization the motions of string subjected to planar or rotary excitation. The first ingredient is the identification of a string with appropriate mechanical condition that can transmit the motion imposed at one end to the rest of the string but can rightly be considered as an inextensible and flexible string. The second is the ability to generate the high-degree planar sinusoidal or pure whirling excitation in the string. This requires a speed controlled motor with a high degree of control in order to eliminate any spurious driving forces in other directions. The third is the ability to obtain quantitative measurements of the amplitude of the motion. We describe the details of the experimental arrangement in this section.

2.3.1 Flexible String

It is unfortunate that the terminology “heavy chain” was used in the early literature. It might seem that a chain would be ideal in the sense that it can exhibit the required torsional stiffness in order to transmit the applied torque but at the same time exhibit almost negligible bending stiffness. However, a chain (or even a twined or braided thread or string) introduces hysteretic behavior in the torque-twist response that is not quite suitable for this particular demonstration. Western [90] was able to demonstrate some elements of this problem with a necklace chain only because he was in the region of small amplitude whirling as will become clear from our experimental results. Furthermore, the string does not have to be "heavy"; the mass density of the string must be nonzero in order to provide the gravitational and inertial forces assumed in the model; other than that, it plays no role whatsoever in determining the motion of the string. In our quest for the ideal "string", we examined tightly braided cotton and nylon threads, twines, nylon fishing line, cosmetic jewelry chains, piano wire, rubber cord extracted from elastic waist bands etc. Material and structural properties are shown in Table 2.1 for steel, nylon and rubber. The natural frequencies of the linearized whirling modes are also indicated in this table. For these thin strings, the bending stiffness is very small. Comparison of the bending energy to the stretching energy requires a length scale. If we take the length scale to be about $L/10$, such that there are 10 bends over the length of the string, then we can estimate that the ratio of bending energy to stretching energy is roughly 10^{-4}. Thus, for a first approximation it appears that we may ignore bending contributions for any of the materials considered. The experiments reported here were performed with a rubber string with properties shown in Table 2.1.

2.3.2 Planar Excitation and Whirling Apparatuses

In the realization of planar harmonic excitation, the upper end of the string was attached to a *Ling Dynamic System (LDS) Model 203 shaker* and driven by a *LDS* power oscillator with the frequencies in the range of 0 to 25 kHz, and the shaking amplitude X_0 is adjustable by changing the amplitude of the output voltage. In our experiments, the shaking amplitude X_0 was set to be 3.25 mm. The entire assembly was placed in an enclosure in order to eliminate disturbances from air currents in the room; the enclosure was fitted with a transparent view port on one side to enable observations. During the experiments, the exact driving

Table 2.1: Material and structural properties of steel, nylon and rubber.

Material	Unit	***Steel***	***Nylon***	***Rubber***
Density, ρ	kg/m^3	7800	1100	1130
Modulus of elasticity, E	GPa	200	2.8	0.0036
Cross-sectional Diameter, d	m	0.00060	0.00060	0.00060
Length, L	m	0.40	0.40	0.40
Bending rigidity, EI	Nm^2	1.27×10^{-3}	1.78×10^{-5}	2.29×10^{-8}
Axial stiffness, EA	N	5.65×10^{4}	7.92×10^{2}	1.02
Axial wave speed, $c = \sqrt{E/\rho}$	m/s	5064	1595	56

(Whirling resonance [rad/s]: $5.95, 13.66, 21.42, 29.18, 36.95$)

frequencies were measured with a digital oscilloscope.

In order to provide the proper boundary conditions for the whirling string, a 12 V DC motor (Pittman Express Model 8322S001) with an encoder and a speed controller (JR Kerr Automation Engineering PIC-SERVO board) were used. This motor provides a continuous torque of $0.011N \cdot m$ at speeds below $800rad/s$. The encoder provides 500 counts per revolution in order to enable the speed controller to maintain a constant speed. The encoder on the motor and the controller together are capable of maintaining the speed error to within 15 parts per million. The motor was mounted on a stiff frame on top of a vibration isolated optical table. A precision-machined sleeve was press fit on the shaft of the motor to ensure proper balance of the rotating mass. The string was inserted into one end of the sleeve through a small hole and fixed in place through two set-screws. The other end of the string was left freely hanging thereby replicating the boundary conditions assumed in the problem formulation. This arrangement provided good alignment of the loading; the string was provided with a rotational motion along its axis with the magnitude of the lateral motions below the sensitivity of our measuring instruments. The entire assembly was placed in an enclosure in order to eliminate influences from air currents in the room; it was fitted with a view port on one side to enable observations.

2.3.3 Quantitative Imaging

Quantitative measurement was obtained using video imaging systems. Three different schemes were used in these experiments. In the first arrangement, in order to obtain the mode shapes, a video camera was used in conjunction with a Frame Grabber board in a *time-averaging* mode. A *LabVIEW* program was written to acquire images with controllable exposure times, under continuous illumination. The camera was aimed so as to obtain a projection in the (X_1, X_3) plane. Considering that the first five natural frequencies of whirling corresponding to the linearized problem are below $6.3Hz$, exposure over $0.25s$ assures us of capturing many revolutions of the string; thus, this long time exposure should indicate the mode shape in the (X, Z) coordinate system. In the second arrangement, the string was observed through a mirror mounted at 45^o to the X_3 axis to obtain a projection of the tip point of the string in the (X_1, X_2) plane. Multi-flash images of the tip were obtained in many sequences at different frequencies of whirling and used to identify the trajectory of the tip point.

In the third arrangement, computer stereo vision techniques, as shown in Fig. 2.7, well-developed in the field of artificial intelligence [10, 83] were adapted

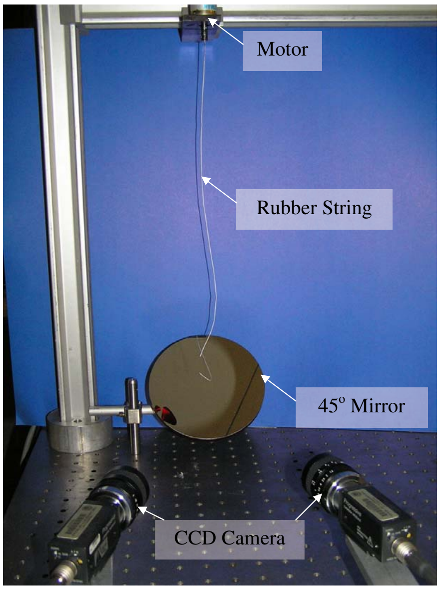

(a) Experimental apparatus

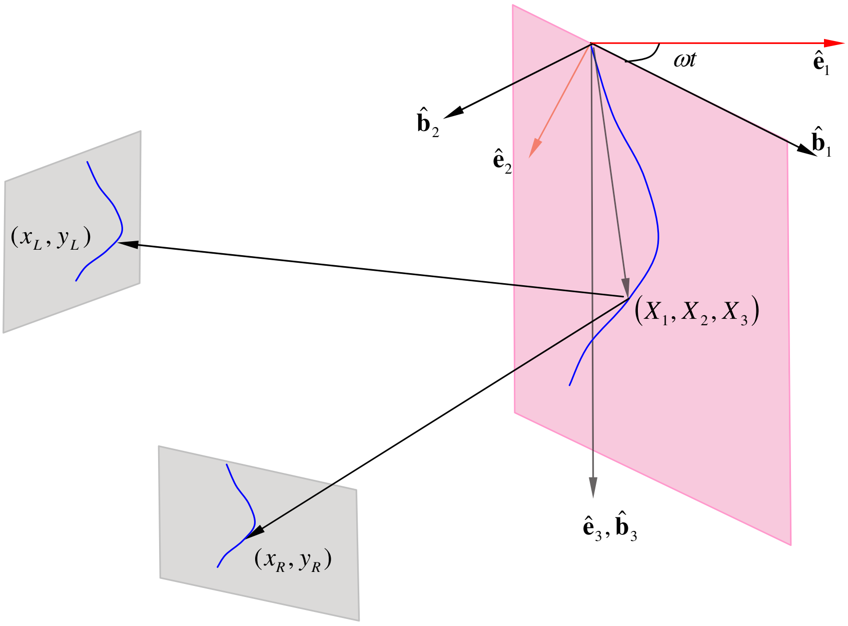

(b) Schematic of 3D Stereo vision system

Figure 2.7: Experimental setup and stereo vision system.

for measurement of $\mathbf{r}(s,t)$ in a time-resolved mode. Such a method has recently been used by Helm *et al.*, [48] to measure the three-dimensional shape and displacements of deformable objects. The principle of this method is quite simple: consider an object point (X_1, X_2, X_3) in three dimensional space. This point is viewed through two cameras and the corresponding points in the left and right image planes are identified by a digital image correlation algorithm; thus, we get the following projections of the object point: (x_L, y_L) and (x_R, y_R) in the coordinate system of the two cameras. (x_L, y_L) and (x_R, y_R) can be used to reconstruct the object point (X_1, X_2, X_3) based on a model for the camera. Calibration of the system for intrinsic parameters of the camera such as focal lengths, principal point, and correction for lens distortion errors and extrinsic parameters of the geometry of the optical arrangement of the two cameras relative to the object (rotation angles and translation vector of two three-dimensional coordinate systems) needs to be performed. This calibration is accomplished by obtaining photographs of a precise checkerboard pattern in multiple orientations and identifying the corner points of the pattern through a nonlinear least square technique to minimize the following error function to get the optimum parameters:

$$Error(parameters) = \sum_{exp-points} [(x_c - x_{c-exp})^2 + (y_c - y_{c-exp})^2]^{1/2} \tag{2.52}$$

where (x_c, y_c) are the camera coordinates from the coordinates (X_1, X_2, X_3) of each corner of the checkerboard pattern determined by using geometric projection. (x_{c-exp}, y_{c-exp}) are measured from the captured images of the corner of the checkerboard pattern. Details of these procedures can be found in Tsai [87]. Here, we used the calibration toolbox based on Matlab developed by Bouguet [9]. With our optical system, we were able to obtain a position accuracy of less than one mm in all three directions.

In our experiments, two Sony XC-55 monochrome progressive scan cameras, two National Instruments' IMAQ 1409 frame grabbing boards and the image acquisition software based on LabVIEW 7.0 were used to acquire the motion trajectories of the string simultaneously. The progressive scan cameras allow a scan reset that when combined with the IMAQ 1409 controller function enables the acquisition of images from both cameras at the same time. A flash illumination was synchronized with the image capture in order to freeze the motion of the string in the image. It was also possible to acquire the image with a long time exposure, but with the string illuminated by a stroboscope such that multiple images of the string were obtained in the same frame. Then a three-dimensional algorithm was used to reconstruct the three-dimensional shape and trajectories of the rotating string.

2.4 Whirling Response of a Rubber String

We now describe the experimental observations for the whirling string. A rubber string (length $L = 0.40m$, diameter $d = 0.60mm$, density $\rho = 1130kg/m^3$, and modulus of elasticity under small stretch $E = 3.6MPa$) was attached to the supporting fixture at the base of the motor as described in Section 2.3.2. The motor was set in steady-state rotation at progressively increasing frequencies. At each frequency the transients were allowed to dissipate and then the whirling mode shape was captured through the time-averaging video imaging as described in Section 2.3.3. In contrast to the solutions to the nonlinear problem as discussed in Section 2.1.4, it was possible to generate steady-state whirling motion only at specific frequencies, while non-steady motion was observed at other frequencies. The steady-state behavior is evaluated first; this is followed by an evaluation of the non-steady response of the string to periodic excitation. Although only results corresponding to the rubber string are presented here, these observations remain valid regardless of the composition of the string.

2.4.1 Steady-State Response

In order to eliminate possible hysteretic effects of dependence on initial conditions, at each frequency, the whirling motion was diminished by moving two fingers on either side of the string and then allowed to rebuild naturally. In contrast to the solution discussed above, steady-motion of the type assumed in Eq. (2.7) was observed only at specific frequencies. In Fig. 2.8a, the experimentally obtained mode shapes corresponding to steady-state are compared to the Bessel function mode shapes in Eq. (2.18) corresponding to the linearized eigenvalue problem. The mode $n = 1$ exhibited a very small amplitude and hence resonance could not be observed easily and are not shown here. As can be seen from the experimental observations, for the lowest mode shown ($n = 2$), the experimentally observed mode shape is close to the Bessel function. But for higher modes ($n = 3-5$), the deviation from the linearized theory is apparent. Clearly, we must resort to the nonlinear analysis. Western [90] showed experimentally mode shapes from a necklace chain; from his measurements he obtained the positions of the nodes and showed that they were in good agreement with the nodes identified by the linearized solution. As can be seen from Fig. 2.8a, even though the nodes are almost at the same locations as the Bessel function indicates, the disagreement in the amplitude is quite substantial.

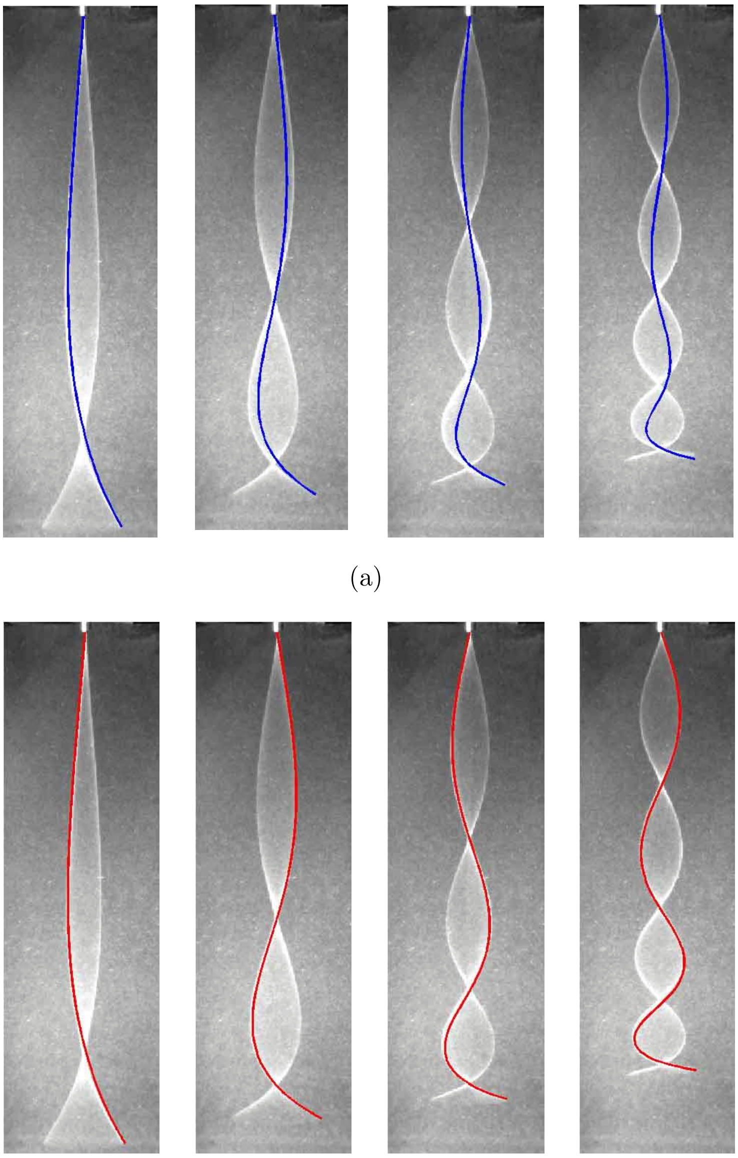

(a)

(b)

Figure 2.8: Time-averaged images of the rubber string corresponding to four steady-state modes are compared with the predictions of the linearized theory (a) and the nonlinear theory (b).

The nonlinear problem was solved for the parameters of the rubber string in MATLAB as indicated in Section 2.1.4. As described there, Eqs. (2.11) and (2.12) possess multiple solutions at any frequency. So, two options are available: either find the whirling mode shape appropriate to the experimentally imposed frequency of rotation or find the appropriate frequency corresponding to a matched mode shape. The first option was discarded since the amplitude determined from Eqs. (2.11) and (2.12) at the imposed frequency did not match the experimentally observed amplitudes. On the other hand, searching for an appropriate frequency at which the amplitude of the whirling matched the observed shapes resulted in good agreement as shown by the red lines in Fig. 2.8b. The frequencies at which the nonlinear solution matched the measured resonance frequencies are given in Table 2.2; these differ from the experimentally measured resonance frequencies by an increasing amount with increasing mode number. The influence of bending stiffness in the rubber string appears to be the primary reason for this discrepancy; this will be explored further in Chapter 3.

Table 2.2: Comparison of resonance frequencies. ($\omega_n : rad/s$)

Mode n	Linearized eigenvalue	Nonlinear frequency	Experiment	% difference between nonlinear theory and experiments
2	13.67	13.94	14.47	3.80
3	21.43	23.60	24.91	5.55
4	29.20	34.20	36.89	7.87
5	36.97	47.50	52.22	9.94

2.4.2 Non-Steady Motion

We now turn to an examination of the non-steady motion of the whirling string. At any frequency between those where steady response was observed, the string exhibited whirling motion with a dominant mode shape very similar to that obtained at the steady-states discussed above, but an additional motion in both the radial and axial directions appeared superposed. Selected time-averaged images of the motion are shown in Fig. 2.9. We note that the images were taken with a constant exposure time and hence at the higher rotational speeds, more revolutions of the string were captured. From the images in this figure, it is clear that two features of the steady-state solution are violated. First, the nodal points move with time and second, the vertical position of the string is not time independent as assumed in formulating the steady-state solution. The motion still appears to be repeatable, but with two different periods: the first period is associated with the rotational motion input through the motor and dominated by the mode shapes found earlier. The second periodic motion is associated with variations in the axial motion.

In an effort to quantify the non-steady motion of the string, the video imaging system was reoriented to the second arrangement discussed in Section 2.3.3. The entire string was painted with black ink, leaving only the free-end tip point visible in the video imaging system. Images of the tip at different frequencies of whirling were then obtained in this arrangement. During each exposure of the camera, the light was pulsed N times (typically 10 times) resulting in N distinct images of the tip point. These images were then filtered to eliminate all other points, leaving only the N images of the tip of the string. This imaging scheme was repeated M times (typically 250 images) and all M images were

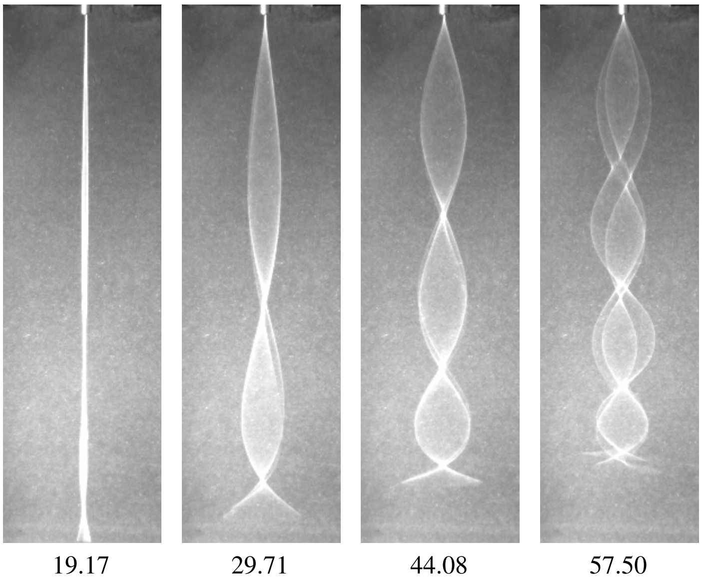

Figure 2.9: Time-averaged images of the rubber string corresponding to frequencies in between the different steady modes.

then superposed to obtain a map of the tip in the (X_1, X_2) plane; thus, each composite image contains $M \times N$ discrete images of the free-end tip point of the string. Such images, captured under increasing frequencies spanning from $n = 2$ to $n = 5$ are shown in Fig. 2.10. A number of observations can be made from these measurements.

- Corresponding to steady-state motion, the locus of the tip points projected in the (X_1, X_2) plane is nearly circular; the width of this circle is an indication of the extent of variation of $X(0)$. The small width over which the tip points are dispersed in the some cases indicates that $X(0)$ is indeed constant and the motion assumed in Eq. (2.7) is the one observed. The motion is periodic and the circular orbit is executed at the period of the imposed rotation.

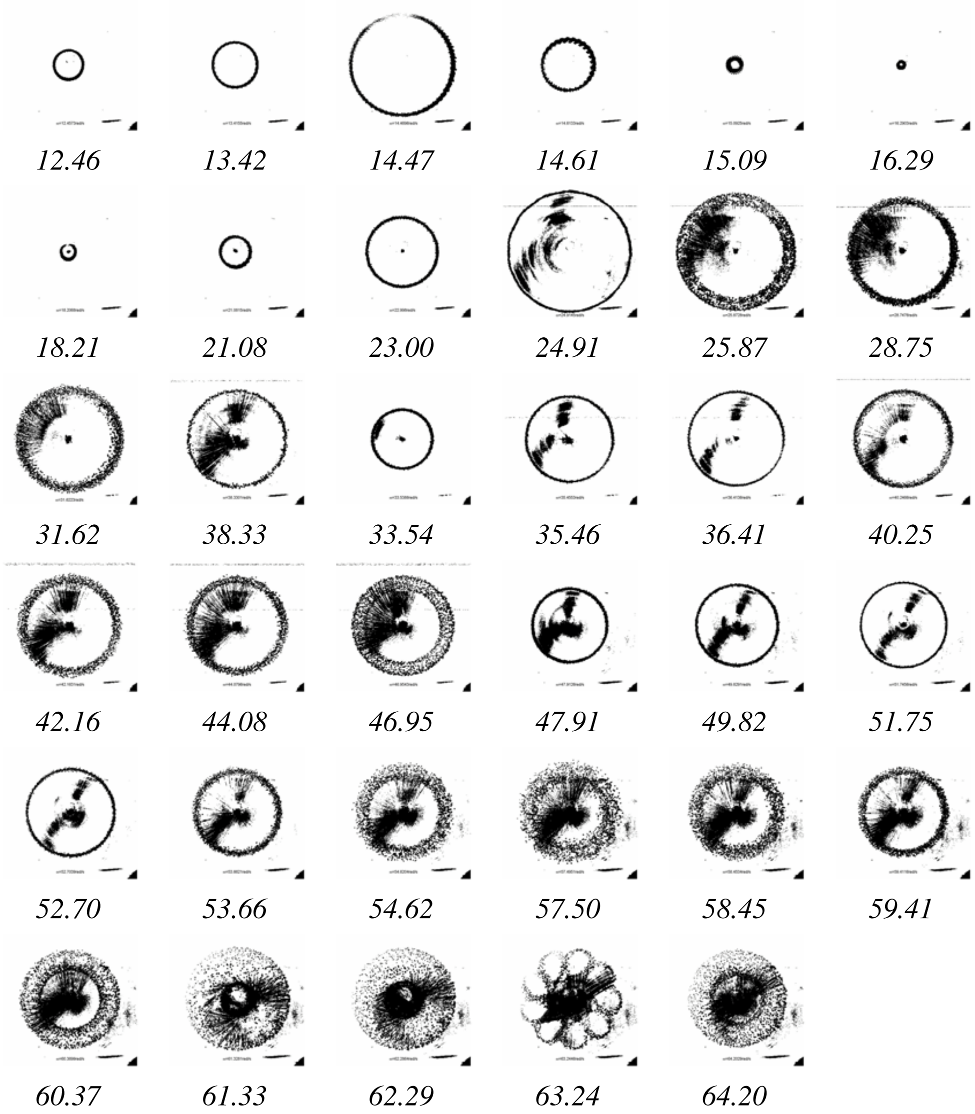

12.46 13.42 14.47 14.61 15.09 16.29

18.21 21.08 23.00 24.91 25.87 28.75

31.62 38.33 33.54 35.46 36.41 40.25

42.16 44.08 46.95 47.91 49.82 51.75

52.70 53.66 54.62 57.50 58.45 59.41

60.37 61.33 62.29 63.24 64.20

Figure 2.10: Locus of motion of the tip point of the string. The dark points in the interior of the annulus are obtained from other points along the length of the string that could not be eliminated in the optical arrangement. (ω : rad/s and $L = 0.40m$).

- In other cases, the locus of the tip points projected in the (X_1, X_2) plane lies within a circular annulus, but with the extent of this annulus varying significantly with frequency. Thus $X_1(s,t) = X\cos(\omega t)$ is no longer an appropriate description of the motion. Note also that $X_3(s,t) = Z(s)$ is not adequate since time dependence in the axial motion is essential. However, this information is lost in the projection obtained; quantitative stereo-imaging can be used to reveal the nature of this motion as we examine in the next section.

- As the whirling speed is increased form one natural frequency towards another, spectacular patterns are formed by the tip point; this is most evident in the next to the last image in Fig. 2.10, but if fewer revolutions of the string are captured in the imaging process, patterns become evident at other whirling frequencies as well; this is illustrated through the observations in Fig. 2.11. Such patterns are a clear indication of multiple periodicities in the phenomena observed. In particular, Woolley [93] observed patterns in the motion of the flagella of eel sperm that are identical to that shown in Fig. 2.11a and called these *flagelloid* curves; while there is a geometric similarity in the patterns, the underlying physical connections need to be developed more carefully.

From the images shown in Fig. 2.10, the amplitude excursion of $X_1(s,t)$ clearly depends nonmonotonically on the frequency of rotation; this is developed further through a plot of the amplitude of the tip $X_1(0,t)$, determined as a function of the frequency of rotation in Fig. 2.12. In this figure, the frequency of the imposed rotation is normalized by the characteristic frequency $\sqrt{g/L}$. The dotted lines indicate the steady-state solution to the nonlinear eigenvalue prob-

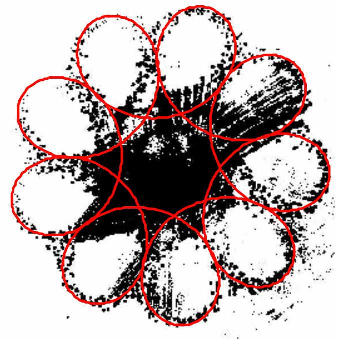

ω =63.24 *rad/s*

L = 0.4 *m*

ω = 40.28 *rad/s*

L= 0.2 *m*

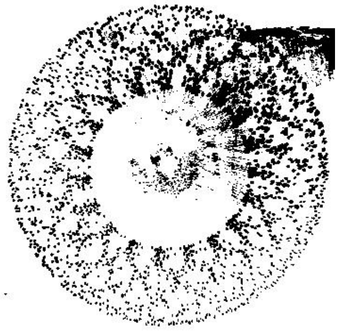

ω = 49.83 *rad/s*

L = 0.2 *m*

Figure 2.11: Patterns formed by the tip point at different rotational frequencies. Solid line in the first image is drawn with $\omega_m/\omega = 8$ (see Eq. (2.54)).

lem corresponding to different modes. The vertical solid lines (Red and blue) indicates measured amplitude excursion at different frequencies as the frequency is increased from the second eigenfrequency; these are lines connecting measurements of the maximum and minimum amplitudes determined from the projection of $X_1(0,t)$ in the (X_1, X_2) plane. The red lines are the corresponding measurements obtained as the frequency is continuously increased while the blue lines are related to measurements obtained as the frequency is graduately decreased. These measurements reveal the complex nonlinear response of the string to the whirling motion. The main observations are listed below:

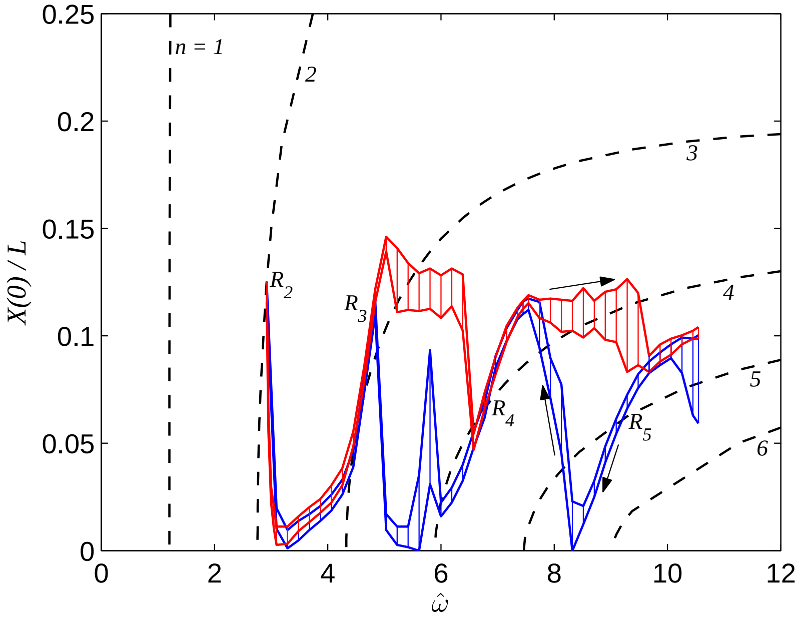

Figure 2.12: Variation of the amplitude of the free-end tip point as a function of the driving frequency.

- The points R_2 through R_5 marked on Fig. 2.12 correspond to observed steady-state behavior shown in Fig. 2.8. These appear to lie close to the steady-state solution to the nonlinear problem.

- Beginning at the second mode at R_2, if the driving frequency is increased, rather than follow the solution corresponding to the mode $n = 2$, the string whirls at a mode that is close to this shape; the amplitude of whirling appears to correspond well with the approximate solution of the forced whirling problem.

- As the driving frequency is increased close to the range where the third mode solution to the nonlinear problem is available, the amplitude increases quickly until steady motion is observed at R_3. At each frequency below R_3, there is still a periodic fluctuation of the amplitude between the vertical lines indicated in Fig. 2.12, although the magnitude of the fluctuation is small.

- Upon decrease of the frequency from R_3 to R_2, the frequency response follows the same branch and jumps back to the 2^{nd} mode resonance at R_2.

- As the driving frequency is increased above R_3, the string is unable to follow the nonlinear solution corresponding to the branch $n = 3$. This is similar to the observation at the 2^{nd} resonance; however, rather than the low amplitude whirling that was observed immediately beyond R_2, now the string maintains the mode shape of $n = 3$ with a substantial amplitude together with a superposed time-dependent variation. The amplitude decreases for a while, but is then followed by a gradual increase with the process repeating itself periodically, with a period much larger than the whirling period; such amplitude excursions are marked in Fig. 2.12 by the vertical lines and their envelope. We refer to this mode as the *trapped mode*; detailed evaluation of the trapped mode are provided in the next section.

- When the frequency is increased to the range where the next mode shape and steady-state nonlinear solution become available, an abrupt transition occurs as the $n = 4$ mode shape is taken with a smaller amplitude. Decreasing the frequency from this range towards R_3 results in the string maintaining the $n = 4$ mode, but with significantly lower amplitudes; attempted jumps and a successful jump back to the $n = 3$ mode are also seen clearly in Fig. 2.12. This hysteretic behavior is similar to the response of nonlinear systems such as the Duffing spring and the forced response indicated in Section 2.1.5.

- Increasing the driving frequency beyond R_4 a similar hysteretic behavior is observed once more. We anticipate that this nonlinear behavior would persist at higher modes, although not all higher modes may be achievable with any given string. In this particular string, with a length of $0.40m$, modes $n > 6$ were not attainable even at frequency as large as $65 rad/s$.

- If transverse deflection of the string whirling in a trapped mode is diminished by slowly running a cupped palm along the length of the string, the trapped whirling motion is reestablished suggesting that it is indeed the stable motion for the string.

- Overall, a significant departure from the steady-state solution of the nonlinear equations is observed, at small whirling amplitudes; we believe that this is due to the small bending stiffness of the string (and hence important at higher modes); we will pursue this quantitatively in a future contribution.

- Considering the overall response shown in Fig. 2.12, it is clear that the peak amplitude of the whirling motion is limited at $0.1L$. The reason for this limit in the whirling amplitude is not clear and needs further investigation; however, it was determined through repeated measurements that the magnitude of the peak amplitude depends on the length of the sting.

- We conclude that while steady state whirling modes are available, the string would not attain such a mode, but be trapped in a mode between two such steady-state solutions.

We now turn to a discussion of the trapped mode of the whirling string.

2.4.3 Trapped States

In an effort to understand the dynamics of the trapped mode response of the string, the stereo-vision system described in Section 2.3.3 was used to obtain the time variation of the spatial position of the tip point. Multiple stereo pairs of images were obtained over many periods of rotation of the string and then processed to determine $X_1(0,t)$, $X_2(0,t)$, and $X_3(0,t)$. This was then repeated at different whirling frequencies spanning the range from just before the third eigenfrequency to just beyond the fourth eigenfrequency. The variation of $X_1(0,t)$, $X_2(0,t)$, and $X_3(0,t)$ is shown in Figures 2.13, 2.14 and 2.15 for three different whirling frequencies; in these figures, the discrete points are samples obtained from the stereo vision measurements. Fig. 2.13 corresponds to whirling motion at R_3, and provides a clear demonstration of the steady-state motion as well as outlines the sensitivity of the measuring scheme; at resonance, the string exhibits no measurable time dependence in the X_3 direction and the motion in the X_1 and X_2 directions is sinusoidal. We recognize that there are higher frequency components to the X_3 motion, but these have not been fully resolved by the measuring system. On the other hand, beyond R_3, when the string enters the trapped modes, the motion in the X_3 direction exhibits a clear sinusoidal motion as shown in Fig. 2.14; furthermore, the motion in the (X_1, X_2) plane is modulated with the same period (as dictated by the inextensibility condition); in this figure, the data points are samples obtained from the stereovision measurements while the solid line corresponds to a modulated sinusoidal motion:

$$\begin{cases} X_1(0,t) = X(0)(1+\epsilon\cos\omega_m t)\cos\omega t \\ X_2(0,t) = X(0)(1+\epsilon\cos\omega_m t)\sin\omega t \\ X_3(0,t) = Z(0)(1-\epsilon\cos\omega_m t) \end{cases} . \tag{2.53}$$

With a further increase in the frequency, the motion in the X_3 direction is

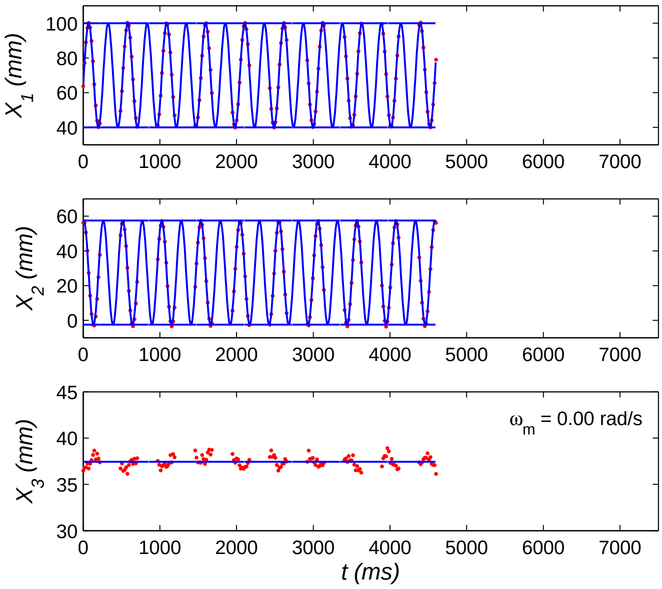

Figure 2.13: Time variation of the position of the tip at a driving frequency of $\omega = 24.91 rad/s$.

still periodic, but an increase in the modulation frequency as shown in Fig. 2.15 for $\omega = 33.54 rad/s$. The time dependence of the motion in the X_3 direction

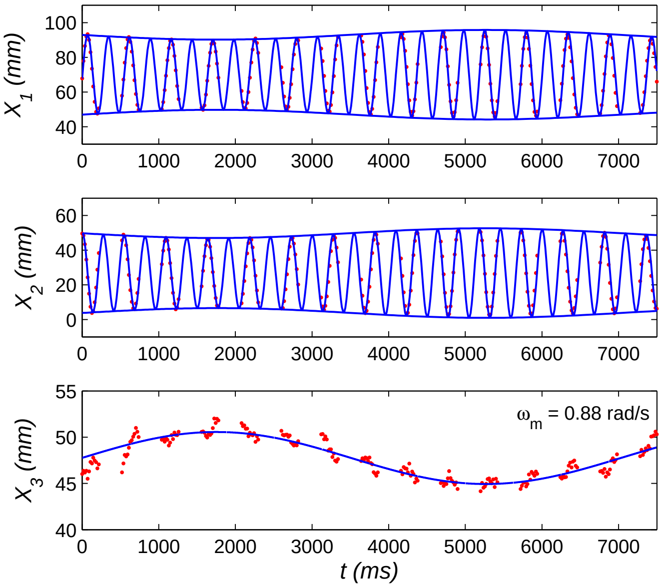

Figure 2.14: Time variation of the position of the tip at a driving frequency of $\omega = 26.83 rad/s$.

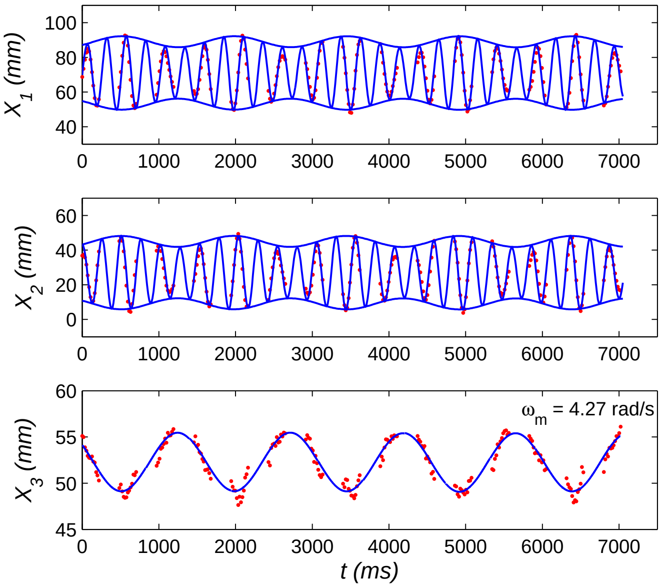

Figure 2.15: Time variation of the position of the tip at a driving frequency of $\omega = 33.54 rad/s$.

was traced at a number of frequencies from just below R_3 to just above R_4; this is shown in Fig. 2.16. At R_3, the string maintains a time independent position $X_3(0,t) = Z(0)$ to within the resolution of the measuring scheme $\pm 1mm$. With increasing frequency, a periodic motion is observed $X_3(0,t) = Z(0)f(t)$; this periodic oscillation is sinusoidal when the whirling frequency is close to a resonant frequency, but becomes increasingly distorted and asymmetrical as the whirling frequency is increased away from resonance. The emergence of a second time scale can be observed clearly from the results shown in Fig. 2.16; this time scale must relate to an interaction between the rotational motion and the axial wave motion that is neglected in the steady-state analysis based on Eq. (2.7).

The tip motion observed in the experiment suggests that the overall motion of the string could be assumed to be of the following form (in the fixed frame):

$$\begin{cases} X_1(s,t) = X_s(s)\cos\omega t + \epsilon X_m(s)f(t)\cos\omega_m t \\ X_2(s,t) = X_s(s)\cos\omega t + \epsilon Y_m(s)f(t)\sin\omega_m t \\ X_3(s,t) = Z_s(s)\cos\omega t - \epsilon Z_m(s)f(t) \\ T(s,t) = T_s(s)\cos\omega t + \epsilon T_m(s)f(t) \end{cases} \tag{2.54}$$

where the subscript s indicates the solution corresponding to the steady state and the subscript m indicates the modulation. An example of fitting the motion in Eq. (2.53) to the whirling of the string, is demonstrated in Fig. 2.11 with $\omega = 1$ and $\omega_m = 8$. The equations of motion for the modulation are similar to the original equations of motion in Eq. (2.5) and unless the modulation is assumed to be small - clearly not justified in light of the results shown in Fig. 2.16 - no reduction in the system of governing equations is obtained.

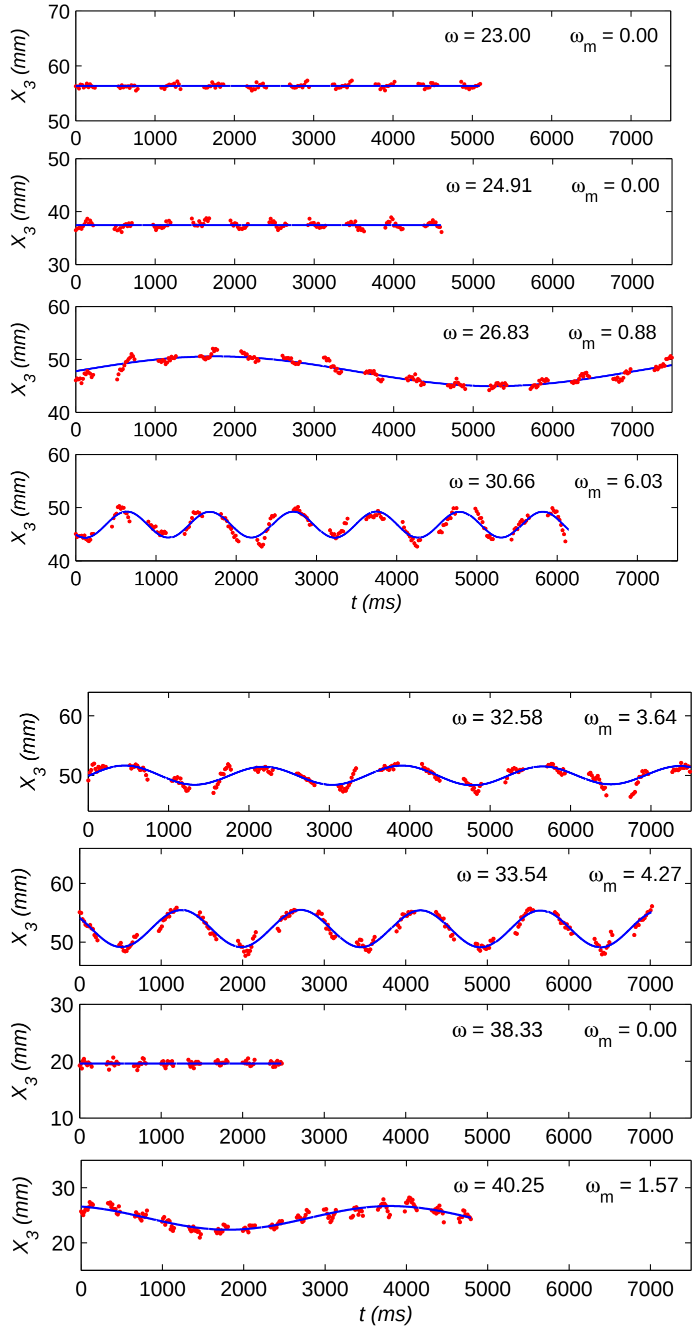

Figure 2.16: Time variation of the X_3-position of the tip at different driving frequencies.

2.5 Response of a Rubber String Subjected to Planar Excitation

2.5.1 Experimental Results

A rubber string was attached to the supporting fixture at the base of the shaker as described in Section 2.3.2; the shaker was set in steady-state oscillation at progressively increasing driving frequencies. Thus, the imposed motion is $X_1(L, t) = X_0 \cos(\omega t)$, in which X_0 is the forcing amplitude and ω is the driving frequency. At each frequency the transients were allowed to dissipate and then the mode shape was captured through the time-averaged video imaging scheme as described in Section 2.3.3. Time-averaged images displaying the mode shape at different driving frequencies are shown in Fig. 2.17. While it is not apparent from the time averaged images, it was observed that the two images in Fig. 2.17a corresponded to the string executing an oscillatory motion fully in the (X_1, X_3) plane for mode $n = 2$ and mode $n = 3$, while the images in Fig. 2.17b corresponded to the string executing a whirling (out-of-plane) motion in modes $n = 2$ and $n = 3$, even though the excitation was planar. The amplitude corresponding to whirling motion was always higher than the in-plane motion for the same mode. It was not possible to generate steady-state motion with either the planar or non-planar modes at all frequencies. As an example, Fig. 2.18 shows a temporal sequence of images of the motion shape at $\hat{\omega} = 4.62$ corresponding to the non-steady motion with multiple periodicities. In Fig. 2.18, each image is time-averaged image over successive $0.25sec$ time intervals. It is readily seen that as the driving frequency is increased, the string exhibits transitions from planar oscillations to out-of-plane whirling and then back to in-plane oscillations. Although only results corresponding to the rubber string are presented here, these observations remain valid regardless of the composition of the string.

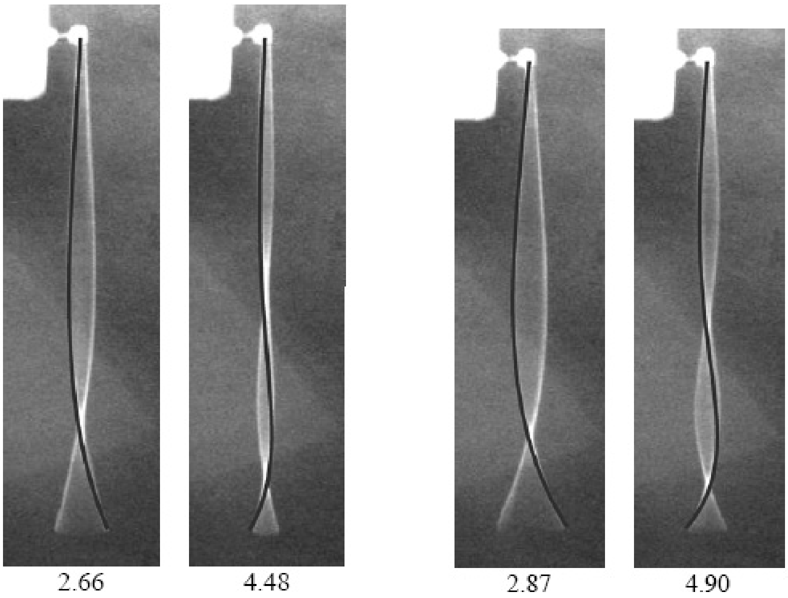

(a) steady-state 2D oscillations (b) steady-state 3D whirling

Figure 2.17: Time-averaged images of the motion shapes corresponding to four steady-state modes are compared with the predictions of the nonlinear theory. ($\hat{\omega}$: normalized driving frequency). ($L = 0.30m$)

In an effort to quantify the response of the string as the driving frequency is gradually increased, the second arrangement of the video imaging system was used. The entire string was again painted with black ink, leaving only the free-end tip point visible in the video imaging system. Images of the tip point at different driving frequencies were then obtained in this arrangement. During each exposure of the camera, the light was pulsed N times (typically 10 times) resulting in N distinct images of the tip point. These images were then filtered to eliminate all other points, leaving only the N images of the tip point of the string. This imaging scheme was repeated M times (typically 250 images) and all M images were then superposed to obtain a map of the tip point motion in the (X_1, X_2) plane;

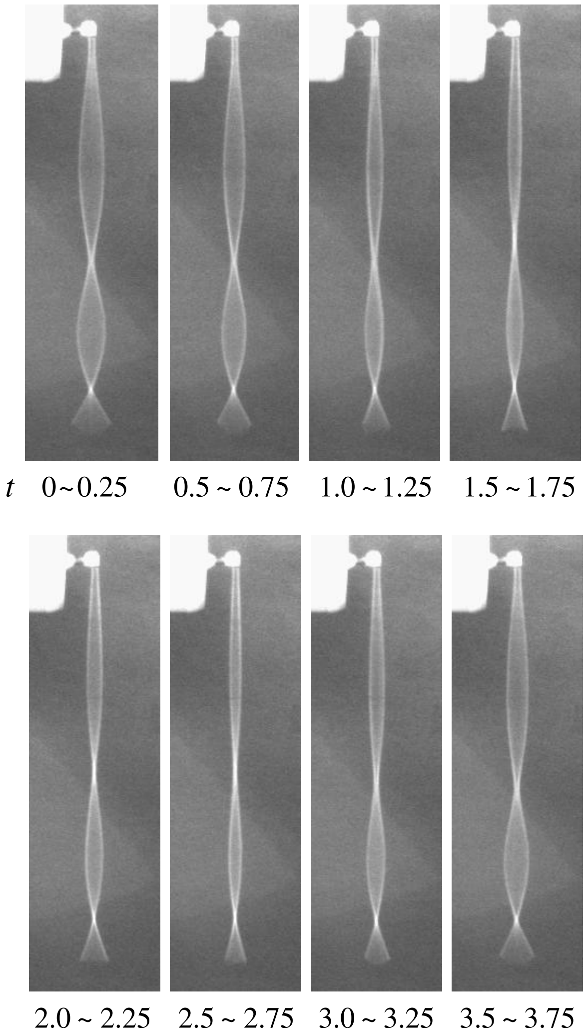

Figure 2.18: Temporal sequence of time-averaged images of the non steady-state motion shapes for normalized driving frequency: $\hat{\omega} = 4.62$. Time (t : sec). ($L = 0.30m$)

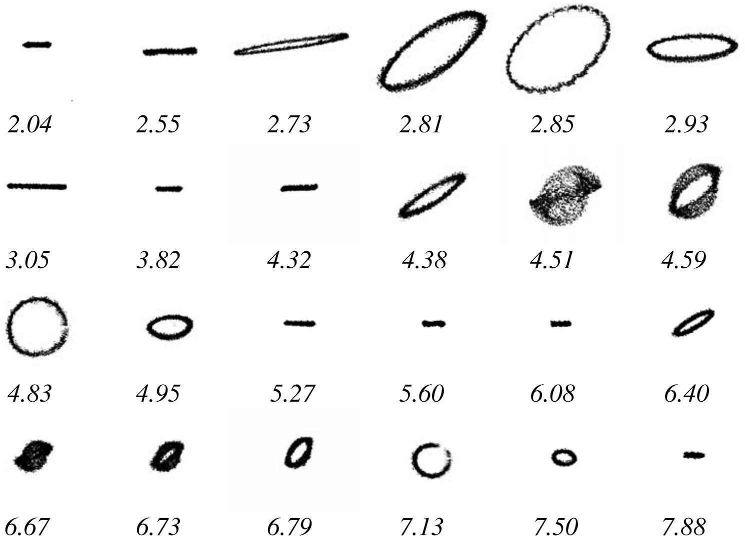

Figure 2.19: Locus of the motion trajectories of the free-end tip point for the rubber string subjected to planar excitation. ($\hat{\omega}$: normalized driving frequency and $L = 0.40m$).

thus, each composite image contains $M \times N$ discrete samples of tip point. The representative images, captured under gradually increasing frequencies spanning from $n = 2$ to $n = 4$, are shown in Fig. 2.19. A number of observations can be made from these measurements.

- For a certain range of driving frequency of imposed in-plane excitation, the locus of the free-end tip points projected in the (X_1, X_2) plane is a straight line. This represents the planar oscillatory response.
- As the driving frequency approaches the eigenfrequency of the linearized equations, out-of-plane whirling begins to emerge, initially with small amplitude but quickly increasing to larger amplitudes. The resulting loci on the (X_1, X_2) plane are elliptical and exhibit a phase relationship between the in-plane and out-of-plane components of the motion.
- Further increases in the driving frequency lead to a decrease and cut-off of the out-of-plane mode and the locus becomes a straight line again.
- At higher driving frequencies, the in-plane and out-of-plane amplitudes become nearly equal and the loci on the (X_1, X_2) plane are nearly circular. This corresponds to the 3D steady whirling response.
- Interesting patterns appear during the transition from planar oscillatory response to 3D whirling response, as seen in Fig. 2.19, for example, $\hat{\omega} = 4.51$. These motions have multiple periodicities.
- The motion switches from the planar oscillatory response to 3D whirling response, and then back to planar oscillation. During the transition from

2D to 3D response, there is a range of frequencies, in which the planar to 3D transient response shown in Fig. 2.19 occurs. As the driving frequency increases further, this phenomenon repeats.

2.5.2 Comparison of Experiments and Analysis

We now turn to a quantitative comparison of the results of the experiments and analysis. In Fig. 2.17, the numerical solutions of the mode shape (X, Z) are superposed on the experimentally observed mode shapes. The corresponding frequencies for both the experimental measurements and theoretical predictions are compared in Table 2.3. The loci of the tip point in the (X_1, X_2) plane with straight lines in Fig. 2.19 correspond to the motion assumed in Eq. (2.23), i.e. the planar oscillation. The circular loci are related to the 3D whirling response, which is the motion assumed in Eq. (2.24). As shown in Fig. 2.19, the two steady-state motions assumed in Eqs. (2.23) and (2.24), are observed for some range of driving frequencies.

Table 2.3: Comparison of the normalized frequency ($\hat{\omega}$) between nonlinear analysis and experimental results. ($L = 0.30m$)

	Mode n	Nonlinear Calculation	Experimental results	difference
In plane motion	2	2.78	2.66	4.6%
	3	4.37	4.48	2.3%
Out of plane whirling	2	2.82	2.87	1.8%
	3	4.44	4.90	9.3%

The in-plane and out-of-plane amplitudes of the free-end tip point $X_\alpha(0)$, $(\alpha = 1, 2)$ were measured from the loci of its motion trajectories. For comparison with the results of the perturbation analysis of the forced motion, these data are plotted in Fig. 2.20a and 2.20b as a function of the normalized driving frequency $\hat{\omega}$. The open symbols represent the planar response, while the filled symbols correspond to 3D motions. The vertical straight lines connecting the data points represent the systematic excursion of the amplitude of the free-end tip points between these data points. The theoretical response calculated from the perturbation analysis is superposed in these figures; for the sake of clarity only the stable 2D (dashed lines) and stable 3D (solid lines) motions are shown. When the driving frequency is far below the 2^{nd} eigenfrequency and above the 1^{st} eigenfrequency, the imposed in-plane motion at the top end excites a small amplitude planar oscillation at the free-end tip point; the experimental points fall close to the stable 2D solution predicted by the perturbation analysis. As the driving frequency approaches the 2^{nd} eigenfrequency, the amplitude of oscillation of the tip increases rapidly and at a certain point, begins to excite the out-of-plane or whirling mode of motion. This is seen in Fig. 2.20b as the out-of-plane amplitude of the tip point increases and approaches the stable 3D branch. As the 2^{nd} eigenfrequency is crossed, the out-of-plane motion is eliminated quickly and only 2D motion of the free tip is observed. Reasonable quantitative agreement between the experiments and the results of the perturbation analysis is observed in Fig. 2.20a and 2.20b. This behavior is observed repeatedly as the driving frequency goes over the higher eigenfrequencies. However, as the driving frequency reaches the 4^{th} eigenfrequency, the experimental results are clearly observed to be frequency-shifted with respect to the theoretical predictions. This is very similar to the response of the whirling string and was shown to be well estimated by bending effects in Chapter 3 that become more important at the higher modes.

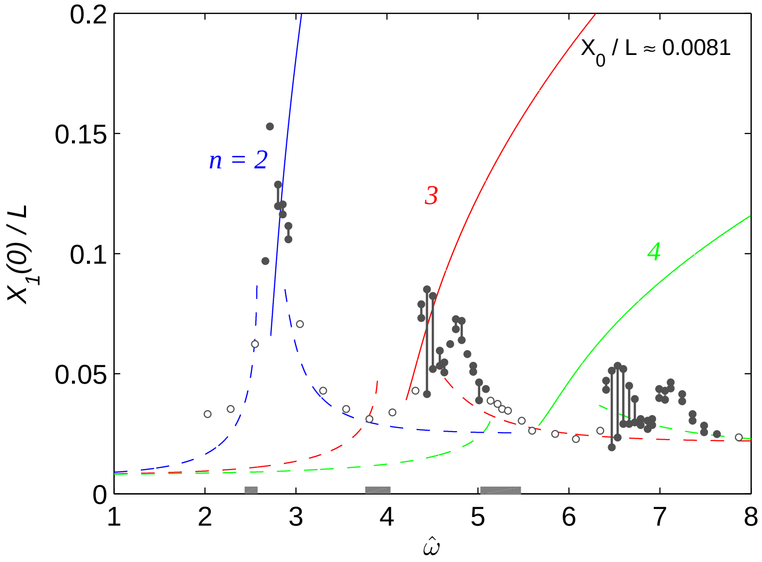

(a) in-plane

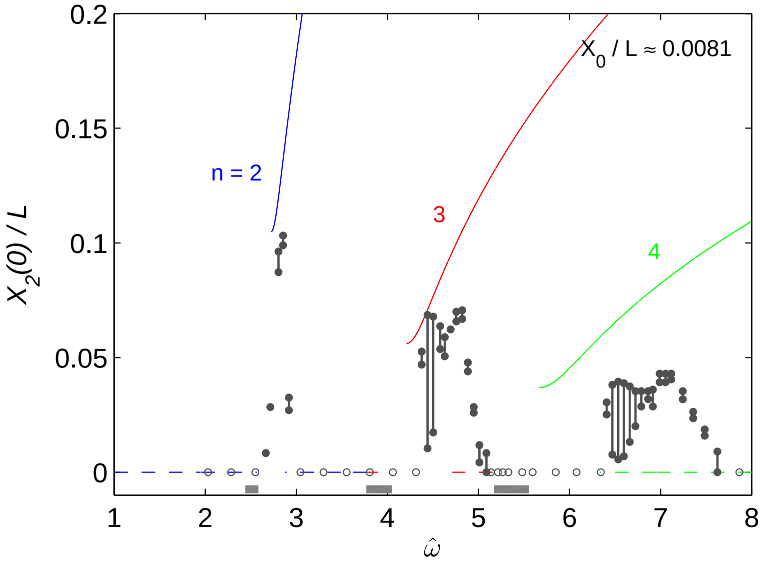

(b) out-of-plane

Figure 2.20: Comparison of the frequency response of the rubber string under planar excitation. The lines are theoretical predictions (solid line: stable 3D; dashed lines: stable 2D) and the circle symbols are the experimental results (filled circles: 3D; open circles: 2D; the vertical lines between some of the filled circles represent the variation of the amplitude). ($L = 0.40m$)

The experimental results indicate that near the frequency range $2.58 < \hat{\omega} < 2.72$ where no stable solutions were found in the perturbation analysis, motions with multiple periodicities and chaotic motions can occur; it is in this range that the systematic excursions in amplitude of oscillations were found. Similar behavior was found at other modes; the expansion of this range of frequencies at higher modes is also confirmed in the experiments. The frequency ranges over which such motions are observed is indicated in Fig. 2.20a and 2.20b with the gray bars along the abscissa. Once again, the shifts in these ranges when compared to the analytical predictions are attributed to the influence of bending. Qualtitative understanding of what occurs in these ranges can be gained by examining the locus images presented in Fig. 2.19. For example, the locus corresponding to $\hat{\omega} = 4.51$, can be interpreted as the string exhibiting a nearly planar motion for a certain duration while it goes into a three dimensional whirling motion for another duration and switching back and forth between these two motions. This response might be influenced significantly by the end support with respect to rotation at the top support. This behavior is repeated again at $\hat{\omega} = 6.67$ for the $n = 4$ mode. In Fig. 2.20b, one could imagine from the data points with a vertical connecting line corresponding to the 4^{th} mode (with a shift in the frequency of the theoretical curves to account for the influence of bending) that the top data points coincide with the stable 3D while the bottom data points coincide with the stable 2D motion and that the string executes a periodic transition between these stable states. Quantitative evolution of this response should be possible, but has not yet been explored.

2.6 Summary

That steady-state solutions exist to the problem of a whirling string under gravitational loading has been known for over half a century; however, except for anecdotal evidence and some brief accounts, to our knowledge, careful experimental assessment of the whirling of strings has not been presented in the literature; in this chapter, we have presented such a detailed examination of this problem. Rubber strings are used as models for the whirling string; while the string is elastic, accommodating changes in tension along its length, the total extension was found to be small enough to be negligible. Furthermore, the bending stiffness of the rubber string is also negligibly small. Thus, the strings are assumed to be inextensible and flexible; the resulting equations of motion for the string are geometrically nonlinear. Kolodner [55] showed that multiple steady-state whirling solutions with a constant axial position exist at any whirling frequency beyond the first resonance of the linearized problem. In our experiments, we found three major departures from this result. First, that steady state motions without time variation in the axial motion is observed only at specific frequencies. Second, while multiple steady-state solutions are available at any frequency, the string settles into steady-state trapped modes that exhibit a significant cyclic axial motion; such trapped modes have been observed and characterized quantitatively for the first time in the present chapter. The trapped modes provide interesting time evolution of the mode shapes of the whirling string; in particular, the trajectories in space of the free end of the string present exciting similarities to the trajectories observed in the motion of flagella of sperm, suggesting possibilities for exploring such motions in the string. Finally, the maximum amplitude that the string may attain is limited to a level that depends on the string length. On the other hand, the motion of a flexible string under small-amplitude planar harmonic excitation has also been studied. The mode shapes and the bifurcation diagram appear to be quite similar to the ones for the whirling motion. 2D response as well as 3D response has been observed. The results of perturbation analysis showed that these 2D to 3D transition are governed by the dynamic instability.

Chapter 3

Planar and Whirling Motions of Thin Filaments

In this chapter, we focus on the steady-state whirling motion of thin filaments based on Kirchhoff's rod theory[1]. Specifically, the coupling effect between tension and bending has been explored. In Section 3.1, the governing equations of the whirling motion of filaments are obtained based on Kirchhoff's theory of slender rods. In Section 3.2, the system of nonlinear first-order ordinary differential equations (ODE's), which describes the steady-state whirling motion of the inextensible filaments, is presented. The corresponding linearized eigenvalue problem is also discussed in this section. In Section 3.3, we study the numerical solutions of the system of nonlinear first-order ODE's. In particular, the effect of bending is discussed. In Section 3.4, the experimental results for a rubber string and a nylon filament are analyzed and compared to the corresponding numerical predictions.

3.1 Kirchhoff's Theory of Slender Rods

Consider an initially straight rod, with one end attached to a motor rotating at constant angular velocity ω and the other left hanging free under gravity. The main assumptions behind Kirchhoff's rod theory are that the strains are small and that transverse shear effects on the deformation may be neglected. In the fol-

---

[1] Some of the contents of this chapter have been published in *Int. J. Solids Struct.*, **44**, 3035-3048 (2007).

lowing subsections, we formulate the problem of a whirling filament within the framework of the Kirchhoff's theory of slender rods.

3.1.1 Kinematical Description

In order to describe the geometry of the rod during its motion, let us define three coordinate systems, namely, $\hat{\mathbf{e}}_k$, $\hat{\mathbf{b}}_k(s,t)$ and $\hat{\mathbf{a}}_k(s,t)$, as shown in Fig. 3.1. Here, s is a Lagrangian coordinate identifying the position along the neutral axis of the rod and is zero at the fixed end and L at the free end. Specifically, $\hat{\mathbf{e}}_k$ is a given triad of unit vectors fixed in space; the original (undeformed) configuration of the rod is taken to be such that the coordinate origin is sitting at the fixed end of the rod; $\hat{\mathbf{e}}_3$ is the direction of the neutral axis, and $\hat{\mathbf{e}}_\alpha$ are the principal axes of the cross section. We will restrict attention to circular cross-sections; for this cross section, $\hat{\mathbf{e}}_\alpha$ can be chosen as two orthogonal directions oriented arbitrarily in the cross sectional plane.

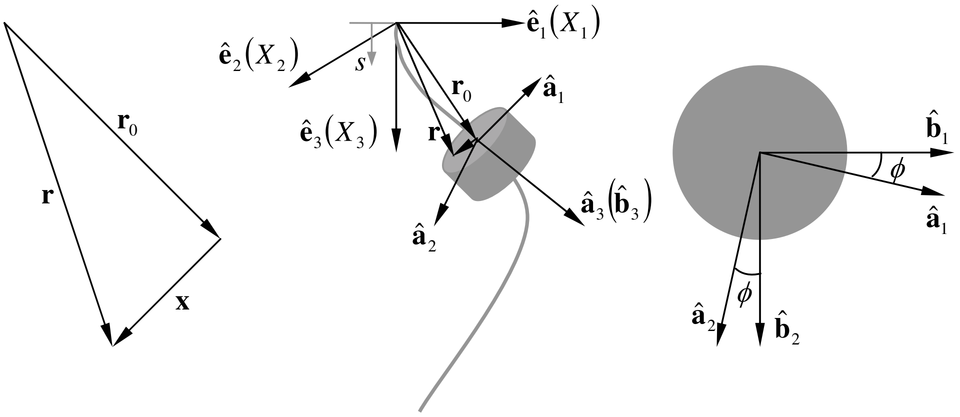

Figure 3.1: Geometric scheme of the segment of the rod.

$\hat{\mathbf{b}}_k(s,t)$ is a triad of local unit vectors for the current (deformed) configuration at each s, before the twist deformation $\phi(s,t)$ is considered. $\hat{\mathbf{b}}_3$ is the tangent vector of the rod, and $\hat{\mathbf{b}}_\alpha$ are the unit vectors associated with the principal axes of the cross section. The origin of the $\hat{\mathbf{b}}$-frame is at the centroid of the cross-section of each segment. The $\hat{\mathbf{a}}_k(s,t)$ coordinate system is obtained by introducing the twist deformation $\phi(s,t)$ about the $\hat{\mathbf{b}}_3$ axis, which is coincident with the $\hat{\mathbf{a}}_3$ axis. Note that the $\hat{\mathbf{b}}$-frame is introduced merely as a convenient step in determining the relationship between the $\hat{\mathbf{e}}$-frame and the $\hat{\mathbf{a}}$-frame.

Now, let us consider the geometrical description of the rod. First, the neutral axis can be represented as a space curve c with position vector

$$\mathbf{r}_0(s,t) = X_k(s,t)\hat{\mathbf{e}}_k \tag{3.1}$$

where X_k are the components of $\mathbf{r}_0$ in the $\hat{\mathbf{e}}$-frame. Second, a point in the rod can be represented by vectors $\mathbf{r}(s,t)$ and $\mathbf{x}(s,t)$, with $\mathbf{r} = \mathbf{r}_0 + \mathbf{x}$, where $\mathbf{x}$ is restricted to the cross sectional plane with $\mathbf{x} = x_\alpha \hat{\mathbf{a}}_\alpha$. For convenience, let $f'(s,t)$ denote the partial derivative of $f(s,t)$ with respect to s and $\dot{f}(s,t)$ denote the partial derivative of $f(s,t)$ with respect to t. Then,

$$\begin{aligned} \lambda = |\mathbf{r}_0'| = \sqrt{(X_1')^2 + (X_2')^2 + (X_3')^2} \\ \mathbf{r}_0' = \lambda \hat{\mathbf{b}}_3(s,t) \\ \hat{\mathbf{a}}_3 = \hat{\mathbf{b}}_3 = \frac{X_k'}{\lambda}\hat{\mathbf{e}}_k. \end{aligned} \tag{3.2}$$

For circular cross-section, the vectors $\hat{\mathbf{b}}_1$ and $\hat{\mathbf{b}}_2$ can be chosen as

$$\hat{\mathbf{b}}_1 = \frac{\hat{\mathbf{e}}_3 \times \hat{\mathbf{b}}_3}{\left|\hat{\mathbf{e}}_3 \times \hat{\mathbf{b}}_3\right|} \tag{3.3}$$

and

$$\hat{\mathbf{b}}_2 = \frac{\hat{\mathbf{b}}_3 \times \hat{\mathbf{b}}_1}{\left|\hat{\mathbf{b}}_3 \times \hat{\mathbf{b}}_1\right|} \tag{3.4}$$

and the relation between $\hat{\mathbf{b}}_k$ and $\hat{\mathbf{a}}_k$ can be obtained by accounting for the twist deformation $\phi(s,t)$.

$$\begin{pmatrix} \hat{\mathbf{a}}_1 \\ \hat{\mathbf{a}}_2 \\ \hat{\mathbf{a}}_3 \end{pmatrix} = \begin{pmatrix} \cos\phi & \sin\phi & 0 \\ -\sin\phi & \cos\phi & 0 \\ 0 & 0 & 1 \end{pmatrix} \begin{pmatrix} \hat{\mathbf{b}}_1 \\ \hat{\mathbf{b}}_2 \\ \hat{\mathbf{b}}_3 \end{pmatrix}. \tag{3.5}$$

After some mathematical manipulation, the relation between deformed configuration $\hat{\mathbf{a}}_k$ and the reference configuration $\hat{\mathbf{e}}_k$ can then be written as

$$\hat{\mathbf{a}} = \mathbf{Q}\hat{\mathbf{e}} \tag{3.6}$$

where $\hat{\mathbf{a}} = (\hat{\mathbf{a}}_1, \hat{\mathbf{a}}_2, \hat{\mathbf{a}}_3)^T$, $\hat{\mathbf{e}} = (\hat{\mathbf{e}}_1, \hat{\mathbf{e}}_2, \hat{\mathbf{e}}_3)^T$, and the transformation matrix

$$\mathbf{Q} = \begin{pmatrix} -\frac{1}{\gamma}\left(X_2' \cos\phi + \frac{X_1' X_3'}{\lambda} \sin\phi\right) & \frac{1}{\gamma}\left(X_1' \cos\phi - \frac{X_2' X_3'}{\lambda} \sin\phi\right) & \frac{\gamma}{\lambda}\sin\phi \\ \frac{1}{\gamma}\left(X_2' \sin\phi - \frac{X_1' X_3'}{\lambda} \cos\phi\right) & -\frac{1}{\gamma}\left(X_1' \sin\phi + \frac{X_2' X_3'}{\lambda} \cos\phi\right) & \frac{\gamma}{\lambda}\cos\phi \\ \frac{X_1'}{\lambda} & \frac{X_2'}{\lambda} & \frac{X_3'}{\lambda} \end{pmatrix} \tag{3.7}$$

where $\gamma^2 = (X_1')^2 + (X_2')^2$. The transformation matrix $\mathbf{Q}$ is orthonormal. So far, the relation between $\hat{\mathbf{e}}$-frame and $\hat{\mathbf{a}}$-frame has been established in Eq. (3.6). Now, we can find the spatial and temporal derivates of $\hat{\mathbf{a}}_k$.

$$\begin{pmatrix} \hat{\mathbf{a}}_1' \\ \hat{\mathbf{a}}_2' \\ \hat{\mathbf{a}}_3' \end{pmatrix} = \begin{pmatrix} 0 & \kappa_3 & -\kappa_2 \\ -\kappa_3 & 0 & \kappa_1 \\ \kappa_2 & -\kappa_1 & 0 \end{pmatrix} \begin{pmatrix} \hat{\mathbf{a}}_1 \\ \hat{\mathbf{a}}_2 \\ \hat{\mathbf{a}}_3 \end{pmatrix}, \tag{3.8}$$

$$\begin{pmatrix} \dot{\hat{\mathbf{a}}}_1 \\ \dot{\hat{\mathbf{a}}}_2 \\ \dot{\hat{\mathbf{a}}}_3 \end{pmatrix} = \begin{pmatrix} 0 & \omega_3 & -\omega_2 \\ -\omega_3 & 0 & \omega_1 \\ \omega_2 & -\omega_1 & 0 \end{pmatrix} \begin{pmatrix} \hat{\mathbf{a}}_1 \\ \hat{\mathbf{a}}_2 \\ \hat{\mathbf{a}}_3 \end{pmatrix} \tag{3.9}$$

where κ_1 and κ_2 are the curvatures and κ_3 is the twist of the rod measured in $\hat{\mathbf{a}}$-frame; ω_i's are the components of the angular velocity measured in $\hat{\mathbf{a}}$-frame.

Finally, by combining Eqs. (3.6), (3.8) and (3.9), we find the expressions for κ_i and ω_i in terms of Q_{ij}:

$$\begin{cases} \kappa_1 = Q'_{2i}Q_{3i} \\ \kappa_2 = Q'_{3i}Q_{1i} \\ \kappa_3 = Q'_{1i}Q_{2i} \end{cases} \tag{3.10}$$

and

$$\begin{cases} \omega_1 = \dot{Q}_{2i}Q_{3i} \\ \omega_2 = \dot{Q}_{3i}Q_{1i} \\ \omega_3 = \dot{Q}_{1i}Q_{2i} \end{cases} . \tag{3.11}$$

At this point, the kinematical description of $\mathbf{r}_0(s,t)$ of the model problem has been established. We turn to the balance of momentum in the next subsection.

3.1.2 Balance of Momentum

Now, we are ready to present the balance of momentum for an infinitesimal segment ds of the rod based on the continuum theory. From the free-body-diagram shown in Fig. 3.2, it is clear that the balance of linear momentum can be written as

$$\mathbf{F}' + \mathbf{f} = \rho A \ddot{\mathbf{r}}_0 \tag{3.12}$$

where the forces $\mathbf{F}$ exerted by the neighboring segments acting on the segment ds are $\mathbf{F} = F_k\hat{\mathbf{a}}_k$. ρ is the mass density per unit volume and A is the cross-sectional area of the rod. In general, the body force density per unit length, $\mathbf{f}$, may act in arbitrary orientations; however, if we consider that the rod is in a gravitational field directed along $\hat{\mathbf{e}}_3$, $\mathbf{f} = \rho A g Q_{k3}\hat{\mathbf{a}}_k$. Then, equation (3.12) can be written in the $\hat{\mathbf{a}}$-frame as indicated below.

$$\begin{cases} F'_1 + \kappa_2 F_3 - \kappa_3 F_2 + \rho A g Q_{13} = \rho A \ddot{X}_j Q_{1j} \\ F'_2 + \kappa_3 F_1 - \kappa_1 F_3 + \rho A g Q_{23} = \rho A \ddot{X}_j Q_{2j} \\ F'_3 + \kappa_1 F_2 - \kappa_2 F_1 + \rho A g Q_{33} = \rho A \ddot{X}_j Q_{3j} \end{cases} . \tag{3.13}$$

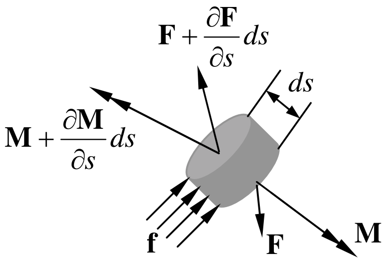

Figure 3.2: Free-body-diagram of an infinitesimal rod segment ds

The balance of angular momentum for the segment ds shown in Fig. 3.2 is

$$\mathbf{M}' + \mathbf{r}_0' \times \mathbf{F} + \mathbf{m} = \iint_A \mathbf{x} \times \ddot{\mathbf{r}} \rho dx_1 dx_2. \tag{3.14}$$

The moments $\mathbf{M}$ exerted by the neighboring segments acting on the segment ds are $\mathbf{M} = M_k \hat{\mathbf{a}}_k$. $\mathbf{m}$ represents distributed external moments, such as viscous torque that might arise for a rod rotating in a fluid environment, but these are not considered here. After some mathematical manipulations, equation (3.14) can be written in the $\hat{\mathbf{a}}$-frame as indicated below.

$$\begin{cases} M_1' + \kappa_2 M_3 - \kappa_3 M_2 - \lambda F_2 = \rho I_1 \left(\dot{\omega}_1 + \omega_2\, \omega_3\right) \\ M_2' + \kappa_3 M_1 - \kappa_1 M_3 + \lambda F_1 = \rho I_2 \left(\dot{\omega}_2 - \omega_1\, \omega_3\right) \\ M_3' + \kappa_1 M_2 - \kappa_2 M_1 = \rho \left(\left(I_1 + I_2\right) \dot{\omega}_3 + \left(I_2 - I_1\right) \omega_1 \omega_2\right) \end{cases} . \tag{3.15}$$

Next, we examine the constitutive relations of an initially straight rod. Let us consider the simplest case, i.e. a homogeneous rod made of linear elastic, isotropic material with Young's modulus E, Poisson's ratio ν and shear modulus μ with:

$$\mu = \frac{E}{2(1+\nu)}. \tag{3.16}$$

Using the Bernoulli-Euler bending theory and the Coulomb torsion theory for circular shafts, the expressions relating the moments to the curvatures and twist can be written as

$$\begin{cases} M_1 = EI_1\kappa_1 \\ M_2 = EI_2\kappa_2 \\ M_3 = \mu J\kappa_3 \end{cases} . \tag{3.17}$$

For the circular cross-section with radius R, $I_1 = I_2 = I = \pi R^4/4$ and $J = 2I$. It should be noted that generally, an additional constitutive equation relating the axial tension F_3 to the axial stretch λ is needed. Here, the filament is considered to be inextensible and the condition $\lambda = 1$ is used as a constraint instead of this constitutive equation. Material properties of rubber and nylon used in this investigation are given in Table 2.1.

3.2 Steady-State Whirling Motion

Now, we are ready to derive the equations for the steady-state whirling motion based on the kinematical Eqs. (3.6)-(3.11), conservation Eqs. (3.13) and (3.15), and constitutive Eqs. (3.17). Within this theory of bending-torsion of thin filaments with circular cross-section, let us explore the possibility of the following steady-state motion

$$\begin{cases} X_1(s,t) = X(s)\cos\omega t \\ X_2(s,t) = X(s)\sin\omega t \\ X_3(s,t) = Z(s) \end{cases} \tag{3.18}$$

for angular velocity $\omega = const.$ Note that equation(3.18) implies that the filament bends in a plane while this plane rotates at the imposed angular velocity ω. As a consequence of the above, equation (3.7) can be simplified as

$$\mathbf{Q} = \begin{pmatrix} -\cos\phi\sin\omega t - Z'\sin\phi\cos\omega t & \cos\phi\cos\omega t - Z'\sin\phi\sin\omega t & X'\sin\phi \\ \sin\phi\sin\omega t - Z'\cos\phi\cos\omega t & -\sin\phi\cos\omega t - Z'\cos\phi\sin\omega t & X'\cos\phi \\ X'\cos\omega t & X'\sin\omega t & Z' \end{pmatrix} . \tag{3.19}$$

Then, equations (3.10) and (3.11) can be reduced to yield the curvature and angular velocity in the $\hat{\mathbf{a}}$-frame, respectively.

$$\begin{cases} \kappa_1 = (X''Z' - Z''X')\cos\phi \\ \kappa_2 = (-X''Z' + Z''X')\sin\phi \\ \kappa_3 = \phi' \end{cases} \tag{3.20}$$

and

$$\begin{cases} \omega_1 = \omega X' \sin\phi \\ \omega_2 = \omega X' \cos\phi \\ \omega_1 = \omega Z' \end{cases} . \tag{3.21}$$

Love (1927) [62] showed that, for the static problem of rods that possess double symmetry of the cross-sectional plane, the twist equations simply imply that a certain rate of twist must be maintained along the rod; this can be seen to be true also for the dynamic problem in the last of Eq. (3.15). Furthermore, for steady-state motion, we get $\kappa_3' = 0$, which together with the free end boundary condition $M_3(L) = 0$, leads to $\kappa_3 = 0$. Then, equations (3.13) and (3.15) can be simplified to yield the following governing equations

$$\begin{cases} F_1' = \rho A\omega^2 XZ' \sin\phi - \kappa_2 F_3 - \rho AgX' \sin\phi \\ F_2' = \rho A\omega^2 XZ' \cos\phi + \kappa_1 F_3 - \rho AgX' \cos\phi \\ F_3' = -\rho A\omega^2 XX' + \kappa_2 F_1 - \kappa_1 F_2 - \rho AgZ' \end{cases} \tag{3.22}$$

and

$$\begin{cases} EI\kappa_1' = \rho I\omega^2 X'Z' \cos\phi + F_2 \\ EI\kappa_2' = -\rho I\omega^2 X'Z' \sin\phi - F_2 \\ \kappa_3 = 0 \end{cases} . \tag{3.23}$$

The last equations in Eqs. (3.20) and (3.23) imply $\phi' = 0$. Furthermore, the free end boundary condition $\phi(L) = 0$ leads to $\phi = 0$ for the steady-state whirling motion.

In addition, the inextensibility condition allows us to simplify the above equations by defining a new variable $\theta = \theta(s)$, such that

$$\begin{cases} X' = \sin\theta \\ Z' = \cos\theta \end{cases} . \tag{3.24}$$

In fact, with the above definition, θ represents the slope angle of the deformed filament in (X, Z) plane. Then Eq. (3.20) become

$$\kappa_1 = \theta', \kappa_2 = 0, \kappa_3 = 0. \tag{3.25}$$

The second equation in Eq. (3.23) implies $F_1 = 0$. By considering Eqs. (3.22)-(3.25), we end up with the system of first-order nonlinear $ODEs$

$$\begin{cases} X' = \sin\theta \\ Z' = \cos\theta \\ \theta' = \kappa_1 \\ \kappa_1' = \frac{1}{EI}\left(\rho I \omega^2 \sin\theta\cos\theta + F_2\right) \\ F_2' = \rho A \omega^2 X \cos\theta + \kappa_1 F_3 - \rho A g \sin\theta \\ F_3' = -\rho A \omega^2 X \sin\theta - \kappa_1 F_2 - \rho A g \cos\theta \end{cases} . \tag{3.26}$$

These equations describe the large deflection bending of a beam in a plane with the distributed load arising from both the gravitational effect and the inertia of the rotation. The boundary conditions are

$$\begin{cases} X(0) = 0 \\ Z(0) = 0 \\ \theta(0) = 0 \\ \kappa_1(L) = 0 \\ F_2(L) = 0 \\ F_3(L) = 0 \end{cases} . \tag{3.27}$$

The system of first order ODE's (3.26) together with boundary conditions (3.27) form the nonlinear two-point boundary value problem. Before turning to solve the fully nonlinear problem, let us consider the small deflection case, i.e. the linearized problem.

3.2.1 Linearized Eigenvalue Problem

For the small amplitude deflection ($Z \approx s$ and $\theta \ll 1$), $\sin\theta \approx \theta$ and $\cos\theta \approx 1$. Retaining only the terms up to first order, equation (3.26) can then be simplified to yield a single fourth order ODE

$$EIX'''' - \rho I\omega^2 X'' - \rho A\omega^2 X - \rho Ag\left(\left(L - s\right)X'\right)' = 0 \tag{3.28}$$

together with boundary conditions $X(0) = 0$, $X'(0) = 0$, $X''(L) = 0$ and $X'''(L) = 0$. This defines the linear eigenvalue problem for ω that can be solved numerically to find the eigenvalues ω_n. The first and third terms in Eq. (3.28) are the typical bending and distributed transverse loading contributions, the second term arises from rotary inertia and the last term represents the effect of gravity. Furthermore, if we neglect the effects of rotary inertia and gravity, equation (3.28) can be reduced to

$$X'''' - \frac{\rho A\omega^2}{EI}X = 0. \tag{3.29}$$

This is the governing equation for steady-state whirling motion of a cantilever beam. The first three eigenvalues ω_n for the rubber and nylon filament based on Eqs. (3.28) and (3.29) are given in Table 3.1. For convenience, the frequency is normalized as $\hat{\omega} = \omega\sqrt{L/g}$, facilitating easy comparison with the string solutions as discussed in Chapter 2. As can be seen from Table 3.1, equation (3.29) gives good approximation for Nylon filament but not for rubber string with very low bending stiffness. Hence, it is appropriate to ignore the effects of rotary inertia and gravity for the filaments with high bending stiffness, such as Nylon; on the other hand, it is important to include these effects for the filaments with lower bending stiffness, such as rubber, if it is to be modeled as a filament. The linear theory predicts that the filament can only whirl at $\omega = \omega_n$, but the simple experimental observation tells us that this is not true and hence the nonlinear effects will be investigated by solving the fully nonlinear Eq. (3.26) numerically in the next section.

Table 3.1: Linear whirling eigenfrequency for rubber and nylon filament. ($\hat{\omega}_n$)

n	Rubber	Rubber	Nylon	Nylon
	Eq. (3.28)	Eq. (3.29)	Eq. (3.28)	Eq. (3.29)
1	1.21	0.038	1.64	1.06
2	2.79	0.24	7.28	6.65
3	4.50	0.66	19.30	18.64

3.3 Numerical Simulations

Equation (3.26) together with (3.27) constitute a nonlinear eigenvalue problem for the steady-state whirling shape of the slender rod or the thin filament; it is the counterpart of the nonlinear eigenvalue problem for a string that was considered by Kolodner [55]. In analogy to that problem, we expect that for any frequency $\omega \geq \omega_n$, where ω_n are the eigenvalues of the corresponding linearized problem, there are n mode shapes that are available for the whirling of the rod (when $n > 1$). The eigenvalue problem which consists of six nonlinear first-order ODE's can be solved by using finite difference method [81]. Material parameters corresponding to the thin filaments of different bending stiffness used in the simulations are listed in Table 2.1. The steady-state solution can be determined by specifying either the rotational speed ω or the amplitude $X(L)$ of the free end as the input, and searching for the other one. The whirling shapes $(X(s), Z(s))$ and the corresponding internal forces, i.e. tension $F_3(s)$, in-plane shear force $F_2(s)$ and in-plane bending moment $M_1(s)$ are then calculated easily. The results of numerical simulation are described in the following paragraphs.

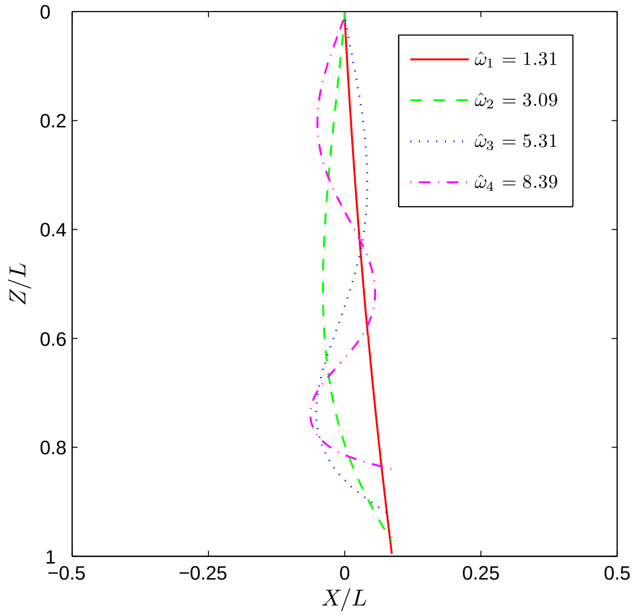

Figure 3.3: Whirling shapes at different driving frequencies corresponding to $X(L)/L = 0.087$. (Material: rubber with $EI = 2.29 \times 10^{-8} N \cdot m^2$)

First, we fix the material parameters to correspond to that of rubber and obtain the steady-state solution at different frequencies of whirling. For a given amplitude $X(L)/L$ of the free end, there exist several solutions corresponding to different mode shapes and frequencies that satisfy Eqs. (3.26) and (3.27). From such simulations, we show in Fig. 3.3 the mode shapes corresponding to a fixed tip deflection $X(L)/L = 0.087$, at four different whirling frequencies $\hat{\omega} = 1.31$, 3.09, 5.31, and 8.39. The corresponding variations of the normalized tension, transverse shear force and bending moment along the length of the filament are shown in Fig. 3.4. The mode shapes are somewhat different from the solutions that are

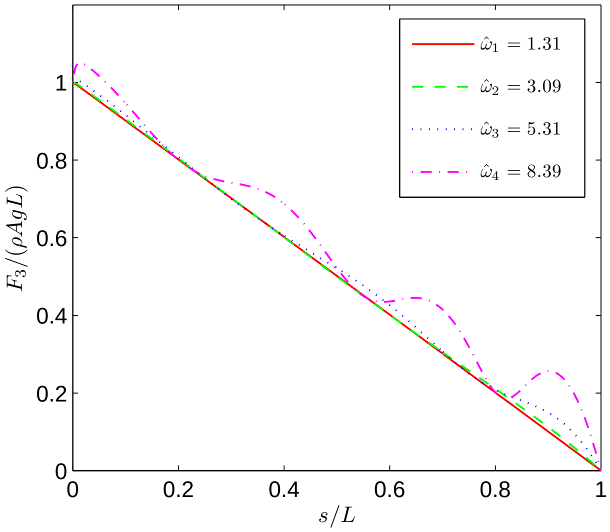

(a) Tension

Figure 3.4: Normalized internal forces distributions along the length of the filament at different driving frequencies with $X(L)/L = 0.087$.

predicted by the string model. In a similar manner, we perform an exhaustive numerical search in the $X(L)/L - \hat{\omega}$ space in order to construct the bifurcation diagram for the whirling motion of the rubber filaments based on the Kirchhoff's rod theory; this result is shown in Fig. 3.5, where the amplitude of the free end of the steady-state whirling, $X(L)/L$, is shown as a function of the normalized whirling frequency $\hat{\omega}$. For comparison, the corresponding result for a whirling string is shown superposed in the same figure. For the rubber cord, with a small bending rigidity of $EI = 2.29 \times 10^{-8} N \cdot m^2$, the steady-state whirling behavior with and without bending effect appear to be qualitatively similar. Quantitatively significant differences appear only for higher modes and then, only for smaller amplitudes. We will examine these through experiments in the next section.

Second, in order to examine the influence of the relatively large bending

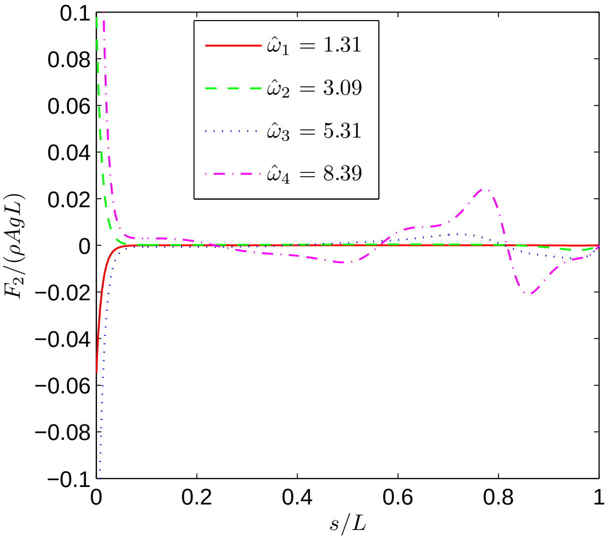

(b) Shear force

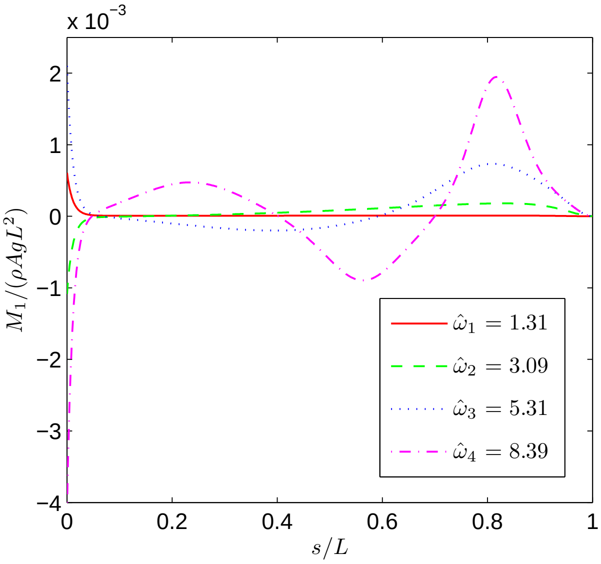

(c) Bending moment

Figure 3.4: Normalized internal forces distributions along the length of the filament at different driving frequencies with $X(L)/L = 0.087$. Cont'd

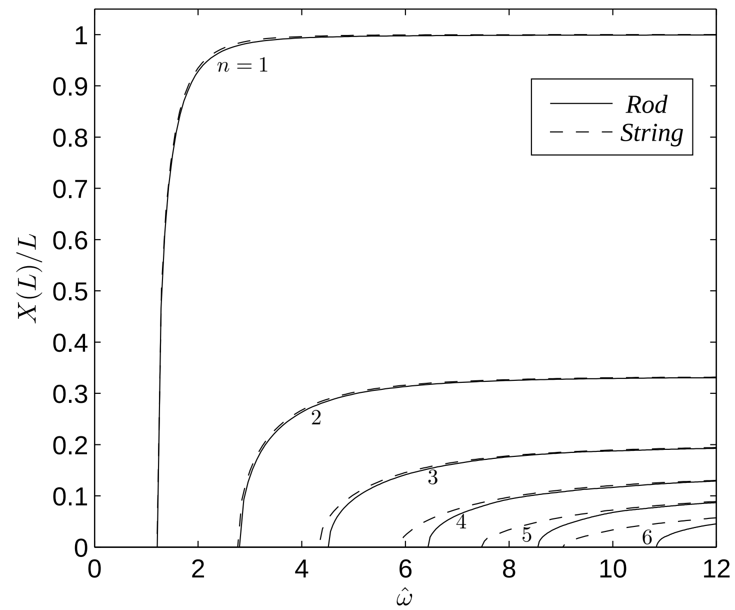

Figure 3.5: Comparison of bifurcation diagram of whirling motion between the string model and the rod theory (Material: rubber with $EI = 2.29 \times 10^{-8} N \cdot m^2$)

rigidity, another set of simulations was performed with material properties corresponding to a Nylon fishing line. The mode shape, tension, shear force and bending moment distributions corresponding to $n = 2$ are shown in Fig. 3.6, together with a comparison of the corresponding mode for the string; clearly as EI increases, bending effects become more significant. The most obvious deviations are to be found near the fixed support at $s = 0$, where the slope must be zero if bending is important. The bifurcation diagram corresponding to this simulation is shown in Fig. 3.7, but only for $n = 2$; for comparison, the results for a string and the rubber filament are plotted in the same figure. For the Nylon filament, with bending rigidity $EI = 1.78 \times 10^{-5} N \cdot m^2$, steady-state solutions corresponding to the $n = 2$ mode are available over a wider range of frequencies, but these are shifted to higher frequencies in comparison to the string. For example, small

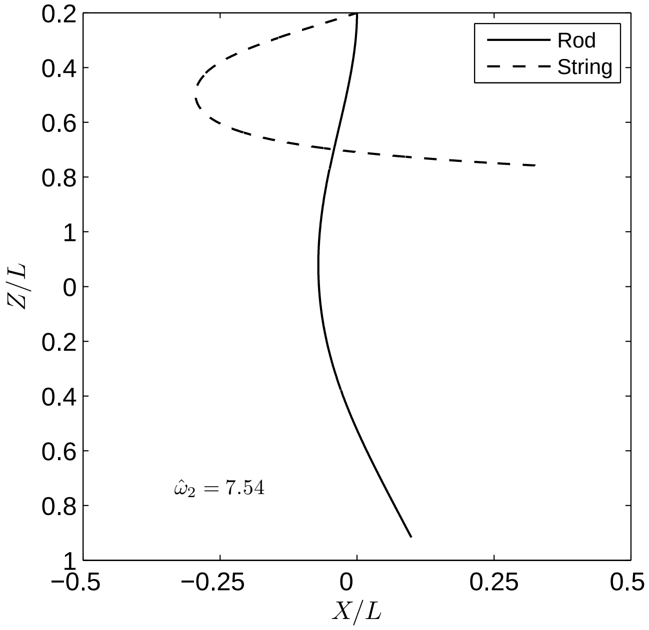

(a) Mode shapes.

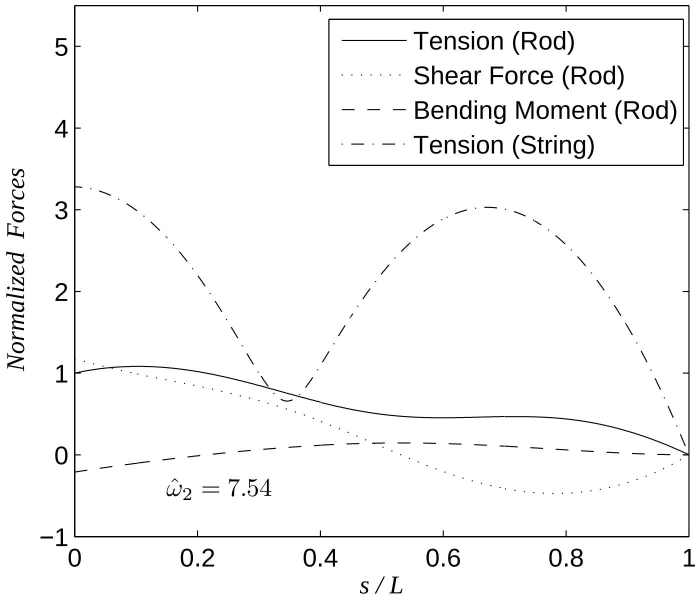

(b) Tension, shear force and bending moment distributions.

Figure 3.6: Comparison of the theoretical predictions for mode $n = 2$ between the string model and the rod theory.

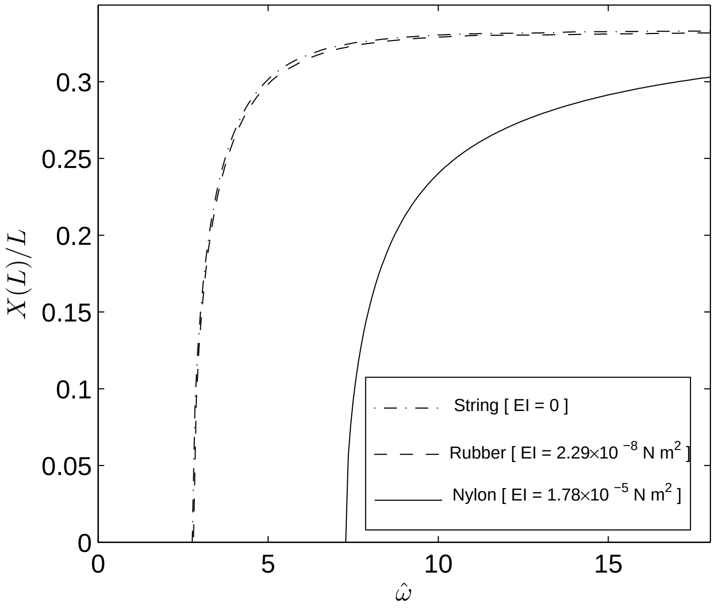

Figure 3.7: Variations of the free-end amplitude with the whirling frequency for mode $n = 2$ are compared for filaments with different bending rigidities.

amplitude motion in the mode $n = 2$ appears at a normalized frequency of 2.8 for the string with negligible bending rigidity, while the Nylon exhibits this solution at a normalized frequency of 7.3. For filaments of other materials such as glass, carbon, steel, etc, EI increases significantly and bending effects will become more and more evident. On the other hand, as the diameter of the filaments become extremely small (with diameters in the range of μm), EI can be made extremely small and bending effects diminish. Our eventual goal is to apply these considerations to the motion of sperm driven by a single flagellum; the bending rigidity for the flagella have been estimated to be around $EI \sim 10^{-22} N \cdot m^2$ [89], and hence the response of the flagella may be modeled with the simple string equations rather than the more complicated bending equations, which will be studied in the following chapters. In the next section, we present results of an experimental investigation to examine the effects of different bending rigidity on whirling motion of the filaments.

3.4 Experimental Results

The influence of bending rigidity was examined directly through experiments on rubber and Nylon filaments. Details of the experimental system have been described earlier in connection with an examination of the whirling of strings and are summarized here briefly. The rubber strings were quite straight and needed no special care in handling, but the Nylon filaments taken from the spool exhibited significant initial curvature. This was minimized by stretching the Nylon filaments to near failure at a temperature of about $140°C$ and holding for about 18 hours, removing the curvature. The rubber and Nylon filaments were attached to a speed-controlled dc motor on one end. A precision-machined sleeve was press fit on the shaft of the motor to ensure proper balancing of the rotating mass. The rubber or Nylon filament was inserted into one end of the sleeve through a small hole and fixed in place with two set-screws. The other end of the filament was left freely hanging thereby replicating the boundary conditions assumed in the problem. Quantitative measurement of the motion of the filaments was obtained using a video imaging system, operated in a time-averaging mode; the image was acquired continuously in a CCD camera over a time of about 0.25 seconds, thus recording the average of many rotations of the whirling filament. This imaging scheme allowed the mode shapes of the whirling motion to be captured and stored for later analysis.

3.4.1 Response of a Whirling Rubber Filament

In chapter 2, we have examined the various modes exhibited by a rubber string subjected to rotary excitation; in particular, we showed that the analysis based on the assumption of negligible bending stiffness was capable of capturing the essential response of the rubber string, but some discrepancy was noted at the higher whirling modes. A part of the experimental results is reproduced here in Fig. 3.8, along with the steady-state solutions that are derived from the bending analysis presented in Section 3.3. This figure shows the bifurcation diagram corresponding to the steady-state solutions (dashed lines correspond to the string analysis, while the solid lines correspond to the solutions of Eqs. (3.26) and (3.27)), together with the measured amplitudes corresponding to the forced motion. It is clear from this figure that while the string analysis is adequate to describe the motion for modes 2 and 3, it is necessary to incorporate bending effects when considering higher modes. Other features exhibited by a whirling rubber string, such as the hysteretic response and the trapped states, have been discussed in Chapter 2 and are not shown in Fig. 3.8.

3.4.2 Response of a Whirling Nylon Filament

In contrast, the experimental observations on the whirling Nylon filament under planar excitation demonstrate the importance of bending effect clearly. Two time-averaged images of the whirling motion of the Nylon filament are shown in Fig. 3.9 corresponding to modes $n = 2$ and 3. The mode shapes calculated from the string and rod equations are shown superposed in the images; the dashed lines in both figures correspond to the string approximation while the solid line is the result of the simulation based on incorporating the appropriate bending stiffness

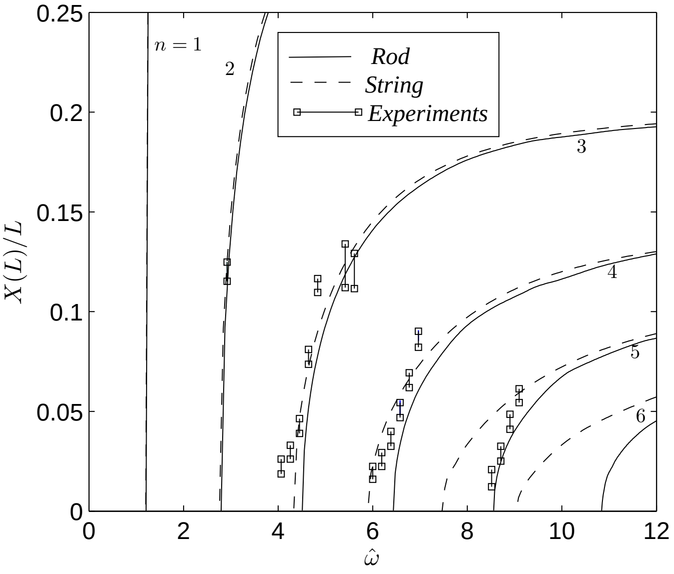

Figure 3.8: Comparison of bifurcation diagram between the numerical prediction and experimental results for rubber string.

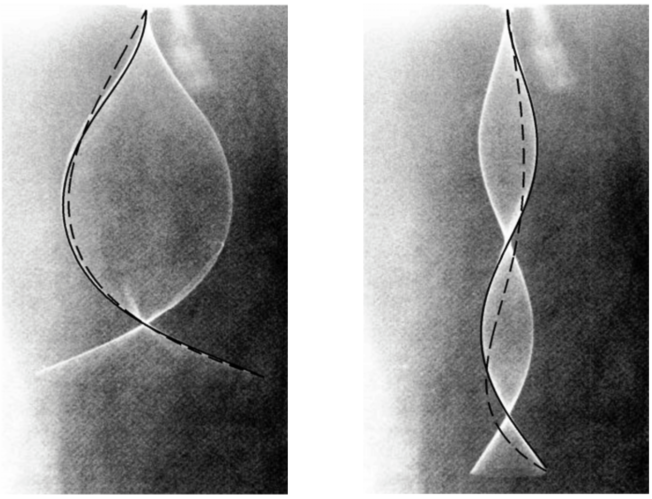

Figure 3.9: Time-averaged images of the nylon filament corresponding to two steady-state whirling modes ($n = 2$ and $n = 3$) are compared with the predictions of the string model (dashed lines) and the rod theory (solid lines). See Table 3 for frequencies used in the experiments and simulations. Images have been histogram equalized to increase visibility of the mode shapes.

of the Nylon. Two options are available in effecting this matching; the first is to calculate the mode shapes with both models at the frequency that corresponds to the experimental condition; this leads to inconsistent amplitudes for the two cases; so we fix the amplitude to be at the experimental value and search for the frequency corresponding to this amplitude and evaluate the mode shape at that frequency. The second approach leads to meaningful comparison between the experimental mode shapes and the simulations; values of the frequencies at which the amplitude matching was obtained are given in Table 3.2. Clearly, bending effects dominate the response of the Nylon filament.

Table 3.2: Comparison of frequencies for whirling of nylon filament ($\hat{\omega}_n$)

Mode n	Matching string solution (no flexural rigidity)	Matching rod solution (nylon)	Experiment
2	3.62	9.49	10.65
3	4.71	20.51	21.49

The complete frequency response of the Nylon filament was examined by capturing the whirling motion at normalized driving frequencies in the range of 4.8 to 22.3. Variation of the amplitude $X(L)/L$ with normalized frequency $\hat{\omega}$ is shown in Fig. 3.10. We explored only the region around the mode $n = 2$; in analogy with the results of the whirling string we anticipate similar response around other modes. The frequency response was obtained by driving the Nylon filament at a given frequency for a few minutes until the starting transients had dissipated completely; at this point a time-averaged image was obtained with the CCD camera and the amplitude at the free end was measured. This procedure was repeated as the frequency was increased or decreased in small steps. A number of observations can be made from the results displayed in this figure.

- The star symbols in Fig. 3.10 indicate amplitude trend with increasing the normalized frequency from 4.8; the amplitude continues to increase with increasing frequency. While we have not calculated the forced response, we expect that it will follow the trends generally seen with the string (see [23] for an approximate solution to the forced motion of a whirling string) or a simple nonlinear oscillator; this trend is indicated by the dashed line.

- As the frequency is increased past the 2^{nd} mode, the filament enters a region of chaotic motion, where the amplitude never settles down; this frequency range is shown by the shaded region in Fig. 3.10. It was in this region that the string exhibited a trapped motion with a periodic modulation of the whirling motion with an axial motion; such trapped-states are absent in the Nylon filament.

- At a certain frequency, it jumps into a stable mode 3 shape and settles down to steady whirling at significantly smaller amplitudes; the steady motions corresponding to continued increase in frequency is indicated by the cross symbols and approaches the bifurcation line corresponding to mode $n = 3$. The dotted lines are again drawn intuitively with the trends derived from the string solutions.

- Upon decreasing the normalized frequency from 21.3, the frequency response retraces the path followed while increasing the frequency until about a normalized frequency of 10.6. The corresponding results are indicated by the filled circles.

- Below a frequency of 10.6, the filament once again enters a regime without any steady motion; as the frequency is decreased further, the string jumps into a mode 2 whirling, with significantly larger amplitude. Continued decrease in frequency results in the filament following the motion observed as the frequency was increased; the corresponding results are indicated by the open circles.

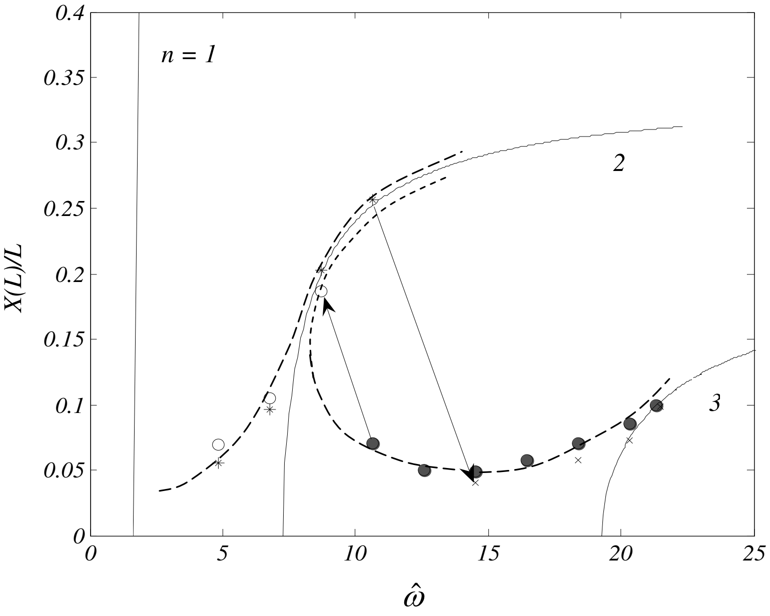

Figure 3.10: Variation of the free-end amplitude with the whirling frequency is compared between the analytical and experimental results of Nylon filament. The star and cross symbols are with increasing frequency and the circle symbols (both hollow and solid) are with decreasing frequency. Dashed lines are free hand lines suggesting expected trends

These experimental observations confirm the trends predicted by the numerical simulations. More importantly, they indicate the range of stiffness in which the bending effects are important.

3.4.3 Response of a Nylon Filament subjected to Planar Excitation

A set of experiments has also been conducted for a Nylon filament subjected to planar harmonic excitation. The imposed motion is $X_1(0,t) = X_0 \cos(\omega t)$, in which X_0 is the forcing amplitude and ω is the driving frequency. The nylon filaments exhibit steady-state mode shapes similar to the flexible string, except at much higher frequencies; the similarity to the whirling problem as discussed in Section 3.2 is notable. In addition to such steady-states, non-steady motion was also observed. The representative images of trajectories of the free-end tip point in the (X_1, X_2) plane at several different driving frequencies are shown in Fig. 3.11. For ease in comparison to the string problem, the frequency is normalized as $\hat{\omega} = \omega\sqrt{L/g}$, even though the characteristic frequency for the bending problem is governed by $\sqrt{EI/(\rho AL^4)}$. A number of observations can be made from these images. Some observations are similar to what has already been stated earlier in connection with the response of rubber strings.

- The 2D oscillatory response is observed for some ranges of the driving frequency, just as in the case of flexible strings. The corresponding locus is a straight line.
- As the driving frequency approaches the eigenfrequency, out-of-plane whirling response begins to emerge, initially with small out-of-plane amplitude $X_2(0)$ then increasing to larger amplitudes. The resulting loci on the (X_1, X_2) plane are either elliptical or circular.
- Further increases in the driving frequency lead to a decrease of the out-of-plane amplitude and the response changes back to the planar oscillation. As

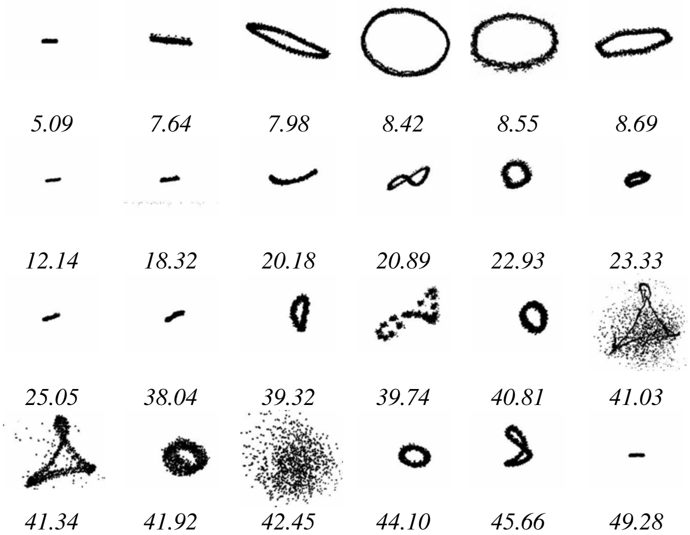

Figure 3.11: Locus of the motion trajectories of the free-end for the Nylon filament subjected to planar excitation. ($\hat{\omega}$: normalized driving frequency and $L = 0.40m$)

the driving frequency is increased further, the response switches from the planar oscillatory motion to 3D whirling motion, and then back to planar motion. During the transition from 2D to 3D motions, there is a range of frequency over which motion with multiple periodicities occurs. This phenomenon repeats as the driving frequency is increased further.

- Interesting patterns of the motions with multiple periodicities are seen clearly in the loci at several driving frequencies. For instance, there are two periodicities for $\hat{\omega} = 20.89$, and 39.74, and three periodicities for $\hat{\omega} = 41.34$. The random black dots in the loci of $\hat{\omega} = 41.03$ and 41.34 represent the chaotic motions besides the primary periodic motion. The pattern at $\hat{\omega} = 41.34$ is one of the examples that show the kinematical similarity to the trajectories of the flagellar motion [94].

- At some higher driving frequencies such as $\hat{\omega} = 42.45$, a chaotic motion appears. This results in the random distribution of black dots in the image.

We now turn to a discussion of comparison between the experimental results and the theoretical analysis for the motion of a nylon filament subjected to planar excitation. The details of the formulations are similar to that for the whirling filaments, which can be found in Sections 3.1 and 3.2. By using the same assumptions as the string in Chapter 2, and due to the intrinsic similarity between the whirling problem and planar motion, one can find the governing equations for the steady-state free motion of the filament subjected to planar excitation as in Eq. (3.26). For the free response of the filament, the boundary conditions can be written as Eq. (3.27)

Similar to the string problem, equation (3.26) represent the envelope of the mode shapes for the planar response; the assumption $X_3(s,t) \approx Z(s)$ is an approximation since the inextensibility constraint is satisfied only approximately for this case. On the other hand, for the 3D whirling response, equation (3.26) describe the motion shape in the rotating $X - Z$ plane, which rotates about the X_3 (or Z) axis at frequency ω.

The solutions of Eqs. (3.26) and (3.27) represent the free response of a filament subjected to planar excitation. It can be treated as a nonlinear two-point boundary value problem for prescribed ω and solved numerically by using finite difference or shooting method [27]. Such numerical solutions indicate that at any frequency $\omega \geq \omega_n$ steady-whirling is possible at n different modes. Furthermore, the amplitude $X_\alpha(L)/L$, $(\alpha = 1, 2)$ of the free-end tip point obtained from this numerical solution is plotted as a function of the normalized driving frequency

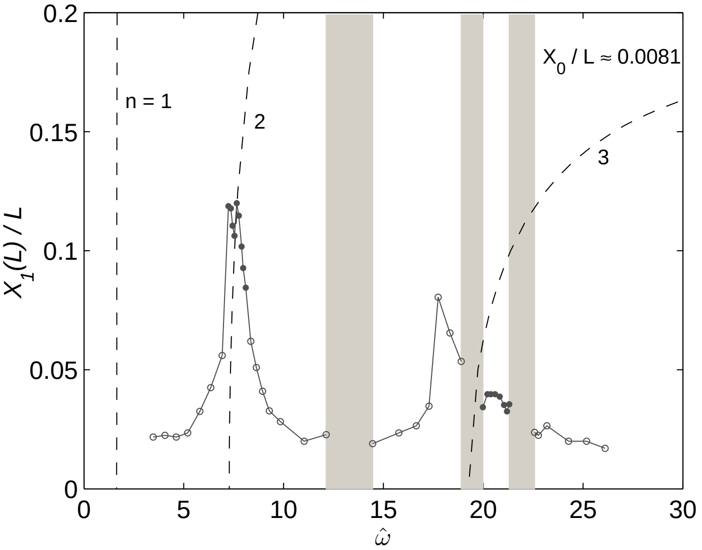

(a) In-plane free-end amplitude

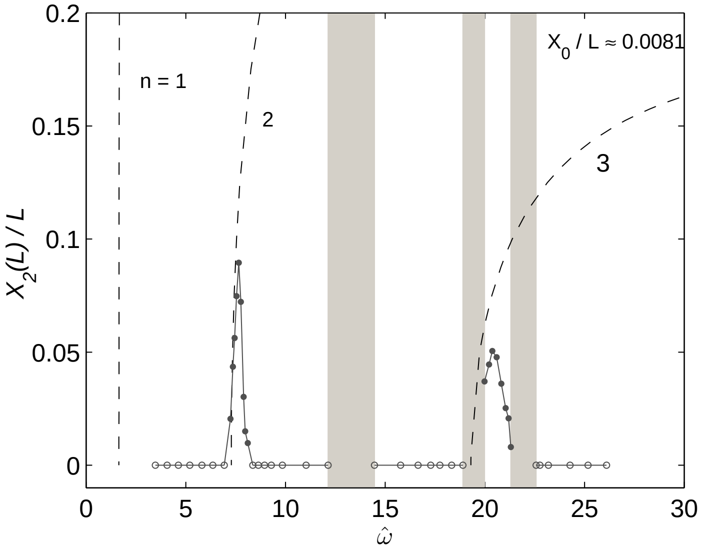

(b) Out-of-plane free-end amplitude

Figure 3.12: Bifurcation diagrams of the motion of the Nylon filament under planar excitation. The dotted lines represent the theoretical steady-state eigensolutions of the free response and the circle symbols represent the experimental data (open symbols represent 2D motion while filled symbols indicate 3D motion); in some frequency ranges, the motions are coupled with multiple periods, which are indicated by the gray rectangles. ($L = 0.40m$)

$\hat{\omega}$ in Fig. 3.12. Thus, the essential features of the response of strings are also seen in the case of filaments, with the major difference that the frequencies at which the different modes appear are shifted to higher values. Comparison to the experimentally measured amplitudes is also shown in Fig. 3.12 (We did not attempt to calculate the forced response, but clearly this can be done in terms of the linearized mode shapes similar to what has been discussed in Section 2.2.3 for the case of the string, but with significantly more difficulty). When driving frequency is far away below the 2^{nd} eigenfrequency of the linearized problem, the imposed in-plane motion at the tip end excites a small amplitude planar oscillation at the free tip. As the driving frequency approaches the 2^{nd} eigenfrequency, the amplitude of oscillation of the tip increases rapidly and at a certain point, begins to excite the out-of-plane or whirling mode of motion. This is seen in Fig. 3.12b as the amplitude of the tip point in the plane perpendicular to the plane of excitation. As the steady-state nonlinear solution is crossed, the out-of-plane motion is abruptly eliminated and once again, only planar motion of the free tip is observed. This behavior is observed repeatedly as the driving frequency goes over the eigenfrequencies of the linearized problem. Clearly, transition to whirling motion is seen near the natural frequencies. In addition, in these filaments, at different frequency bands between the natural frequencies, motion with multiple periodicities and chaotic motion were observed; these bands are indicated in Fig. 3.12 by the manually drawn gray shading.

3.5 Summary

The steady-state nonlinear whirling response of the thin filaments with non-negligible bending stiffness has been studied based on the Kirchhoff's theory of slender rods; these filaments exhibit interesting nonlinear dynamic response. Qualitatively, the response is similar to that observed in the whirling strings with negligible bending stiffness. For a given $\omega \geq \omega_n (n > 1)$, n mode shapes corresponding to different whirling amplitudes exist. Quantitatively, the frequencies at which these solutions appear are higher for the filament with non-negligible bending stiffness than for the string with negligible bending stiffness. Experimental measurements of the forced whirling motion of rubber and Nylon filaments have been used to demonstrate the effect of bending. In contrast to the rubber strings, trapped-steady-state motions were not found in the Nylon filaments, but regions of chaotic motions were identified. In addition, the response of the thin filament subjected to small-amplitude planar harmonic excitation has also been examined. 2D oscillation, 3D whirling response as well as the transition from 2D to 3D have been observed.

Chapter 4

A Tunable Microscopic One-Armed Swimmer

Many micro-organisms in nature propel themselves by spinning or beating their appendices - cilia or flagella [11]. For instance, bacteria rotate their basal motor to spin their relatively rigid helical flagella for their swimming [6]. In contrast, eukaryotic sperms beat their relatively soft flagella for swimming when adenosine triphosphate (ATP) is sufficiently presented in the solvent and thus activates the dynein motors [61]. Recently, a microscopic artificial one-armed swimmer has been demonstrated experimentally [33], which mimics some aspects of the motion of microorganisms but with an externally driven magnetic forcing. Modelling the propulsion of such micro-swimmers has attracted a lot of interest from the biophysics community in past decades [4, 20, 45, 63, 77, 84, 85, 91]. For these micro-swimmers, with length $L \sim 10\mu m$, swimming velocity $V_0 \sim 10^2 \mu m/s$, mass density of fluid $\rho \sim 10^3 kg/m^3$ and fluid viscosity $\mu \sim 10^{-3} N \cdot s/m^2$, the Reynolds number is estimated as $Re = \rho V_0 L/\mu \sim 10^{-3} << 1$. Hence, swimming of such flexible micro-swimmers is well characterized by low-Reynolds-number hydrodynamics [77, 85]. This is fundamentally different from the macroscopic animal kingdom as inertia effects are negligible and the viscous drag dominates their motion. The propulsive force in such micro-swimmers is merely the result of the anisotropy of the hydrodynamic drag in the local normal (η_n) and tangential (η_t) directions, i.e. $\eta_n > \eta_t$ [45].

The reported bending stiffness ranges from 4×10^{-24} to $3.4 \times 10^{-23} N \cdot m^2$ for microtubules [37, 52, 89] and around 10^{-22} to $10^{-21} N \cdot m^2$ for eukaryotic sperm flagella [50, 73, 74]. On the other hand, it ranges from 10^{-24} to $10^{-22} N \cdot m^2$ for the flexible magnetic micro-filaments [33, 43]. It should be noted that we use the symbol A_0 (or A) for bending stiffness in this chapter and the following rather than EI in order to follow the same sign convention as that in the biophysics literatures. In this chapter, we study the low-Reynolds-number dynamics of the nonlinear elastica model and show that, for the micro-filaments with such small bending stiffness, tension plays an important role in varying its effective bending stiffness. Therefore, one can alter the effective bending stiffness of the artificial one-armed micro-swimmer by changing the externally applied tension, for instance, varying the externally applied magnetic field for the magnetic biofilaments, and thus control its swimming velocity and propulsion efficiency. We also characterize the different regimes in which tension or bending dominate the micro-filament elasticity[1].

4.1 Dynamics of Micro-Filaments at Low Reynolds Number

As mentioned above, for a flexible micro-filament immersed in a viscous fluid, the Reynolds number is estimated to be $Re \approx 10^{-3} << 1$. Therefore, the active forces and elastic forces are balanced by the viscous drag. The equation of motion for such a filament can be written as

$$\eta \dot{\mathbf{r}} = -A_0(\kappa' \hat{\mathbf{n}})' + (T\hat{\mathbf{t}})' + \mathbf{f} \tag{4.1}$$

---

[1] Some of the contents of this chapter has been submitted to *Physical Review Letters* for publication .

where the position vector $\mathbf{r}(s,t) = X(s,t)\hat{\mathbf{e}}_1 + Y(s,t)\hat{\mathbf{e}}_2$, $\hat{\mathbf{e}}_1$ and $\hat{\mathbf{e}}_2$ are the unit vectors in the horizontal and vertical directions, respectively, and s is arc length, t represents time; A_0 is the physical bending stiffness; T is the axial force; and $\mathbf{f}$ is the active body force per unit length, for instance, the externally applied magnetic force. For the filament we consider here, the axial deformation is negligibly small compared to the transverse deflection of the filament, i.e. $|\mathbf{r}'| = 1$, such that the local tangent and normal can be written as $\hat{\mathbf{t}} = \mathbf{r}' = X'\hat{\mathbf{e}}_1 + Y'\hat{\mathbf{e}}_2$ and $\hat{\mathbf{n}} = -Y'\hat{\mathbf{e}}_1 + X'\hat{\mathbf{e}}_2$. The local curvature $\kappa = \theta' = Y''/(1-Y'^2)^{1/2}$, with θ the angle between $\hat{\mathbf{t}}$ and $\hat{\mathbf{e}}_1$. Dot and prime represents the temporal and spatial derivatives with respect to t and s, respectively. For a filament whose cross-sectional dimension (radius a) is much smaller than its length L, the well-established theory of slender-body hydrodynamics [29,54] pertains. Hence, the local drag tensor can be written as

$$\eta = \eta_t \hat{\mathbf{t}}\hat{\mathbf{t}} + \eta_n \hat{\mathbf{n}}\hat{\mathbf{n}} = \eta_t \hat{\mathbf{t}}\hat{\mathbf{t}} + \eta_n(\mathbf{I} - \hat{\mathbf{t}}\hat{\mathbf{t}}) \tag{4.2}$$

where $\mathbf{I}$ is the 2D second rank identity; and η_t and η_n are the tangential and normal drag coefficients, respectively. According to the lowest order approximation of the slender-body theory, the drag coefficients are

$$\begin{aligned} \eta_t &= \frac{2\pi\mu}{ln(L/a) + C_1} \\ \eta_n &= \frac{4\pi\mu}{ln(L/a) + C_2} \end{aligned} \tag{4.3}$$

where $C_2 = C_1 + 1$ and the value of C_1 depends on the axial variation of the cross-section [54]. For a filament composed of spheroid particles, $C_1 = -0.5$. This leads to $\eta_n \approx 1.68\eta_t$. On the other hand, $C_1 = -3/2 + ln2 = -0.807$ for a solid circular cylinder, which leads to $\eta_n \approx 1.66\eta_t$ [29]. The boundary conditions at the free tail ($s = L$) are $A_0\kappa(L, t) = 0$ and $A_0\kappa'(L, t) = 0$; the boundary conditions at $s = 0$ depends on the loading condition applied.

Furthermore, the repulsive interactions between the flexible magnetic biofilaments and the externally applied magnetic field may lead to repulsive forces (tensile forces) along the entire filament, which can be very complicated in the real situation. These repulsive forces (i.e. tensions) are in self-equilibrium and decay to zero rapidly at both ends ($s = 0$ and $s = L$) of the filament. In order to keep the mathematical argument simple, we apply a pair of equal, opposite tensions T_0 horizontally at both ends of the filament in our model. This pair of tensile forces is also in self-equilibrium such that no net motion will be generated by T_0 itself, which is consistent with the result of the physically complex repulsive interactions.

4.2 Linear Analysis

For small deflection ($x \approx s$), Eq.(4.1) can be linearized as

$$\eta_n \dot{Y} = -A_0 Y'''' + T_0 Y'' + f_y. \tag{4.4}$$

For general discussion purpose, we consider the transverse forcing function $f_y = Re[\tilde{f}(s)e^{-i\omega t}]$ with frequency ω. The competition between the bending elastic force and hydrodynamic force has been addressed in [63, 91] and is characterized by a nondimensional number, namely "Sperm number" $S_p = L/(A_0/\omega\eta_n)^{1/4}$ [63]. Here, we examine the interplay of bending and tension elasticity; therefore, two characteristic lengths $\ell_b = (A_0/\omega\eta_n)^{1/4}$ and $\ell_t = (T_0/\omega\eta_n)^{1/2}$ that correspond to the first two terms on the right hand side of Eq. (4.4), respectively, can be extracted. Then, two limiting cases can be identified: (i) if $\ell_b >> \ell_t$, bending

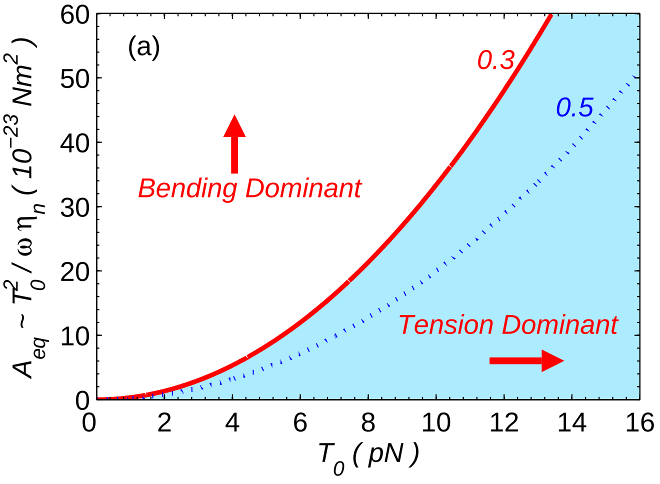

(a)

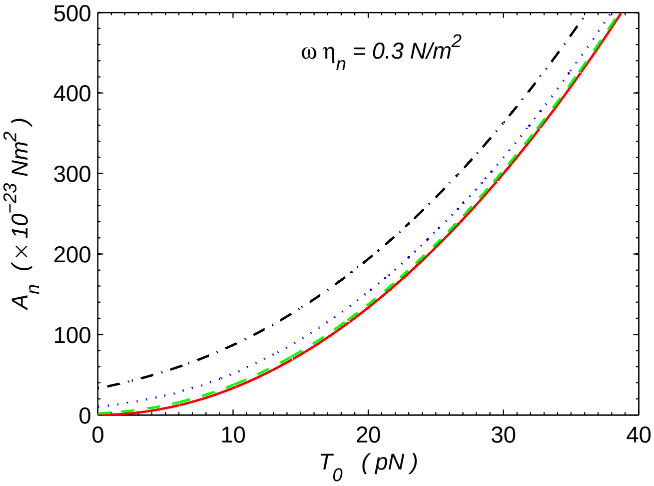

(b)

Figure 4.1: Effective bending stiffness as function of externally applied tension T_0. (a) Equivalent relations between A_{eq} and T_0 for two different $\omega\eta_n[unit : N/m^2]$. (b) effective bending stiffness A_n as function of T_0 for four filaments with different A_0, red solid line: $A_0 = 0N \cdot m^2$; green dashed line: 2×10^{-23} (microtubule); blue dotted line: 10×10^{-23} (magnetic micro-filament); black dash-dotted line: 33×10^{-23} (artificial microswimmer of Dreyfus et al [33]).

dominates and tension can be ignored, which leads to the previous model [20, 63, 91]; (ii) if $\ell_b << \ell_t$, tension dominates and bending force will be relatively unimportant resulting in a so-called string model. By demanding $\ell_b = \ell_t$, we define the equivalent bending stiffness for the string model $A_{eq} = T_0^2/\omega\eta_n$. In order to explore this equivalence quantitatively, we let $\omega \sim 150 rad/s$ and $\eta_n \sim 0.002 N \cdot s/m^2$, resulting in $\omega\eta_n \sim 0.3 N/m^2$; for typical values of driving frequency and fluid viscosity encountered in microscopic swimmers, $\omega\eta_n = 0.1 \sim 1.3 N/m^2$. Figure 4.1a shows the relation between A_{eq} and T_0 for two viscous loads $\omega\eta_n$; the solid line represents the condition under which the elastic energy in the string of tension T_0 is equal to elastic energy in a beam of bending stiffness A_{eq}. Thus, for example, a string with a $10 pN$ tension is equivalent to a filament with a bending stiffness of $33 \times 10^{-23} N \cdot m^2$ when $\omega\eta_n \sim 0.3 N/m^2$ and $20 \times 10^{-23} N \cdot m^2$ when $\omega\eta_n \sim 0.5 N/m^2$. In cases where the effects of bending and tension are comparable, an equivalent characteristic length ℓ can be defined through

$$\frac{A_0}{\omega\eta_n}\ell^{-4} + \frac{T_0}{\omega\eta_n}\ell^{-2} = 1 \tag{4.5}$$

where A_0 is the physical bending stiffness of the filament; this is obtained by considering an equivalent beam with stored elastic energy equal to the sum of the tensile and bending energies.. Similarly, the effective bending stiffness (A_n) of a micro-filament under externally applied T_0 can be calculated by requiring $\ell_b = \ell$

$$\frac{A_n}{A_0} = 1 + \frac{1}{2}\frac{A_{eq}}{A_0} + \left[\frac{A_{eq}}{A_0}\left(1 + \frac{1}{4}\frac{A_{eq}}{A_0}\right)\right]^{1/2}. \tag{4.6}$$

The competition between tension and bending force depends on the motion frequency and fluid viscosity, but is independent of the length of the filament. In cases where the tension is negligible, $A_n \to A_0$ as $T_0 \to 0$; this is the condition that is typically considered in the literature in biophysics. For a perfectly flexible string $A_n \rightarrow A_{eq}$ as $A_0 \rightarrow 0$. We examine the consequences of Eq. (4.6) through a plot shown in Fig. 4.1b of the effective bending stiffness A_n versus the tension T_0 for filaments with different inherent (physical) bending stiffness A_0. Four different cases are shown in Fig. 4.1b. Clearly, as T_0 grows, A_n becomes larger, suggesting that tension should play an important role in determining motion characteristics of micro-filaments. In particular, a tension of $10pN$ increases the stiffness of a single microtubule by an order of magnitude while the bending stiffness of the artificial swimmer can be increased by an order of magnitude with a tension of about $30pN$. These values of tension are easily imposed either in the artificial swimmer through magnetic or optical interactions and in natural swimmers by motor proteins such as dynein. From the above estimates, we suggest that tension must play crucial role in dictating the motion of artificial and natural microscopic swimmers. We examine this further through direct numerical simulations of the fully nonlinear governing equations. (4.1).

4.3 Numerical Simulation

In the numerical simulation study, we use the classical central difference and Euler methods for the spatial and temporal discretization, respectively. The numerical scheme can also be viewed as bead-spring [35] or worm-like chain [65] model, i.e. considering the discretized nodes as spherical beads. For the Euler method, the time step dt has been chosen appropriately to fulfill the numerical stability conditions. It should be noted that the head (for instance, latex and magnetic beads or sperm head) is not considered here, but can be easily incorporated in our model by adding higher viscous drags at the head location. At each time step, the position vector $\mathbf{r}(s,t)$ is calculated for all the nodal points; tension $T(s,t)$ is obtained through constraint dynamics, which is widely used in computing the constraint forces in molecular dynamics simulation of polyatomic systems [1] and has been used by Lowe in [63] to determine the tension in simulating motion by flagella; here, we follow this idea to calculate $T(s,t)$. At each new time step $t+dt$, we solve the system of the linearized inextensibility equation ($|\Delta\mathbf{r}|_{t+dt} = ds$) for all segments to get tension T at each segment. The details are discussed in Appendix A. All the simulations are started from a stress-free straight configuration and settled down to the steady state after enough cycles.

In order to validate our numerical scheme, the simulation for the "fictitious" isotropic viscous drag has been performed first. One-period motion trajectory of the mid-point of the micro-string is plotted in Fig. 4.2. It clearly shows

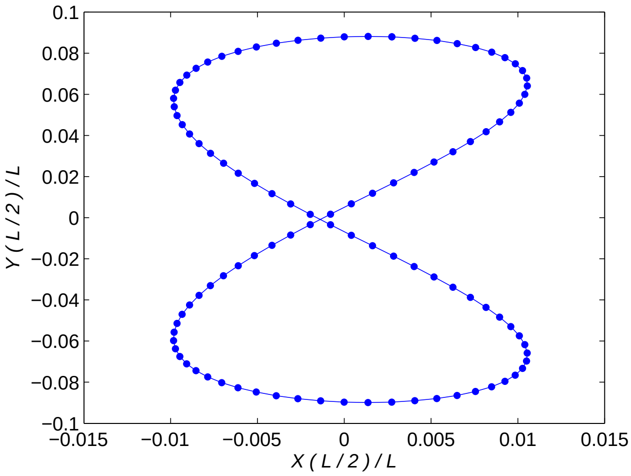

Figure 4.2: Zero net motion for one complete cycle of the driven headless micro-filament ($A_0 = 2 \times 10^{-23} N \cdot m^2$) beating in the fluid with "fictitious" isotropic drag ($\eta_n = \eta_t = \eta$) to validate our numerical scheme. Parameters used here are $\eta_n = \eta_t = 1.3 \times 10^{-3} N \cdot s/m^2$, and $f_y = f_{y0} \cos\left[k\left(s/L - ct\right)\right]$ with $f_{y0} = 1.6 pN/\mu m$, $k = 3.25\pi$, $L = 40\mu m$, $kc = 2\pi \times 50 rad/s$. The time interval between every two points is $\Delta t = 2 \times 10^{-4} s$.

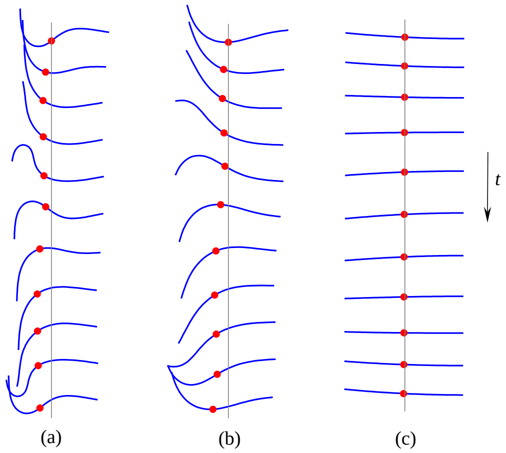

Figure 4.3: Swimming patterns of a micro-filament ($L = 40\mu m$, $a = 125nm$, and viscosity $\mu = 10^{-3} N \cdot s/m^2$) with $A_0 = 10 \times 10^{-23} N \cdot m^2$ subjected to point load $F_{y0}\cos(\omega t)$ at $s = 0$, where $F_{y0} = 50pN$ and $\omega = 2\pi \times 25 rad/s$, for three different T_0. (a) $T_0 = 0pN$ ($L/\ell_t = \infty$); (b) $T_0 = 10.3pN$ ($L/\ell_t = 7$); (c) $T_0 = 504pN$ ($L/\ell_t = 1$). vertical spacing are corresponding to equal temporal interval $\Delta t = 0.004s$. The red dots denote the locations of the midpoint of the filament. For visual reference, the vertical gray lines are aligned with the midpoint of the first(top) swimming pattern.

that zero net motion for the isotropic drag, which agrees with the fact that the swimming is merely due to the anisotropic viscous drag and is also consistent with the linear analysis above.

As an illustration of typical results from the above numerical simulation, the calculated swimming patterns of a micro-filament with $A_0 = 10 \times 10^{-23} N \cdot m^2$ subjected to a transverse point load $F_{y0}\cos(\omega t)$ at $s = 0$. Three different values of tension T_0 have been used in obtaining the results plotted here. In Fig. 4.3a, tension is set to be zero, i.e. $T_0 = 0pN$ ($L/\ell_t = \infty$) such that the swimmer becomes the most compliant, with a physical bending stiffness A_0. The filament exhibits a swimming velocity of $V_0 = 93.9\mu m/s$. In Fig. 4.3b, a tension $T_0 = 10.3pN$

($L/\ell_t = 7$) is added to the filament; the micro-filament becomes stiffer and swims faster with $V_0 = 126.6\mu m/s$; this is approximately the fastest speed in terms of T_0 (L/ℓ_t) observed in this set of numerical simulations. Finally, in Fig. 4.3c, when a very high tension $T_0 = 504pN$ ($L/\ell_t = 1$) is applied, the micro-filament become very stiff such that it behaves like a rigid bar rocking back and forth and its swimming velocity ($V_0 = 10.5\mu m/s$) is very small compared to cases with smaller T_0. This example illustrates that the effective bending stiffness and hence the dynamic response can be controlled or *tuned* by altering the tension imposed on the filament, whether this is done externally or internally.

The swimming velocity and propulsion efficiency (ϵ), which is defined as the amount of energy consumed, relative to the amount of energy required to simply drag a passive filament through the fluid at the same velocity [63], are estimated from the numerical simulations as a function of T_0 for the same loading case as above and are plotted in Fig. 4.4 as a function of length normalized by the characteristic length based on tension for the three different micro-filaments (physical bending stiffness $A_0 = 2, 10, 33 \times 10^{-23} N \cdot m^2$) that have been studied. As shown in Fig. 4.3, the filaments become softer as T_0 decreases. Swimming velocity and propulsion efficiency have peak values at $L/\ell_t = 6 \sim 9$. We note that these curves exhibit significant qualitative similarities to the results of [63], but with quantitative differences brought about by the inclusion of tension. The main upshot of this result is that one can change in situ the externally applied T_0, for example, through changing the horizontal magnetic field for the magnetic filaments, to vary the effective bending stiffness A_n of the filament and thus control its swimming velocity and propulsion efficiency. Of course, this can also be achieved by varying one or more of the following parameters: driving frequency

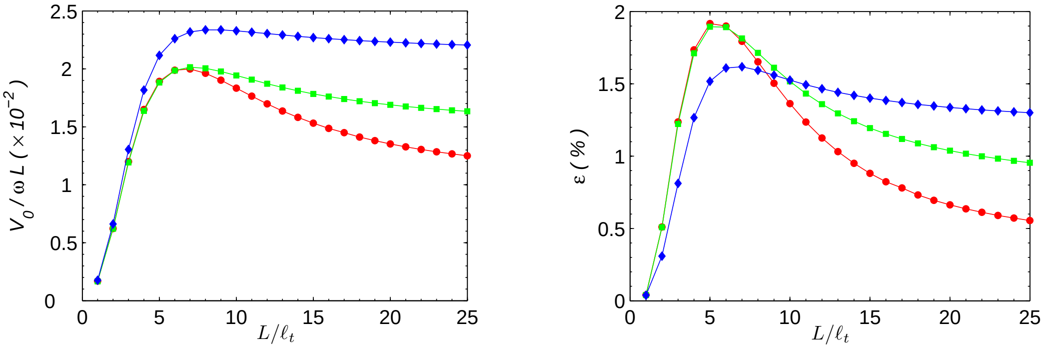

(a) Normalized swimming velocity

(b) Propulsion efficiency

Figure 4.4: Swimming velocity and propulsion efficiency for three micro-filaments with different bending rigidity. Same loading conditions as in Fig. 2. Red circle: $A_0 = 2 \times 10^{-23} N \cdot m^2$; green square: $A_0 = 10 \times 10^{-23} N \cdot m^2$; blue diamond: $A_0 = 33 \times 10^{-23} N \cdot m^2$. Solid lines represent swimming velocity and dashed lines correspond to propulsion efficiency. The symbols represent the computational points, and are connected by straight lines.

ω, fluid viscosity μ, physical bending stiffness A_0 and the geometry of the filament, such as length and cross-sectional dimension, but the proposed mechanism provides a way of actively intervening in the response.

4.4 Summary

The bending stiffness of the flexible micro-filaments is extremely small and is in the range from 10^{-24} to 10^{-22} $N \cdot m^2$ [33, 43]. Here, we study the two-dimensional dynamics of an Euler elastica in low-Reynolds number regime and show that tension effects are comparable to or dominate the bending contributions for the micro-swimmers with such a low bending stiffness. Hence one may change the tension in situ through the externally or internally generated forces, thus changing the effective bending stiffness, and as a consequence controlling the swimming velocity and the propulsion efficiency.

Our results may also be used to explain the diversity of reported data on the microtubule bending stiffness, which vary over one order of magnitude (between 0.4×10^{-23} and $3.4 \times 10^{-23} N \cdot m^2$) [37, 52, 89]. Despite the possibilities of the systematic errors related to different measurement methods and difference in microtubule growth conditions (e.g. growing rate [52]) and other possibilities, tension - which can be due to repulsive forces between different molecules or induced by the flow itself - can also increase the effective bending stiffness A_n similar to what is demonstrated in Fig. 4.1. As a simple illustration, for an assumed viscous load of $0.5N/m^2$, tension of about $4pN$ in a microtubule will increase the effective bending stiffness from about 0.4×10^{-23} to 4×10^{-23}. In the case of swimming sperm flagella, tension or repulsive forces can be generated by many different interactions: the dynein proteins interacting with other molecules, interactions between other proteins in an axoneme (for instance, between the radial spokes and dynein proteins), or repulsive hydration force [51]. As shown in Fig. 4.1a (the dotted line with $\omega\eta_n = 0.5N/m^2$), tension (repulsive force) of even a few piconetwons will have a significant effect on the effective bending stiffness of the sperm flagella, and thus change their swimming behavior. In the examples considered above, we have demonstrated the crucial effect of tension for the biological micro-filaments with such small bending rigidity ($10^{-24} \sim 10^{-22} N \cdot m^2$). As the physical bending stiffness A_0 becomes larger, the effect of tension T_0 will diminish; for instance, T_0 must be as large as $500pN$ such that $A_n \sim 2A_0$ when $A_0 \sim 10^{-18} N \cdot m^2$ and viscous load $\omega\eta_n \sim 0.5N/m^2$. Thus, the present analysis indicates that the effect of internal tension becomes important as the bending stiffness of the filament becomes small and hence must be considered in modelling the dynamics of micro-swimmers and micro-filaments. Finally, it should be noted that, in this study, a pair of tension (or repulsive force) T_0 is applied horizontally at both ends of the filament in the opposite directions. The real situation can be more complicated than this; but the analysis will be similar.

Chapter 5

Dynamics of Flexible Strings at Low-Reynolds Number: Flagellar Swimming

It has been shown, in Chapter 4, that tension plays an important role in micro-swimmers with flexural rigidity in the range of $10^{-24} \sim 10^{-21} N \cdot m^2$. Based on this idea, in this chapter, we study the two-dimensional (2D) low-Reynolds number dynamics of a micro-string with zero bending stiffness, endowed with an internal active force generation capability, and show that the string model is able to capture all the essential aspects of the flagellar motion. Previous studies have proposed a sliding mechanism [15–17,59] and a bending model [20,21,59,63,91] for the flagellar motion. However, the theoretical predictions based on the bending model could not match the experimentally observed flagellar swimming patterns quantitatively [63] and according to Brokaw, "the problem of flagellar movement has not been solved" [18]. In addition to the inherent tension, which is either negligible in the linearized equation [21, 91] or evaluated in the fully nonlinear theory such that the inextensibility constraint is fulfilled [20,63], we postulate that molecular interactions, such as dynein proteins, radial spokes, etc, may generate repulsive forces along the flagella and introduce additional tension of the order of a few pN and hence influence the flagellar dynamics. Through both linear analysis and numerical simulations of the fully nonlinear equations of motion, we demonstrate that the string model reproduces correctly the motion of microscopic one-armed swimmers.

5.1 Equations of Motion

The position of the centerline of the string can be represented by a vector $\mathbf{r}(s,t)$ with

$$\mathbf{r}(s,t) = X(s,t)\hat{\mathbf{e}}_1 + Y(s,t)\hat{\mathbf{e}}_2 \tag{5.1}$$

as shown in Fig. 5.1a. Here s is the Lagrangian coordinate measured from the head of the string towards the tail; t represents time; and $X(s,t)$, $Y(s,t)$ are

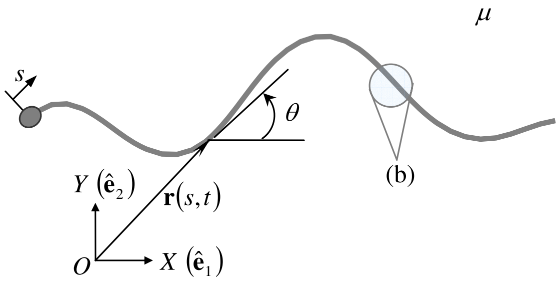

(a) Geometric representation.

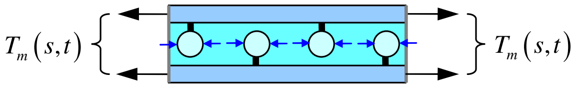

(b) Representation of repulsive interactions between internal molecules that results in tension $T_m(s,t)$ in the filament (external interactions may also provide such tension).

(c) Simplification of $T_m(s,t)$ to T_0.

Figure 5.1: Schematic diagram of a one-armed micro-swimmer swimming in a viscous fluid with viscosity μ.

the corresponding components of $\mathbf{r}(s,t)$ in the global coordinate system $(\hat{\mathbf{e}}_1, \hat{\mathbf{e}}_2)$. We use primes to represent derivates with respect to s and upper dots to denote derivatives with respect to t. Compared to its transverse deflection, the filament can be assumed to be inextensible, i.e.

$$|\mathbf{r}'| = 1. \tag{5.2}$$

Also, we define the local coordinate system $\left(\hat{\mathbf{t}}, \hat{\mathbf{n}}\right)$ with the local unit tangent $\hat{\mathbf{t}} = \mathbf{r}'$ and unit normal $\hat{\mathbf{n}}$, such that

$$\begin{pmatrix} \hat{\mathbf{t}} \\ \hat{\mathbf{n}} \end{pmatrix} = \begin{pmatrix} X' & Y' \\ -Y' & X' \end{pmatrix} \begin{pmatrix} \hat{\mathbf{e}}_1 \\ \hat{\mathbf{e}}_2 \end{pmatrix}. \tag{5.3}$$

For the microscopic swimmers, the Reynolds number has been estimated to be $Re = \rho V_0 L/\mu \sim 10^{-3} << 1$ (see Chapter 4), such that the inertial effects can be ignored and the motion is characterized as low-Reynolds number hydrodynamics. Therefore, the elastic force and the external or internal driving force are balanced by the viscous drag $\mathbf{f}_d = \eta\dot{\mathbf{r}}$. For a flexible string with negligible bending rigidity, the equation of motion can be written as

$$\eta\dot{\mathbf{r}} = (T\mathbf{r}')' + \mathbf{f} \tag{5.4}$$

where T is the physical tension directed along the local tangent; $\mathbf{f}(s,t) = f_x(s,t)\hat{\mathbf{e}}_1 + f_y(s,t)\hat{\mathbf{e}}_2$ is the driving force per unit length, which is distributed along the entire string and can be generated internally, for instance, by the dynein proteins along the flagellum, or externally by the interaction between an applied magnetic field and a flexible magnetic string. The drag tensor η, according to the slender-body hydrodynamics [12,29,54], can be written as Eq. (4.2) and specifically,

$$\eta = \eta_t \begin{pmatrix} X'^2 & X'Y' \\ X'Y' & Y'^2 \end{pmatrix} + \eta_n \begin{pmatrix} 1 - X'^2 & -X'Y' \\ -X'Y' & 1 - Y'^2 \end{pmatrix} \tag{5.5}$$

where **I** is the two-dimensional second rank identity, η_t and η_n are the tangential and normal drag coefficients, respectively. According to the lowest order approximation of the slender-body theory, for a flexible string (cross-sectional radius a and length L) with slenderness $a/L << 1$, the drag coefficients can then be written as Eq. (4.3), in which $C_2 = C_1 + 1$ and the value of C_1 depends on the axial variation of the cross-sectional radius a [25, 29]. For a circular cylinder, $C_1 = -3/2 + \ln 2 = -0.807$ [12, 29], which leads to $\eta_n \approx 1.66\eta_t$. Furthermore, we postulate that the repulsive interactions between different molecules, such as dynein motor proteins, radial spokes, and other molecules of the sperm flagella may generate tension along the entire microtubule, as shown in Fig. 5.1b. These repulsive forces (i.e. tensions $T_m(s,t)$) are in self-equilibrium and decay to zero rapidly at both ends ($s = 0$ and $s = L$) of the flagella. For mathematical simplicity, we simulate these complex repulsive interactions by applying horizontally a pair of two equal, opposite tensile forces T_0 at both ends of the micro-string as shown in Fig. 5.1c, such that there is no net motion due to this pair of tensile forces. In the case of microscopic artificial swimmers, repulsive magnetic interactions may also provide such tensile forces [78]. Hence, the boundary conditions for a swimming micro-string with head at $s = 0$ can be written as

$$\begin{cases} [\zeta_t X'^2 + \zeta_n (1 - X'^2)]\,\dot{X} + [(\zeta_t - \zeta_n)\,X'Y']\,\dot{Y}|_{s=0} = TX'|_{s=0} + T_0 \\ [(\zeta_t - \zeta_n)\,X'Y']\,\dot{X} + [\zeta_t Y'^2 + \zeta_n (1 - Y'^2)]\,\dot{Y}|_{s=0} = TY'|_{s=0} \\ TX'|_{s=L} - T_0 = 0 \\ TY'|_{s=L} = 0 \end{cases} . \tag{5.6}$$

In Eq. (5.6), the head at $s = 0$ is mimicked by applying higher viscous drags with different drag coefficients, ζ_t and ζ_n in the local tangential and normal directions, whose values depend on the shape of the head. If the string is headless, the left hand side of the first two equations in Eq. (5.6) equals zero.

Equations (5.4), (5.2) and (5.6) represent the simple model of low-Reynolds number dynamics of a flexible string. In the following sections, we will first study the analytical solutions corresponding to small-amplitude motion, and then explore the fully nonlinear numerical solutions.

5.2 Linear Analysis: Small-Amplitude Swimming

For small deflections, equation (5.4) can be linearized as

$$\eta_n \dot{Y} - T_0 Y'' = f_y. \tag{5.7}$$

Let us consider an oscillatory transverse driving force of the form $f_y(s,t) = Re\left[\tilde{f}_{y0}(s)e^{i\omega t}\right]$; a characteristic length $\ell_t = (T_0/\omega\eta_n)^{1/2}$ can be extracted from Eq. (5.7). By comparing this characteristic length with the physical length of the micro-string, we define a new dimensionless parameter S_t called "string sperm number" with

$$S_t = \frac{L}{\ell_t} = \frac{L}{(T_0/\omega\eta_n)^{1/2}}, \tag{5.8}$$

which characterizes the competition between the elastic tension and the viscous load. Specifically, two different regimes can be identified: (i) if $S_t << 1$ ($L << \ell_t$), the tension elasticity dominates; (ii) if $S_t >> 1$ ($L >> \ell_t$), the viscous drag dominates. It should be noted that S_t is comparable to the "sperm number", S_p, [63] in the bending model, which characterizes the relative importance between the bending elasticity and the viscous drag.

The solution to the linear equation (5.7) can be obtained by assuming the driving force $f_y(s,t) = Re\left[\tilde{f}_{y0}(s)e^{i\omega t}\right]$ with spatially-variant Fourier amplitude $\tilde{f}_{y0}(s)$, which is generated by some specific mechanism (e.g. dynein motors for the sperm flagella and magnetic interaction for the flexible magnetic filaments). Then, the solution of Eq. (5.7) can be written as $Y(s,t) = Re\left[\tilde{Y}(s)e^{i\omega t}\right]$. $\tilde{Y}(s)$ is the complex Fourier amplitude satisfying

$$T_0\tilde{Y}'' - i\omega\eta_n\tilde{Y} = -\tilde{f}_{y0}, \tag{5.9}$$

The solution of Eq. (5.9) can be expressed as $\tilde{Y}(s) = A(s)e^{-i\phi(s)}$ with the real functions $A(s)$ and $\phi(s)$ denoting the amplitude and phase respectively. Finally, Eq. (5.7) has the following wavelike propagating solution

$$Y(s,t) = A(s)\cos\left(\omega t - \phi(s)\right). \tag{5.10}$$

$\phi'(s) \neq 0$ in Eq. (5.10) ensures $Y(s,-t) \neq Y(s,t)$. Thus, the wave-propagating solution in Eq. (5.10) breaks the time-reversal symmetry and can propel the micro-string. Because of symmetry $Y(s,t) = -Y(s,t+\pi/\omega)$, there is no net motion in the transverse direction. The wave propagation speed depends on the tension T_0, viscosity μ, and the driving frequency ω. Amplitude $A(s)$ can be determined by applying appropriate boundary conditions. In the nonlinear case, the internal tension is nonuniform, but this will only change the local wave speed, not physically alter the wavelike propagating solution. Now, we can calculate the longitudinal swimming speed for this linear analysis. First, the longitudinal component of the hydrodynamic force density is given by

$$f_x^{vis} = -\eta_t\dot{X} + \left(\eta_n - \eta_t\right)\dot{Y}Y'. \tag{5.11}$$

Then, by demanding the resultant longitudinal force $F_x = \int_0^L f_x^{vis}ds = 0$ and time averaging over one period $(2\pi/\omega)$, we find the propulsion velocity

$$V_0 = \frac{\omega}{2\pi}\int_0^{2\pi/\omega} dt\frac{1}{L}\int_0^L \dot{X}ds = -\left(\frac{\eta_n}{\eta_t} - 1\right)\frac{\omega}{2L}\int_0^L A^2\phi' ds. \tag{5.12}$$

Furthermore, we introduced an isotropic viscous drag with much higher drag coefficient ζ to mimic the head at $s = 0$ of the micro-string, the resulting swimming velocity $V = V_0/\left(1 + \zeta/\left(\eta_t L\right)\right)$. A similar analysis of the linearized bending model can be found in [21]. As can be seen from Eq. (5.12), the anisotropy of the drag coefficients plays a crucial role in the propulsion. For a typical string immersed in a viscous fluid, $\eta_n/\eta_t \approx 2$ [45]; and the direction of the motion is opposite to the direction of the wave propagation, indicated by the minus sign on the right hand side of Eq. (5.12). In the following, we will study the fully numerical solutions of the Eq. (5.4).

5.3 Numerical Simulations

In the numerical simulations, we use the finite difference and Euler methods for the spatial and temporal discretizations, respectively. For the Euler method, the time step dt has been chosen appropriately to fulfill the numerical stability conditions. Specifically, the string has been discretized into I identical segments of length ds. At each time step, the position vector $\mathbf{r}(s,t)$ for the $I+1$ nodal points and the tension $T(s,t)$ for the I segments are obtained following the procedures given below.

Tension is calculated by means of constraint dynamics, which is widely used to calculate the constraint forces in molecular dynamics simulation of polyatomic systems [1]. Here, we follow this scheme to calculate the tension in the string. At each new time step $t + dt$, we calculate the new position vector $\mathbf{r}_b|_{t+dt}$ through

$$\mathbf{r}_b|_{t+dt} = \mathbf{r}|_t + dt\left(\eta^{-1}\mathbf{f}\right)|_t \tag{5.13}$$

without considering the contribution from tension. Then, the true position vector

$\mathbf{r}|_{t+dt}$ is the sum of $\mathbf{r}_b|_{t+dt}$ and the contribution from tension.

$$\mathbf{r}|_{t+dt} = \mathbf{r}_b|_{t+dt} + dt \left[\eta^{-1} \left(T\mathbf{r}'\right)'\right]|_t. \tag{5.14}$$

By applying the constraint equation $(\mathbf{r}' \cdot \mathbf{r}')|_{t+dt} = 1$ to all the I segments, specifically, $|\mathbf{r}_{i+1} - \mathbf{r}_i|_{t+dt} = ds$, to the first order approximation, we end up with I linear algebraic equations for $T_i|_{t+dt}$, where $i = 1, 2, ...I$. Finally, plugging $T_i|_t$ into Eq. (5.14), one can compute $\mathbf{r}|_{t+dt}$. The details are discussed in Appendix A. The initial conditions ($t = 0$) used in the following simulations correspond to a straight configuration

$$\begin{cases} X(s,0) = s \\ Y(s,0) = 0 \end{cases} . \tag{5.15}$$

Performing the simulations over a sufficiently long time ($t >> 2\pi/\omega$), we can obtain the steady-state solutions numerically.

In order to validate our numerical scheme, the simulation was performed for the case of “fictitious” isotropic viscous drag. One-period motion trajectory of the mid-point of the micro-string is plotted in Fig. 5.2. It clearly shows zero net motion for the isotropic drag, which agrees with our intuition that the swimming is merely due to the anisotropic viscous drag and is also consistent with the linear analysis above. Moreover, it also indicates that the self-equilibriating tension T_0 imposed as part of the boundary conditions in Eq. (5.6) does not contribute to numerical artifacts that result in net motion of the string. In the following subsections, we will study three aspects of the dynamics of these strings. First, we study the motion generated by the micro-string subjected to oscillatory transverse force/displacement applied at one end $s = 0$. Second, we demonstrate excellent comparison of the simulation results to experimentally observed sperm flagellar motions. This comparison is used to postulate some ideas underlying the

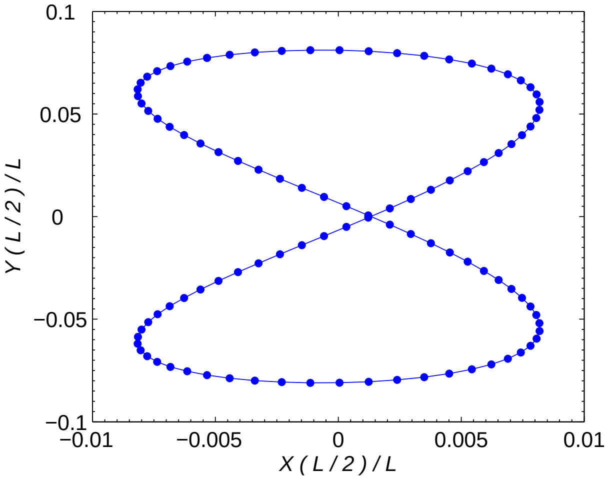

Figure 5.2: Zero net motion for one complete cycle of the driven headless micro-string beating in the fluid with "fictitious" isotropic drag ($\eta_n = \eta_t = \eta$) to validate our numerical scheme. Similar results for the bending model can be found in [63]. Parameters used here are $\eta_n = \eta_t = 1.3 \times 10^{-3} N \cdot s/m^2$, $T_0 = 4pN$, and $f_y = f_{y0} \cos\left[k\left(s/L - ct\right)\right]$ with $f_{y0} = 1.6pN/\mu m$, $k = 3.25\pi$, $L = 40\mu m$, $kc = 2\pi \times 50 rad/s$. The time interval between every two points is $\Delta t = 2 \times 10^{-4} s$.

physics of flagellar propulsion. Finally, comparisons of the string model and beam model to the sperm flagellar waveforms are examined.

5.3.1 Oscillatory Force/Displacement Applied at One End

We first consider the transverse oscillatory force $F_{y0}\cos(\omega t)$ applied at one end ($s = 0$) of the headless micro-string. Temporal sequences of typical swimming patterns for two different values of T_0 (or S_t) are shown in Fig. 5.3. A "stiff" micro-string with $T_0 = 159pN$ ($S_t = 2$) shown in Fig. 5.3a has a swimming velocity of $V_0 = 3.11\mu m/s$, which is very low compared to a "soft" micro-string ($T_0 = 2.83pN$, i.e. $S_t = 15$) with $V_0 = 38.30\mu m/s$ as shown in Fig. 5.3b. Plots of the swimming velocity V_0 of the mid-point ($s = L/2$) and the corresponding propulsion efficiency as functions of T_0 (S_t) under the same loading condition as

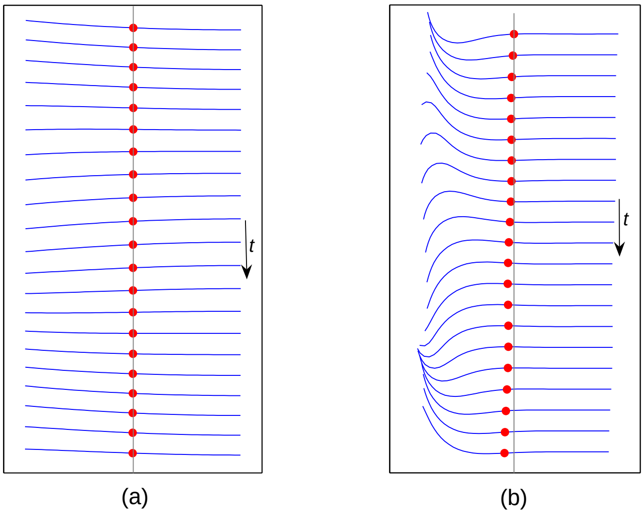

(a) ”Stiff” micro-string with $T_0 = 159pN$ ($S_t = 2$)

(b) “Soft” micro-string with $T_0 = 2.8pN$ ($S_t = 15$)

Figure 5.3: Sequences of swimming patterns of a headless micro-string subjected to a point load $F_{y0}\cos(\omega t)$ at $s = 0$, where $F_{y0} = 16pN$ and $\omega = 2\pi \times 30rad/s$, at two different T_0. The equal time interval between every two patterns is $\Delta t = 0.002s$. The red dots denote the locations of the midpoint of the filament. For visual reference, the vertical gray lines are aligned with the midpoint of the first(top) swimming pattern.

in Fig. 5.3 for three different forcing amplitudes are illustrated in Fig. 5.4a and b. As shown in Fig. 5.4, as S_t increases (or T_0 decreases), both swimming velocity V_0 and propulsion efficiency ϵ increase first, and reach a peak value at certain values of S_t, then drop down. Hence, the swimming velocity as well as the propulsion efficiency of a micro-string can be controlled by changing T_0. In addition, this behavior becomes more pronounced as the forcing amplitude F_{y0} increases, but no qualitatively new phenomena are encountered.

In the second set of simulations, a harmonic displacement boundary condition $Y(0,t) = Y_0 \sin(\omega t)$ was applied at one end ($s = 0$) of the string. Two

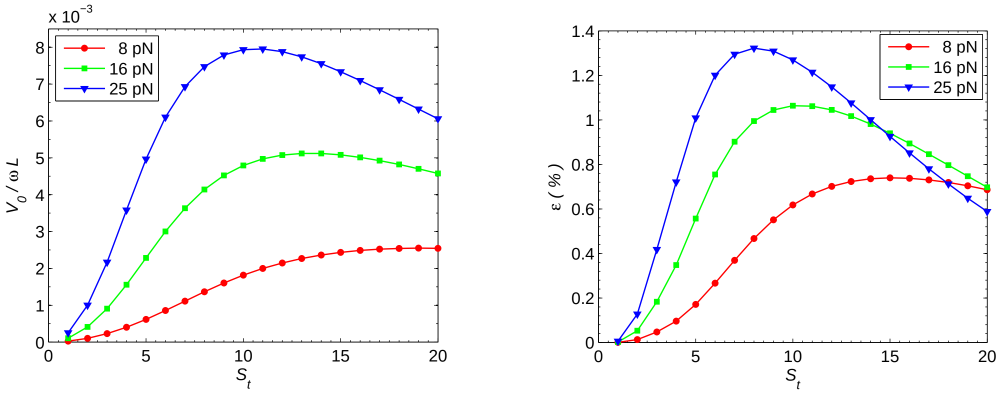

(a) Normalized swimming velocity (b) Propulsion efficiency

Figure 5.4: Swimming velocity and propulsion efficiency as functions of "String sperm number" ($S_t = L/\ell_t$) under same loading condition as in Fig. 5.3 for three different forcing amplitudes F_{y0}.

sequences of typical swimming patterns are shown in Fig. 5.5. A "stiff" micro-string with $T_0 = 159pN$ ($S_t = 2$) shown in Fig. 5.5a has much higher swimming velocity of $V_0 = 34\mu m/s$ than that for the force boundary condition as illustrated in Fig. 5.3a, which is not a surprise because the calculated forcing amplitude $F_{y0} = 54pN$ here is much higher than that in Fig. 5.3a where $F_{y0} = 16pN$; hence much more external work has been done to the micro-string in this case. For a "soft" micro-string shown in Fig. 5.5b with $T_0 = 2.83pN$ ($S_t = 15$), the swimming velocity $V_0 = 21.44\mu m/s$, which is lower than that shown in Fig. 5.5a.

This is again because in order to maintain same Y_0, a smaller forcing amplitude $F_{y0} = 10.5pN$ is needed for the "soft" string with $S_t = 15$ such that a smaller amount of energy is needed than that for the "stiff" string with $S_t = 2$. The corresponding swimming velocity and propulsion efficiency as functions of S_t ($S_t = L/\ell_t$) are shown in Fig. 5.6a and b, respectively. Similar behavior of V_0 and ϵ as functions of (or T_0) have been observed as shown in Fig. 5.4, except that V_0 has much sharper peak here at much smaller value of S_t. Both forcing

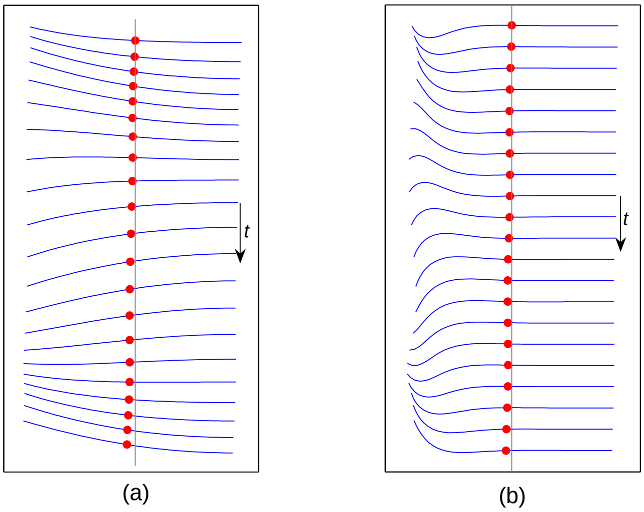

(a) "Stiff" micro-string with $T_0 = 159pN$ ($S_t = 2$)

(b) "Soft" micro-string with $T_0 = 2.8pN$ ($S_t = 15$)

Figure 5.5: Sequences of swimming patterns of a headless micro-string subjected to a point displacement $Y_0 \sin(\omega t)$ at $s = 0$, where $Y_0 = 0.15L$ and $\omega = 2\pi \times 30 rad/s$, at two different T_0. The equal time interval between every two patterns is $\Delta t = 0.002s$. The red dots denote the locations of the midpoint of the filament. For visual reference, the vertical gray lines are aligned with the midpoint of the first(top) swimming pattern.

conditions discussed here are executable in the laboratory experiments through micro-manipulation of optical [57, 71] or magnetic [42, 97] tweezers.

5.3.2 Waveforms of Sperm Flagellar Motion

Now, we use this simple string model to study the swimming motion induced by the sea urchin sperm flagellum [11]. The parameters used in the following simulation - length $L = 50\mu m$, the cross-sectional diameter $d = 200nm$, and viscosity of sea water $\mu = 0.001 N \cdot s/m^2$ - are typical values of the sea urchin sperm flagella. The transverse driving forces, which are considered to be derived from

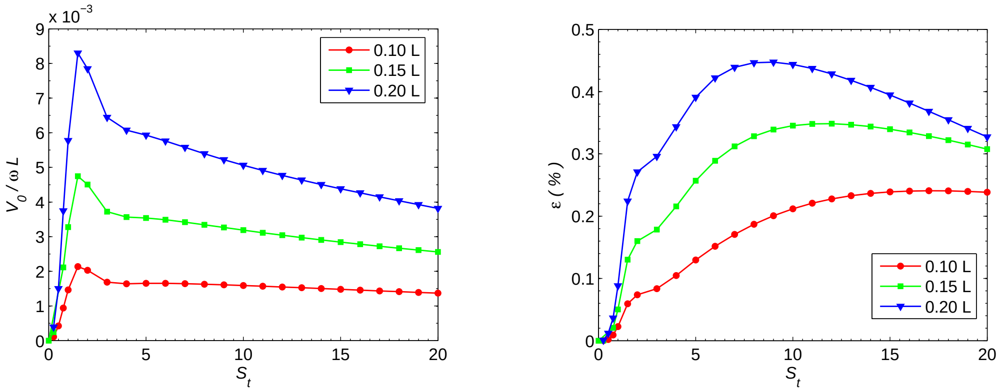

(a) Normalized swimming velocity

(b) Propulsion efficiency

Figure 5.6: Swimming velocity and propulsion efficiency as functions of "String sperm number" ($S_t = L/\ell_t$) under same loading condition as in Fig. 5.5 for three different forcing amplitudes F_{y0}.

the forces generated by the dynein motors when sufficient ATP is presented in the fluid, are taken to be of the form:

$$f_y(s,t) = f_{y0} \cos\left[k\left(s/L - ct\right)\right]. \tag{5.16}$$

In fact, Lowe has introduced a torque quadrupole in the form of a sinusoidal wave [63], which has the same form as $f_y(s,t)$ in Eq. (5.16), in his bending model. In Eq. (5.16), the wave number $k = 3.25\pi$ and beating frequency $f = 35Hz$ are obtained directly from the figure in [11] and partially reproduced in Fig. 5.7b; hence the normalized wave speed $c = 2\pi f/k = 21.5s^{-1}$. The sperm head is modeled by introducing higher anisotropic viscous drag with tangential and normal drag coefficients $\zeta_t = 1.16 \times 10^{-8} N \cdot s/m$ and $\zeta_n = 2\zeta_t = 2.32 \times 10^{-8} N \cdot s/m$. In addition, for simplicity, a pair of two equal-opposite tensile forces T_0 are applied horizontally at $s = 0$ and $s = L$ to simulate the internal tension (repulsive forces, as shown in Fig. 5.1b). The entire flagellum has been divided into $I = 40$ identical segments and the time step $dt = 2\mu s$. The parameters that have not yet been specified are the forcing amplitude f_{y0} and internal tension T_0; these are adjusted during the simulation in order to match the experimentally observed flagellar waveforms.

A series of motion patterns obtained from one simulation at equal time intervals is shown in Fig. 5.7a, clearly indicating that the waveform propagates from left to right, and as a result the sperm swims to the left. A quantitative comparison of our predictions with Brokaw's experimental observations is shown in Fig. 5.7b. The highlighted waveforms from Fig. 5.7a are superimposed in Fig. 5.7b. The unspecified parameters in the simulation (the tension and transverse driving force) were selected in order to obtain a good matching between the simulations and experiments: $T_0 = 6.13pN$ and $f_{y0} = 1.97pN/\mu m$; these values are of the correct order of magnitude for typical forces that can be generated by the dynein motors and other molecular interactions. The predicted swimming speed calculated from the simulation is $V_0 = 126.6\mu m/s$, which is slightly lower than the value $V_0 \sim 150\mu m/s$ estimated directly from the figures of Brokaw [11]. Most notably, in contrast to previous models, the predicted flagellar motion shows excellent quantitative agreement with the experimental observations.

Woolley and Vernon [95] showed that when the fluid viscosity is increased to $\mu = 4N \cdot s/m^2$ (by more than 3 orders of magnitude from that of artificial sea water), sea urchin sperm still manages to propel itself, albeit at a much lower speed, with a much different wave form (shown in Fig. 5.8a). The prediction of the string model for this case is obtained quite easily by varying the "string sperm number" S_t and transverse force f_{y0} until the predicted motion pattern (shown in Fig. 5.8b) exhibits the short wave mode observed experimentally; quantitative matching is not easy to accomplish in this instance since the initial patterns

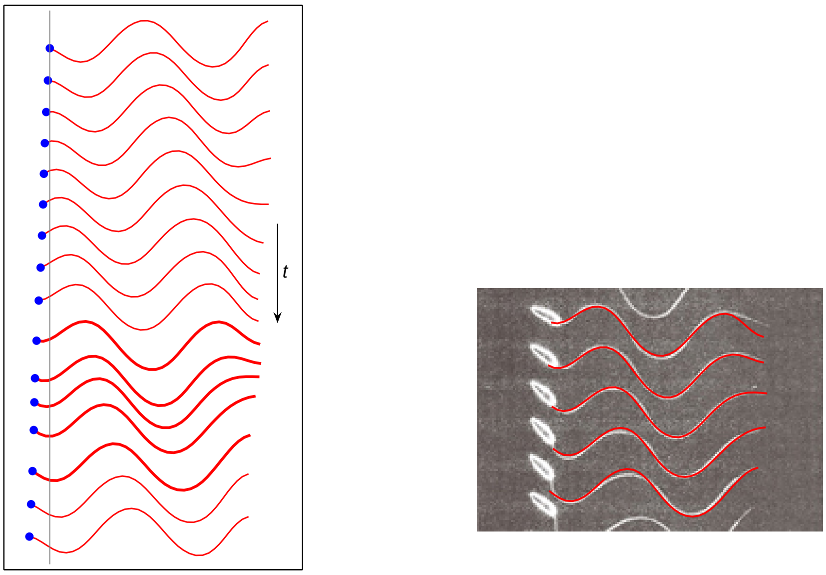

(a) (b)

Figure 5.7: Comparison of the swimming patterns between the simulation results and the sperm flagellar waveforms. The driving force $f_y(s,t) = f_{y0}\cos\left[k\left(s/L - ct\right)\right]$ with $f_{y0} = 1.97pN/\mu m$, $k = 3.25\pi$, $L = 50\mu m$ and $kc = 2\pi \times 35rad/s$. The blue solid circle represents the sperm head. (a) Sequence of the simulated swimming patterns (The vertical spacing proportionally corresponds to the time interval); (b) Superposition of the a series of simulation results on the experimentally observed flagellar waveforms (Courtesy of Charles Brokaw, in [11])

and other factors may affect their beating shapes, but it is easily observed that the predictions are quite similar to the observations [95] in terms of the wave length and amplitude. The parameters that resulted in the appropriate short wavelength mode shapes are $S_t = 15.8$ or $T_0 = 1nN$, and $f_{y0} = 1.2nN/\mu m$, which are achievable when most of the dynein motors in the flagellum are activated simultaneously. The swimming velocity obtained in the simulation $V_0 = 7.8\mu m/s$ is to be compared with the experimental observation of $V_0 = 9.94 \pm 3.44\mu m/s$ [95]. Note that the tension and transverse forces in this case are roughly three orders of magnitude larger than in artificial sea water; this, of course, is to be expected

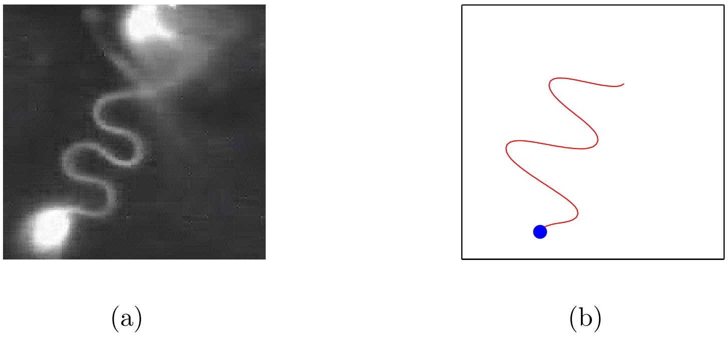
(a) (b)

Figure 5.8: Comparison of the swimming patterns between simulation and experiment for the sperm swims in the artificial sea water with very high viscosity. (a) High curvature of the flagellar swimming in artificial sea water with methylcellulose added to increase the viscosity ($\mu = 4N \cdot s/m^2$) (image reproduced from the supporting materials of ref [95] on Woolley's Website: http://www.bris.ac.uk/Depts/Physiology/Staff/DW/movies.htm); (b) Simulation of the swimming pattern in (a) with $\mu = 4N \cdot s/m^2$, $f_{y0} = 1.2nN/\mu m$ and $T_0 = 1nN$.

since the viscous load on the flagellum is also high. Clearly, using the tension model we have captured the essence of flagellar propulsion.

In order to explore the string model further, we fix the values of all parameters, and determine the variation of the swimming velocity with tension T_0 (equivalently, S_t); this variation is shown in Fig. 5.9 for a forcing amplitude $f_{y0} = 2.15pN/\mu m$, which was chosen in order to match most of the available experimental data for sperm in normal sea water. This diagram represents the dynamic scaling of the motion of sperm in a viscous environment. In order to demonstrate the power of this scaling, we present a comparison with experimental observations on the motion of spermatozoa; we collected data from the literature regarding parameters of sperm movements in different species as summarized in Table 5.1. In order to plot these data in Fig. 5.9, it was assumed that the tension - the quantity that is not measured in experiments - was equal to the one that was obtained in fitting to Brokaw's mode shapes in Fig. 5.7b ($T_0 = 6.13pN$) for the sperm in normal sea water; in other words, we assumed that the internal structural and force generation characteristics of the flagella are species independent. For the case of high viscosity swimming, the parameters obtained by matching the simulations to experimental shapes were used.

Table 5.1: Experimental data on various species of sperm

Sperm species[a]	L (μm)	f (Hz)	f_s (Hz)	V_0 ($\mu m/s$)	μ (Ns/m^2)	$V_0/\omega L$	S_t	Ref.
Sea urchin	50	35	400	150	0.001	0.0136	13.39	[11]
Ovis (ram)	59	29.2	300 – 350	135.8	0.001	0.0125	14.44	[30]
Ostrea (oyster)	47	43.1	400	163.8	0.001	0.0129	13.97	[30]
Colobocentrotus[b]	42	32	?	90	0.001	0.0107	10.76	[19,36]
Colobocentrotus[c]	42	46	?	160	0.001	0.0132	12.90	[19,36]
Tenebrio (2D?)	52	28	?	100	0.001	0.0109	12.46	[3]
Psammechinum	45	35	30 – 40	190	0.001	0.0192	12.05	[44,45]
Ciona (tunicate)	47.5	35	30 – 40	165	0.0014	0.0158	15.05	[13,19]
Chaetopterus	36	26.5	20 – 40	105	0.0014	0.0175	9.93	[13,19]
Lytechinus	43.5	30	30 – 50	158	0.0014	0.0193	12.76	[13,19]
Echinus esculentus	42	50	50	200	0.001	0.0152	13.45	[95]
Echinus esculentus	42	3.80	50	14.89	1.5	0.0148	16.76	[95]
Echinus esculentus	42	2.81	50	9.94	4	0.0134	15.78	[95]

---

[a] L: flagellar length; $f = \omega/2\pi$: beating frequency; f_s: sampling frequency; V_0: swimming velocity; μ: fluid viscosity. S_t is calculated with $T_0 = 450pN$ for Echinus esculentus with $\mu = 1.5Ns/m^2$, $T_0 = 1000pN$ for $\mu = 4Ns/m^2$ and $T_0 = 6.13pN$ for all other cases, which were obtained from the above simulations.

[b] Reactivated with $1mM$ ATP at $25°C$

[c] Live sperm in sea water

It is clear that all experimental observations when scaled with the "string sperm number" fall within range of the predictions from the string model, with most data points in good agreement with the simulation; much of the scatter in the experiments could be attributed to uncertainties in measuring the parameters of swimming. However, there are a few data points that are quite far away from

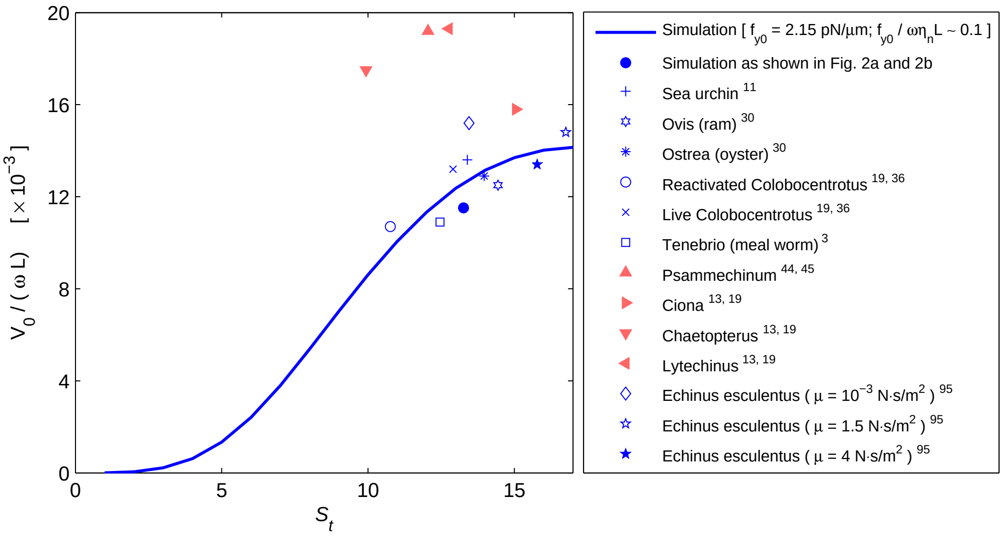

Figure 5.9: Dependence of normalized swimming velocity on “string sperm number” S_t, along with a comparison to the published data on eukaryotic sperms.

the predictions of the string model (with the normalized swimming speed in the range of 0.02); these are plotted with faded-symbols since we estimate that there are greater experimental uncertainties with these results[1].

5.3.3 Comparison With Bending Model

For the bending model, the elasticity of the micro-filament has two contributions: bending and axial forces, thus the governing equation can be written as Eq. (4.1). After linearization for the small-amplitude motion, equation (4.1) becomes

$$\eta_n \dot{Y} + A_0 Y'''' - T_0 Y'' = f_y. \tag{5.17}$$

---

[1] These appear to be significantly faster in comparison to the sperm of similar characteristics, but it is not clear why these data are outside of the trend.

Furthermore, we normalize Eq. (5.17) by setting $\hat{Y} = Y/L$, $\hat{s} = s/L$, $\hat{t} = \omega t$, and $\hat{f}_y = f_y/\left(\omega \eta_n L\right)$, then equation (5.17) can be rewritten as

$$\frac{\partial \hat{Y}}{\partial \hat{t}} + \frac{1}{S_p^4} \frac{\partial^4 \hat{Y}}{\partial \hat{s}^4} - \frac{1}{S_t^2} \frac{\partial^2 \hat{Y}}{\partial \hat{s}^2} = \hat{f}_y. \tag{5.18}$$

with the definitions, “sperm number” $S_p = L/\left(A_0/\omega \eta_n\right)^{1/4}$ [63] and “string sperm number” S_t in Eq. (5.8). Two limiting cases can be identified: (i) for $A_0 \gg T_0^2/\omega \eta_n$, i.e. tension can be ignored, compared to the bending force, equation (5.18) reduces to the previous beam model and solutions have already been studied as well [20, 21, 63, 91, 92]; (ii) for $A_0 \ll T_0^2/\omega \eta_n$, i.e. tension dominates the filament elasticity, then the problem reduces to string model, which has been examined in previous sections. The linearized equations of both model possess wave-propagating solutions, which breaks the time-reversal symmetry and thus generate the net force necessary for propulsion. For quantitative comparison between beam model and string model, we perform numerical simulations of the nonlinear governing equations (4.1) and (5.4), respectively, for two different cases. First, we consider the oscillatory force $F_{y0}\cos(\omega t)$ applied at one end ($s = 0$); then, we compare simulations of both models to the sperm flagellar motion.

By demanding $S_t = S_p$, we end up with the equivalent relation between bending stiffness and tension as $A_0 = T_0^2/\omega \eta_n$. By varying bending stiffness A_0 (setting $T_0 = 0$) in the bending model and T_0 (setting $A_0 = 0$) in the string model, respectively, to ascertain $S_t = S_p$, two sets of simulations have been performed, with a harmonic force $F_{y0}\cos(\omega t)$ applied at the point $s = 0$. Figure 5.10 shows the comparison of swimming patterns for two models. It can be observed from this figure that the response in terms of the swimming patterns of both models is qualitatively quite similar and that there are only minor quantitative differences.

In fact, the swimming velocities of the micro-filament with $S_p = 3$ and its equivalent micro-string are $V_0 = 14.5\mu m/s$ and $V_0 = 16.3\mu m/s$ respectively. Similarly, for $S_p = S_t = 10$, the swimming velocity of the micro-filament and its equivalent micro-string are $V_0 = 57.0\mu m/s$ and $V_0 = 59.8\mu m/s$ respectively. However, there are major differences in the efficiency of propulsion. Comparisons of swimming velocity and propulsion efficiency between the two different models are plotted in Fig. 5.11. The trends of both swimming velocity and propulsion efficiency

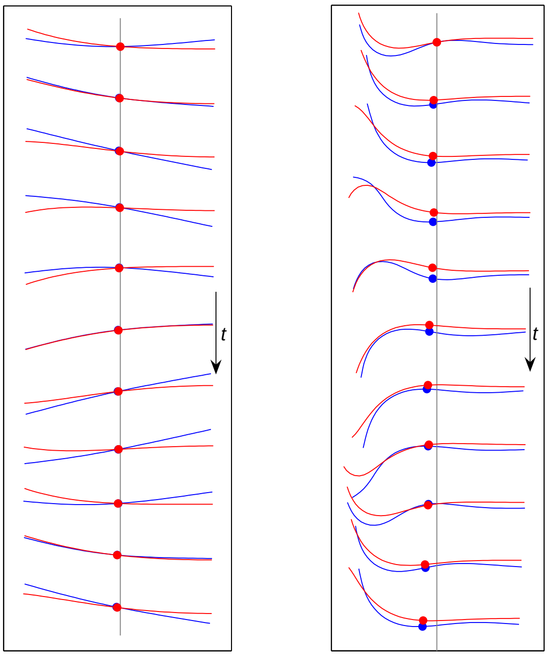

(a) "Stiff" micro-string or filament with $S_t = S_p = 3$

(b) "Soft" micro-string or filament with $S_t = S_p = 10$

Figure 5.10: Comparison of the swimming patterns between the string model and its equivalent beam model. The driving force $F_{y0}\cos(\omega t)$ applied at $s = 0$ with $F_{y0} = 25pN$, and $\omega = 2\pi \times 30rad/s$. Red: string, Blue: filament. The equal time interval between every two patterns is $\Delta t = 0.004s$. The red dots denote the locations of the midpoint of the filament. For visual reference, the vertical gray lines are aligned with the midpoint of the first(top) swimming pattern.

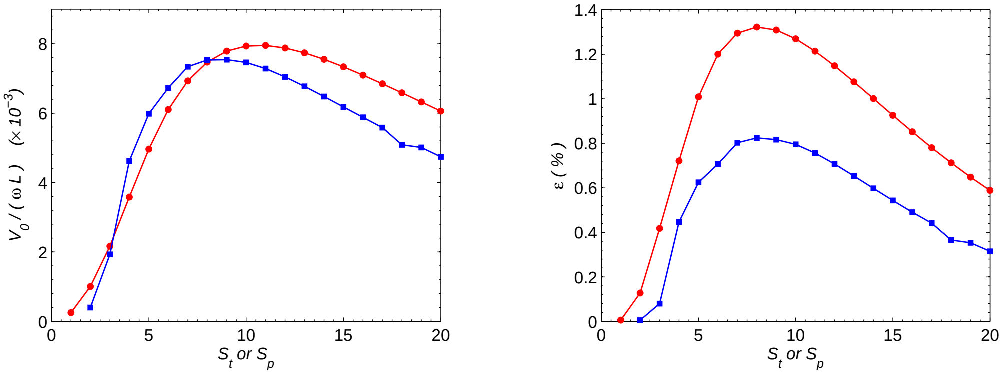

(a) Normalized swimming velocity (b) Propulsion efficiency

Figure 5.11: Comparisons of swimming velocity and propulsion efficiency between two different models for same effective bending stiffness A_n, string ($A_n = T_0^2/\omega\eta_n$) and rod ($A_n = A_0$), under same boundary condition as in Fig. 5.10. Red: string, Blue: filament.

as functions of S_p (S_t) is similar to that discussed previously in Section 5.3.1 for the string model. But an important observation arising from the present simulations is that while both the string and the bending model provide comparable propulsive speed at corresponding S_p (S_t), the string model has a higher propulsion efficiency than its equivalent bending model. This is a very useful concept in the design of the artificial micro-swimmers: one should make the micro-filament with as low bending stiffness as possible and then by controlling the tension in situ during its motion, gain higher propulsion efficiency and while still obtaining favorable velocities as shown in Fig. 5.11.

Second, we compare the simulation results of bending model to the experimental flagellar waveforms, as shown in Fig. 5.12. The bending stiffness of the flagellum is taken to be $A_0 = 4 \times 10^{-22}$ [21, 50]. For the same forcing amplitude used in the string model, $f_{y0} = 1.97 pN/\mu m$, the motion patterns of bending model are far away from the experimental pattern as can be seen from Fig. 5.12a. If

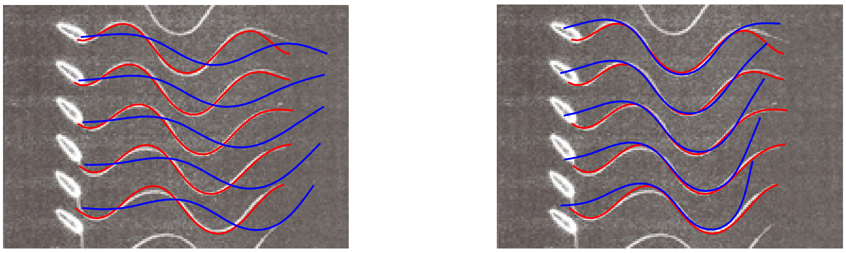

(a) $f_{y0} = 1.97pN/\mu m$ same as that in Fig. 5.7

(b) $f_{y0} = 4.00pN/\mu m$

Figure 5.12: Comparison of the swimming patterns between the bending models (blue curves) and the experimentally observed sperm flagellar waveforms (Courtesy of Charles Brokaw, picture in [11]) for two different sets of parameters. Same type of driving force has used as that in Fig. 5.7. In both cases, the sperm head was modeled by anisotropic drag: $\zeta_t = 1.16 \times 10^{-8} N \cdot s/m$ and $\zeta_n = 2.32 \times 10^{-8} N \cdot s/m$

the forcing amplitude is doubled to $f_{y0} = 4pN/\mu m$, the bending model is able to capture the central part of the motion shape relatively well (as shown in Fig. 5.12b.), but not nearly as completely as the string model does, particularly, near the sperm head and the tail. The calculated swimming velocity corresponding to Fig. 5.12a and b are $V_0 = 57.6\mu m/s$ and $V_0 = 125.1\mu m/s$ respectively; the latter estimate is comparable to the velocity $V_0 = 126.6\mu m/s$ obtained with the string model. Perhaps a better match of the shape is possible, but this requires that the bending stiffness be one or two orders of magnitude smaller than reported value $A_0 = 4 \times 10^{-22}$ [21, 50]. As a quick estimate of this, we consider the curve of the waveform near the sperm head: the local curvature in this range is $\kappa \approx 1/4\mu m^{-1}$ (as shown in Fig. 5.12), so that the required bending moment at this region is $M = A_0\kappa \approx 10^2 pN \cdot \mu m$; this is just the elastic bending moment and ignores the viscous load completely. Even so, this is much greater than what the dynein motors can supply (a pair of dynein motors generating $5pN$ across the flagellum separated by about $0.20\mu m$ can generate a bending moment of about $1pN \cdot \mu m$). For the flagellum with $9 + 2$ structure, the resultant bending moment on each cross-section will become even smaller. For further illustration of this, Fig. 5.13a and b show the flagellar waveforms at two different viscosity taken from [95]; their curvatures has been estimated as shown in the figure. The maximum curvature for the flagellum in normal sea water ($\mu = 10^{-3} N \cdot s/m^2$, Fig. 5.13a) is $\kappa \approx 0.3\mu m^{-1}$. On the other hand, $\kappa \approx 1\mu m^{-1}$ for the flagellum in the artificial sea water ($\mu = 1.5N \cdot s/m^2$, Fig. 5.13b). The maximum elastic bending moments in these two cases are $M \approx 120$ and $600pN \cdot \mu m$, which are again much greater than what the dynein motors can supply. Such curvatures are possible, again if the bending stiffness is one to two orders of magnitude smaller than reported values; the main inference that we derive from these estimates is that the model based on tension is better able to replicate observed flagellar waveforms and propulsive speeds.

With the results of the string and beam models as discussed above, we believe that the tension model is more appropriate than bending model for flagellar motion. Our study shows that tension can indeed play a crucial role in flagellar motion. Excellent agreement between the simulation and experimental observations suggests that simple string model is sufficient to capture the fundamental physics behind the sperm flagellar motion; the string model appears to reproduce observed behavior so completely, that we are tempted to make some conjectures regarding the possibility that tension in the flagella may indeed be an actual possibility rather than a convenient model abstraction. Although direct experimental observations on the sliding of doublet microtubules during the flagellar bending have been reported [16, 17], there is no easy way to ascertain whether bending is

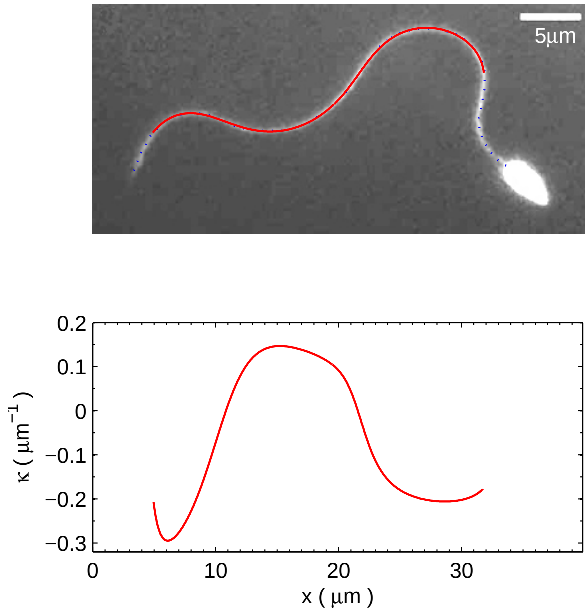

(a) Normal sea water ($\mu = 10^{-3} N \cdot s/m^2$). The measured length: $L \approx 45 \mu m$

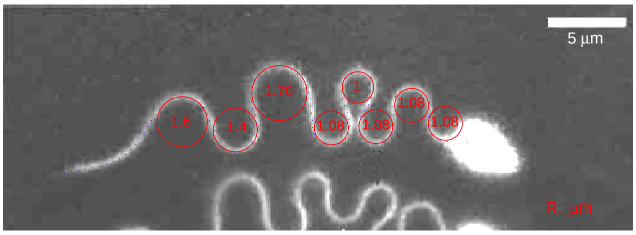

(b) Artificial sea water with very high viscosity ($\mu = 1.5 N \cdot s/m^2$). The measured length: $L \approx 51 \mu m$

Figure 5.13: Waveforms and curvature estimation of the swimming flagella at two different viscosities [95].

caused by the relative sliding of doublet microtubules or the sliding results from the flagellar curvature. Can the tension T_0 and its fluctuations with time arise from the repulsive interaction of dynein heads, radial spokes or from the oscillating interaction of dynein with the microtubules [82]?

5.4 Summary

Low-Reynolds number dynamics of a micro-string has been studied theoretically and numerically, which is able to capture the underpinning physics of the microscopic one-armed swimmers. Bending elasticity may quantitatively alter the swimming patterns, swimming velocity, and propulsion efficiency as well, but not essentially change the swimming of such filaments. Comparison with the bending model has demonstrated that, for the same equivalent “bending stiffness”, the micro-string has a higher propulsion efficiency. This may serve as one of the guidelines in the fabrication of such kind of swimmer as long as the propulsion efficiency is an important concern.

Excellent agreement between the predictions of the string model and flagellar motion has been obtained, indicating that (i) the simple string model is capable of capturing the essential underlying physics of sperm flagellar swimming; (ii) tension plays a crucial role in the sperm flagellar motion. Our model has been restricted to 2D planar motion, future studies can be carried on the 3D helical motion and 2D to 3D transition, which has been observed in the motion of the eukaryotic sperm flagella when the fluid viscosity changes [95].

Chapter 6

Conclusions

Dynamic response of strings and filaments in two different regimes - inertial and low-Reynolds number - has been studied. For the string and filament in the inertial field, free motion as well as forced motion exists. On the other hand, for the microscopic one-armed swimmers in the viscous environment, free motion does not exist due to the viscous dissipation. Hence, an energy source - provided by the dynein proteins interacting with the ATP for sperm flagella or generated optically or magnetically for the artificial swimmers - is needed for such swimmers to maintain their motion.

In the first part of the thesis, we have studied the dynamic response of the perfectly flexible string and thin filament in the inertial regime through theoretical, numerical and experimental efforts. An array of rich dynamics has been observed experimentally: steady-state resonant response, steady-state motion with multiple periodicities, and non-steady chaotic motion for the rotary excitation; planar stable oscillation, 3D steady whirling motion, and 2D to 3D transition for planar harmonic excitation.

In the second part, the low-Reynolds number dynamics of the micro-strings and micro-filaments has been investigated. Tension (repulsive force), which can be generated optically or magnetically for the artificial micro-swimmers or by the interaction between the dynein proteins and the ATP for the natural micro-swimmers (eukaryotic sperm flagella), has been shown to be comparable to or dominate the bending elastic force for these swimmers. The equivalent relation between bending elasticity and tension elasticity has been constructed. Competition between tension and bending has also be identified. A tunable microscopic one-armed swimmer has been constructed theoretically, which can be easily realized in the laboratory micro-manipulation utilizing optical or magnetic tweezers. Finally, we studied the propulsion induced by the sperm flagella using the simple string model. Excellent agreement between the simulation results and experimentally observed flagellar waveforms indicates that simple string model is able to capture the underlying physics of the flagellar motion and that tension plays a crucial role in their motion.

Finally, our study on the dynamics of micro-string and micro-filaments at low Reynolds number has been restricted to two-dimensions. Fully three-dimensional study in the future may provide new features and explain the planar to helical transition, which has been observed in the flagellar motion when the extreme condition (extremely high viscosity of the solvent) is applied [95]. On the other hand, future experimental work can be done on the tunable micro-swimmer that has been constructed theoretically in this work.

Appendices

Appendix A

Calculation of $T(s,t)$ in Numerical Simulation

The calculation of $T(s,t)$ in our numerical scheme in Chapter 4 and 5 is performed through the constraint dynamics, which is widely used to calculate the constraint forces in molecular dynamics simulation of polyatomic systems [1].

First, the inextensibility condition can be expressed in terms of each segment in the numerical discretization as

$$\left|\mathbf{r}_{i(i+1)}^{n+1}\right|^2 - ds^2 = 0 \tag{A.1}$$

where i represents the spatial nodal number, n represents time step, and

$$\mathbf{r}_{i(i+1)}^{n+1} = \mathbf{r}_{i+1}^{n+1} - \mathbf{r}_{i}^{n+1}, \tag{A.2}$$

$$\begin{aligned}\mathbf{r}_{i(i+1)}^{n+1} = (\mathbf{r_b})_{i(i+1)}^{n+1} \quad & +dt\left(\eta^{-1}\right)_{i+1}^{n} \tfrac{1}{ds^2}\left[T_{i+1}^{n}\mathbf{r}_{(i+1)(i+2)}^{n} - T_{i}^{n}\mathbf{r}_{i(i+1)}^{n}\right] \\ & -dt\left(\eta^{-1}\right)_{i}^{n} \tfrac{1}{ds^2}\left[T_{i}^{n}\mathbf{r}_{(i)(i+1)}^{n} - T_{i-1}^{n}\mathbf{r}_{(i-1)i}^{n}\right],\end{aligned} \tag{A.3}$$

$$(\mathbf{r_b})_i^{n+1} = \begin{cases} \mathbf{r}_i^n + dt\left(\eta^{-1}\right)_i^n \mathbf{f}_i^n\ , & string \\ \mathbf{r}_i^n + dt\left(\eta^{-1}\right)_i^n \left[-A_0\left(\kappa'\hat{\mathbf{n}}\right)' + \mathbf{f}\right]_i^n\ , & filament \end{cases} . \tag{A.4}$$

Second, to the first order approximation, equation A.1 can be written as a system of I linear algebraic equations for all the I segments, i.e.

$$\mathbf{A}\mathbf{T} = \mathbf{B}, \tag{A.5}$$

in which $\mathbf{A}$ is a $I \times I$ matrix and $\mathbf{B}$ is a $I \times 1$ vector; $\mathbf{T}$ is a $I \times 1$ vector that are to be determined. Specifically,

$$\begin{cases} \mathbf{A}_{i(i-1)} = (\mathbf{r_b})^{n+1}_{i(i+1)} \left(\eta^{-1}\right)^n_i \mathbf{r}^n_{(i-1)i} \ , \quad i = 2, 3, ...I \\ \\ \mathbf{A}_{ii} = -\left(\mathbf{r_b}\right)^{n+1}_{i(i+1)} \left[\left(\left(\eta^{-1}\right)^n_i + \left(\eta^{-1}\right)^n_{i+1}\right) \mathbf{r}^n_{i(i+1)}\right] \ , \quad i = 1, 2, ...I \\ \\ \mathbf{A}_{i(i+1)} = (\mathbf{r_b})^{n+1}_{i(i+1)} \left(\eta^{-1}\right)^n_{i+1} \mathbf{r}^n_{(i+1)(i+2)} \ , \quad i = 1, 2, ...I - 1 \\ \\ \mathbf{A}_{ij} = 0 \ , \quad otherwise \end{cases} \tag{A.6}$$

and

$$\mathbf{B}_i = \frac{ds^2}{2dt} \left[ds^2 - \left|(\mathbf{r_b})^{n+1}_{i(i+1)}\right|^2\right] \ , \quad i = 1, 2, ...I. \tag{A.7}$$

Finally, $\mathbf{T}^n_i$ ($i = 1, 2, ...I$ and $n = 1, 2, ...$) can be obtained by solving Eq. A.5.

Bibliography

[1] M.P. Allen and D.J. Tildesley. *Computer simulation of liquids.* Oxford University Press, Oxford, 1987.

[2] S.S. Antman and M. Reeken. The drawing and whirling of strings: Singular global multiparameter bifurcation problems. *SIAM J. Math. Anal.*, 18:337–365, 1987.

[3] B. Baccetti, F. Bernini, E. Bigliardi, A.G. Burrini, R. Dallai, F. Giusti, M. Mazzini, V. Pallini, T. Renieri, F. Rosati, G. Selmi, and M. Vegni. Motility patterns in sperms with different tail structure. *The Functional Anatomy of the spermatozoon, ed. B.A. Afzelius*, pages 141–150, 1975.

[4] L.E. Becker, S.A. Koehler, and H.A. Stone. On self-propulsion of micromachnies at low reynolds number: Purcell's three-link swimmer. *J. Fluid Mech.*, 490:15–35, 2003.

[5] C.M. Bender and S.A. Orzag. *Advanced Mathematical Methods for Scientists and Engineers.* New York: McGraw-Hill, 1978.

[6] H.C. Berg. The rotary motor of bacterial flagella. *Annu. Rev. Biochem.*, 72:19–54, 2003.

[7] H.C. Berg and R.A. Anderson. Bacteria swim by rotating their flagellar filaments. *Nature (London)*, 245:380–384, 1973.

[8] S.L. Biswal and A.P. Gast. Rotational dynamics of semiflexible paramagnetic particle chains. *Phys. Rev. E*, 69:041406, 2004.

[9] J.Y. Bouguet. *http : //www.vision.caltech.edu/bouguetj/calib–doc/index.html. accessed on August 30, 2003.*

[10] J.Y. Bouguet and P. Perona. 3D photography using shadows in dual-space geometry. *Int. J. Comput. Vision*, 35:129–149, 1999.

[11] D. Bray. *Cell Movements. From Molecules to Motility.* Garland Publishing, New York, 2001.

[12] C. Brennen and H. Winet. Fluid mechanics of propulsion by cilia and flagella. *Ann. Rev. Fluid Mech.*, 9:339–398, 1977.

[13] C.J. Brokaw. Non-sinusoidal bending waves of sperm flagella. *J. Exp. Biol.*, 43:155–169, 1965.

[14] C.J. Brokaw. Computer simulation of flagellar movement. i. demonstration of stable bend propagation and bend initiation by the sliding filament model. *Biophys. J.*, 12:564–586, 1972.

[15] C.J. Brokaw. Flagellar movement: a sliding filament model. *Science*, 178:455–462, 1972.

[16] C.J. Brokaw. Direct measurements of sliding between outer doublet microtubules in swimming sperm flagella. *Science*, 243:1593–1596, 1989.

[17] C.J. Brokaw. Microtubule sliding in swimming sperm flagella: direct and indirect measurements on sea urchin and tunicate spermatozoa. *J. Cell Biol.*, 114:1201–1215, 1991.

[18] C.J. Brokaw. Simulating the effects of fluid viscosity on the behaviour of sperm flagella. *Math. Meth. Appl. Sci.*, 24:1351–1365, 2001.

[19] C.J. Brokaw and I.R. Gibbons. Mechanisms of movement in flagella and cilia. *Swimming and Flying in Nature*, I:89–132, 1975.

[20] S. Camalet and F. Julicher. Generic aspects of axonemal beating. *New J. Phys.*, 2:24.1–24.23, 2000.

[21] S. Camalet, F. Julicher, and J. Prost. Self-organized beating and swimming of internally driven filaments. *Phys. Rev. Lett.*, 82:1590–1593, 1999.

[22] G.F. Carrier. On the non-linear vibration problem of the elastic string. *Q. Appl. Math.*, 3:157–165, 1945.

[23] T.K. Caughey. Whirling of a heavy chain. *P. 3rd US Natl. Congr. Appl. Mech.*, pages 101–108, 1958.

[24] T.K. Caughey. Whirling of a heavy string under constant axial tension: A non-linear eigenvalue problem. *Int. J. Nonlinear Mech.*, 4:61–75, 1969.

[25] S. Childress. *Mechanics of Swimming and Flying.* Cambridge University Press, Cambridge, 1981.

[26] J. Clark, W.B. Fraser, C. Rahn, and A. Rajamani. Limit-cycle oscillations of a heavy whirling cable subject to aerodynamic drag. *P. Roy. Soc. A-Math. Phy.*, 461:875–893, 2005.

[27] J. Coomer, M. Lazarus, R.W. Ticker, D. Kershaw, and A. Tegman. A non-linear eigenvalue problem associated with inextensible whirling strings. *J. Sound Vib.*, 239:969–982, 2001.

[28] J. Cosson. A moving image of flagella: news and views on the mechanisms involved in axonemal beating. *Cell Biol. Int.*, 20:83–94, 1996.

[29] R.G. Cox. The motion of long slender bodies in a viscous fluid part 1. general theory. *J. Fluid Mech.*, 44:791–810, 1970.

[30] M.A. Denehy. The propulsion of nonrotating ram and oyster spermatozoa. *Biol. Reprod.*, 13:17–29, 1975.

[31] E. H. Dill. Kirchhoff's theory of rods. *Arch. Hist. Exact Sci.*, 44:1–23, 1992.

[32] M. Dogterom and B. Yurke. Measurement of the force-velocity relation for growing microtubules. *Science*, 278:856–860, 1997.

[33] R. Dreyfus, J. Baudry, M.L. Roper, M. Fermigier, H.A. Stone, and J. Bibette. Microscopic artificial swimmers. *Nature (London)*, 437:862–865, 2005.

[34] R.S. Figliola and D.E. Beasley. *Theory and Design for Mechanical Measurement.* John Wiley and Sons, Inc. New York, 2000.

[35] E. Gauger and H. Stark. Numerical study of a microscopic artificial swimmer. *Phys. Rev. E*, 74:021907, 2006.

[36] B.H. Gibbons and I.R. Gibbons. Flagellar movement and adenosine triphosphatase activity in sea urchin sperm extracted with triton $x - 100$. *J. cell Biol.*, 54:75–97, 1972.

[37] F. Gittes, J. Nettleton B. Mickey, and J. Howard. Flexural rigidity of microtubules and actin filaments measured from thermal fluctuations in shape. *J. Cell Biol.*, 120:923–934, 1993.

[38] A. Goriely and M. Tabor. Nonlinear dynamics of filaments - i. dynamical instabilities. *Physica D*, 105:20–44, 1997.

[39] A. Goriely and M. Tabor. Nonlinear dynamics of filaments - ii. nonlinear analysis. *Physica D*, 105:45–61, 1997.

[40] A. Goriely and M. Tabor. Nonlinear dynamics of filaments - iii instabilities of helical rods. *P. Roy. Soc. Lond. A Mat.*, 453:2583–2601, 1997.

[41] A. Goriely and M. Tabor. The nonlinear dynamics of filaments. *Nonlinear Dynam.*, 21:101–133, 2000.

[42] C. Gosse and V. Corquette. Magnetic tweezers: micromanipulation and force measurement at the molecular level. *Biophys. J.*, 82:3314–3329, 2002.

[43] C. Goubault, P. Jop, M. Fermigier, J. Baudry, E. Bertrand, and J. Bibette. Flexible magnetic filaments as micromechanical sensors. *Phys. Rev. Lett.*, 91:260802, 2003.

[44] J. Gray. The movement of sea-urchin spermatozoa. *J. Exp. Biol.*, 32:775–801, 1955.

[45] J. Gray and G.J. Hancock. The propulsion of sea-urchin spermatozoa. *J. Exp. Biol.*, 32:802–814, 1955.

[46] G.J. Hancock. The self-propulsion of microscopic organisms through liquids. *Proc. R. Soc. Lond. A*, 217:96–121, 1953.

[47] H. Harrison. Plane and circular motion of a string. *J. Acoust. Soc. Am.*, 20:874–875, 1948.

[48] J.D. Helm, S.R. McNeil, and M.A. Sutton. Improved three-dimensional image correlation for surface displacement measurement. *Opt. Eng.*, 35:1911–1920, 1996.

[49] C.T. Howell and M.S. Triantafyllou. Stable and unstable nonlinear resonant response of hanging chains: theory and experiment. *P. Roy. Soc. A-Math. Phy.*, 440:345–364, 1993.

[50] S. Ishijima and Y. Hiramoto. Flexural rigidity of echinoderm sperm flagella. *Cell Struct. Fun.*, 19:349–362, 1994.

[51] J. Israelachvili and H. Wennerstrom. Role of hydration and water structure in biological and colloidal interactions. *Nature (London)*, 379:219–225, 1996.

[52] M.E. Janson and M. Dogterom. A bending mode analysis for growing microtubules: Evidence for a velocity-dependent rigidity. *Biophys. J.*, 87:2723–2736, 2004.

[53] M.E. Janson and M. Dogterom. Scaling of microtubule force-velocity curves obtained at different tubulin concentrations. *Phys. Rev. Lett.*, 92:248101, 2004.

[54] J.B. Keller and S.I. Rubinow. Slender-body theory for slow viscous fluid. *J. Fluid Mech.*, 75:705–714, 1976.

[55] I.I. Kolodner. Heavy rotating string - a nonlinear eigenvalue problem. *Commun. Pure Appl. Math.*, 3:395–408, 1955.

[56] L.D. Landau and E.M. Lifshitz. *Theory of Elasticity.* Butterworth-Heinemann, Oxford, 3rd Edition, 1986.

[57] M.J. Lang and S.M. Block. Resource letter: Lbot-1: Laser-based optical tweezers. *Am. J. Phys.*, 71:201–215, 2003.

[58] G. Lemon and W.B. Fraser. Steady-state bifurcations and dynamical stability of a heavy whirling cable acted on by aerodynamic drag. *P. Roy. Soc. A-Math. Phy.*, 457:1021–1041, 2001.

[59] C.B. Lindemann and K.S. Kanous. A model for flagellar motility. *Int. Rev. Cytol*, 173:1–72, 1997.

[60] C.B. Lindemann, W.G. Rudd, and R. Rikmenspoel. The stiffness of the flagella of impaled bull sperm. *Biophys. J.*, 13:437–448, 1973.

[61] H. Lodish, D. Baltimore, A. Berk, S.L. Zipursky, P. Matsudaira, and J. Darnell. *Molecular Cell Biology.* W.H. Freeman and Company, New York, 1995.

[62] A.E.H. Love. *A Treatise on the Mathematical Theory of Elasticity.* Dover Publications, New York, 4th Edition, 1927.

[63] C.P. Lowe. Dynamics of filaments: modelling the dynamics of driven microfilaments. *Philos. Trans. R. Soc. London B*, 358:1543–1550, 2003.

[64] K.E. Machin. Wave propagation along flagella. *J. Exp. Biol.*, 35:796–806, 1958.

[65] M. Manghi, X. Schlagberger, and R.R. Netz. Propulsion with a rotating elastic nanorod. *Phys. Rev. Lett.*, 96:068101, 2006.

[66] J. Miles. Resonant, nonplanar motion of a stretched string. *J. Acoust. Soc. Am.*, 75:1505–1510, 1984.

[67] G.S.S. Murthy and B.S. Ramakrishna. Nonlinear character of resonance in stretched strings. *J. Acoust. Soc. Am.*, 38:461–471, 1965.

[68] R. Narasimha. Non-linear vibration of an elastic string. *J. Sound Vib.*, 8:134–146, 1968.

[69] A.H. Nayfeh and D.T. Mook. *Nonlinear Oscillations.* New York: John Wiley, 1979.

[70] S.A. Nayfeh, A.H. Nayfeh, and D.T.Mook. Nonlinear response of a taut string to longitudinal and transverse end excitation. *J. Vib. Control*, 1:203–207, 1995.

[71] K.C. Neuman and S.M. Block. Optical trapping. *Rev. Sci. Instrum.*, 75:2787–2809, 2004.

[72] D. Nicastro, J.R. Mclntosh, and W. Baumeister. 3d structure of eukaryotic flagella in a quiescent state revealed by cryo-electron tomography. *Proc. Natl. Acad. Sci. USA*, 102:15889–15894, 2005.

[73] M. Okuno and Y. Hiramoto. Direct measurements of the stiffness of echinoderm sperm flagella. *J. Exp. Biol.*, 79:235–243, 1979.

[74] C.M. Omoto and C.J. Brokaw. Structure and behaviour of the sperm terminal filament. *J. Cell Sci.*, 58:385–409, 1982.

[75] O.O'Reilly and P.J. Holmes. Non-linear, non-planar and non-periodic vibrations of a string. *J. Sound Vib.*, 153:413–435, 1992.

[76] D.W. Oplinger. Frequency response of a nonlinear stretched string. *J. Acoust. Soc. Am.*, 32:1529–1538, 1960.

[77] E.M. Purcell. Life at low reynolds number. *Am. J. Phys.*, 45:3–11, 1977.

[78] M. Roper, R. Dreyfus, J. Baudry, M. Fermigier, J. Bibette, and H.A. Stone. On the dynamics of magnetically driven elastic filaments. *J. Fluid Mech.*, 554:167–190, 2006.

[79] E.J. Routh. *The advanced part of a treatise on the dynamics of a system of rigid bodies.* McMillan and Co., 1905.

[80] S.C. Schuster and S. Khan. The bacteria flagellar motor. *Annu. Rev. Biophys. Biomol. Struct.*, 23:509–539, 1994.

[81] L.F. Shampine, I. Gladwell, and S. Thompson. *Solving ODEs with MATLAB, 1st Edition.* Cambridge University Press, 2003.

[82] C. Shingyoji, H. Higuchi, M. Yoshimura, E. Katayama, and T. Yanagida. Dynein arms are oscillating force generators. *Nature*, 393:711–714, 1998.

[83] I.E. Sobel. On calibrating computer controlled cameras for perceiving 3D scenes. *Artif. Intell.*, 5:185–198, 1974.

[84] D. Tam and A.E. Hosoi. Optimal stroke patterns for purcell's three-link swimmer. *Phys. Rev. Lett.*, 98:068105, 2007.

[85] G.I. Taylor. Analysis of the swimming of microscopic organisms. *Proc. R. Soc. London A*, 209:447–461, 1951.

[86] M.S. Triantafyllou and C.T. Howell. Non-linear unstable response of hanging chains. *J. Sound Vib.*, 162:263–280, 1993.

[87] R.Y. Tsai. An efficient and accurate camera calibration technique for 3d machine vision. *P. IEEE Int. Conf. Comput. Vision Pattern Recogn.*, pages 364–374, 1986.

[88] N.B. Tufillaro. Nonlinear and chaotic string vibrations. *Am. J. Phys.*, 57:408–414, 1989.

[89] P. Venier, A.C. Maggs, M.F. Carlier, and D. Pantaloni. Analysis of microtubule rigidity using hydrodynamic flow and thermal fluctuations. *J. Biol. Chem.*, 269:13353–13360, 1994.

[90] A.B. Western. Demonstration for observing $j_0(x)$ on a resonant rotating vertical chain. *Am. J. Phys.*, 48:54–56, 1980.

[91] C.H. Wiggins and R.E. Goldstein. Flexible and propulsive dynamics of elastica at low reynolds number. *Phys. Rev. Lett.*, 80:3879–3882, 1998.

[92] C.H. Wiggins, D. Riveline, A. Ott, and R.E. Goldstein. Trapping and wiggling: elastohydrodynamics of driven microfilaments. *Biophys. J.*, 74:1043–1060, 1998.

[93] D.M. Woolley. Studies on the eel sperm flagellum. 2. kinematics of normal motility. *Cell Motil. Cytoskel.*, 39:233–245, 1998.

[94] D.M. Woolley. Motility of spermatozoa at surfaces. *Reproduction*, 126:259–270, 2003.

[95] D.M. Woolley and G.G. Vernon. A study of helical and planar waves on sea urchin sperm flagella, with a theory of how they are generated. *J. Exp. Biol.*, 204:1333–1345, 2001.

[96] F. Zhu and C.D. Rahn. Stability analysis of a circularly towed cable-body system. *J. Sound Vib.*, 217:435–452, 1998.

[97] J. Zlatanova and S.H. Leuba. Magnetic tweezers: a sensitive tool to study dna and chromatin at the single-molecule level. *Biochem. Cell Biol.*, 81:151–159, 2003.

Vita

Bisen Lin was born in Fujian, China on November 11, 1976, the son of Zancheng Lin and Shixia Zheng. After his graduation from Huian No. 1 High School, he entered Beijing Technology and Business University in September 1995, where he received the Bachelor degree of Science in Engineering with 1st class honor in July 1999. He was admitted to the Graduate School of Tsinghua University in August 1999 and received the Master degree of Science in Engineering in June 2002. In August 2002, he was admitted to the Department of Aerospace Engineering and Engineering Mechanics of the University of Texas at Austin to pursue the Ph.D. degree. He has co-authored the following papers.

[1]. B. Lin and K. Ravi-Chandar, Propulsion of eukaryotic spermatozoa, In preparation, 2007.

[2]. B. Lin and K. Ravi-Chandar, Effect of tension on biofilament dynamics, *Phys. Rev. Lett.*, in review, 2007.

[3]. B. Lin and K. Ravi-Chandar, Steady-state whirling motion of thin filaments, *Int. J. Solids Struct.*, **44**, 3035-3048 (2007).

[4]. B. Lin and K. Ravi-Chandar, An experimental investigation of the motion of flexible strings: Whirling, *J. Appl. Mech.-T ASME*, **73**, 842-851 (2006).

Permanent address: 1642 West 6th Street Apt. D
Austin, Texas 78703

This dissertation was typeset with LaTeX[†] by the author.

[†] LaTeX is a document preparation system developed by Leslie Lamport as a special version of Donald Knuth's TeX Program.